

**Study on Buckling-Restrained Knee Brace Damper  
with Round Steel Core Bar**

(丸鋼芯材を用いた座屈拘束方杖ダンパーに関する研究)

学位取得年月 2022 年 9 月

Togtokhbuyan Munkhunur



## Acknowledgments

### ACKNOWLEDGMENTS

First and foremost, I am extremely grateful to my supervisor, Professor Hiroshi Tagawa, for his invaluable guidance, kindness, and patience during my Ph.D. study. His work ethic, humility, and wisdom inspired and motivated me during critical times when I needed encouragement. From weakness to strength, grass to grace, and nothing to something, the knowledge he has imparted to me will be a great asset throughout my future career. He taught me the value of tolerance, patience, and trust in my future academic life. Thanks once again for all his encouragement and unconditional support. I would also like to thank the assistant professor, Dr. Xingchen Chen, for her technical support in my study. Her humility, diligence, knowledge, and mentorship made it very encouraging during my Ph.D. I would like to express my deepest gratitude to Dr. Tsoggerel Tsamba, the coordinator of the MJEED project, for allowing me to study under her project. Very special thanks to my dear friend Mr. Mateus Segura Jhon Alexander, who helped me greatly from the beginning to the end of my Ph.D. I could not have reached this stage without his support.

My deepest appreciation goes to the Japanese and Mongolian governments for giving me an opportunity to study in such a beautiful, peaceful, and charming country and to get higher education to be more confident with the career path I am taking.

I would like to express my gratitude to my colleagues in the Department of Civil Engineering and Architecture of the Mongolian University of Science and Technology. They have proudly supported me to the extent that it has exceeded all reasonable expectations.

I sincerely thank Professors, Naohiro Nakamura, Hiroyuki Miura, and Dr. Xingchen Chen who reviewed and revised my dissertation to make it more readable and reasonable.

I would like to thank my lab mates for the cherished time spent together in the lab, and in social settings, especially Mr. Feng Shuai, Mr. Zhang Sijin, and Mr. Koga Shotai for their treasured support, which was really influential in shaping my experimental results during my Ph.D. I would like to say to them, "The winds of fortune are blowing in your favor" I have no doubt you will succeed in your achievement soon.

My deepest appreciation also goes to my family, who gave me the time to concentrate on my studies. Special thanks to my wife for carrying the children and for her positivism, patience, and support during my critical time to accomplish my dissertation. My beautiful self-carrying daughters, Sunderiya and Binderiya, are truly amazing, and their independence gives me the strength to go forward and achieve my study goal.

## ABSTRACT

This thesis aims to investigate an innovative application of simple Buckling-Restrained Knee Braces (BRKBs) to distribute plasticity at the beam ends of rigid moment connections and to reveal the applicability of a novel slender cover tubed BRKB for welded and weld-free steel framing systems. A slender knee brace configuration is proposed, consisting of a steel core bar and tubular buckling restrainer. The advantages of tube buckling restrainers include relatively easy implementation for simpler construction and lighter weight compared to mortar-filled buckling restrainers. Two phases of the testing program were performed to achieve the goals of this study. The first phase of the testing program was conducted between February 5<sup>th</sup>, 2020, and March 2<sup>nd</sup>, 2020, while the second phase was conducted between January 27<sup>th</sup>, 2021, and February 2<sup>nd</sup>, 2021, at the Building Structure Laboratory of Hiroshima University. In each chapter of this dissertation, the work done during the research period is summarized as follows.

Chapter 1 starts with a background of the strengthening methods of the steel beam-to-column connections used in steel construction and gives brief explanations of the yield mechanisms of the beam-to-column connections when a knee brace is implemented on them. In addition, the problem statement, the research objectives, and the scope of the dissertation are presented in this section.

In Chapter 2, a literature review of the historical development of the research process on the knee brace systems is given.

In Chapter 3, the procedure of the displacement-controlled cyclic loading tests is presented on examination of the spreading of the plasticity behaviors of rigid moment connections using the proposed BRKBs. Structural performance metrics, such as hysteretic behavior, strength capacity under a given loading, and strain distributions at beam flanges, were measured.

In Chapter 4, an extensive numerical study reveals the optimal parameters for the proposed BRKBs. The results show that the optimal parameters of the proposed slender BRKBs significantly improve load-bearing capacity and reduce stress concentrations in the vicinity of the rigid beam-to-column connections.

In Chapter 5, the results of the test programs such as displacement-controlled compression and cyclic loading tests in investigating the deformation capacities of the proposed novel slender BRKBs with cover tubes are presented. Several contraction allowances were adopted in the proposed BRKBs. Specifically, by increasing the number of contraction allowances, undesirable failure mechanisms that are global instability and local buckling of the restrainer ends can be suppressed effectively because the more uniform plastic deformation of the core bar can be achieved longitudinally.

## Abstract

Chapter 6 summarizes the conclusions of this study and highlights its future extended studies. The final section contains several appendices containing the comparative numerical studies in which an effect of the typical knee brace on the spreading plasticity at the beam was contrasted with the proposed design plasticity mechanisms. In addition, in the last part of this dissertation, the drawing schemes of the test setups with geometric explanations are attached more clearly.

**TABLE OF CONTENTS**

<b>ACKNOWLEDGMENTS</b> .....	<b>I</b>
<b>ABSTRACT</b> .....	<b>II</b>
<b>LIST OF TABLES</b> .....	<b>VI</b>
<b>LIST OF FIGURES</b> .....	<b>VII</b>
<b>NOMENCLATURE AND ABBREVIATIONS</b> .....	<b>IX</b>
<b>1. INTRODUCTION</b> .....	<b>1</b>
<b>1.1 Background</b> .....	<b>1</b>
<b>1.2 Problem Statement</b> .....	<b>3</b>
<b>1.3 Research objectives</b> .....	<b>4</b>
<b>1.4 Scope</b> .....	<b>4</b>
<b>1.5 Dissertation outline</b> .....	<b>6</b>
<b>2. LITERATURE REVIEW</b> .....	<b>8</b>
<b>3. EXPERIMENTAL STUDY FOR THE ASSESSMENT OF SPREADING PLASTICITY IN RMC</b> .....	<b>11</b>
<b>3.1 General</b> .....	<b>11</b>
<b>3.2 Design and theory of the proposed BRKB</b> .....	<b>11</b>
3.2.1 Determination of the position and strength of the proposed BRKB .....	11
3.2.2 Details of the proposed BRKB.....	13
3.2.3 Design theory of the buckling restrainer .....	14
<b>3.3 Cyclic loading tests</b> .....	<b>15</b>
3.3.1 Test specimens.....	15
3.3.2 Testing setup.....	18
3.3.3 Testing data measurement .....	18
3.3.4 Loading conditions and global relative rotation (drift) angles.....	19
<b>3.4 Test results</b> .....	<b>20</b>
3.4.1 Load and global relative rotation angle relationship.....	20
3.4.2 Full plasticity initiation .....	23
3.4.3 Variation in strain distributions .....	26
3.4.4 Residual deformation in the final stage of loading .....	27

## Table of Contents

<b>4. NUMERICAL STUDY FOR THE ASSESSMENT OF SPREADING PLASTICITY IN RMC</b>	<b>39</b>
4.1 Scope of the finite element analysis.....	39
4.2 Element selection .....	39
4.3 Key parameters of FEA models .....	40
4.4 Steel materials.....	43
4.5 Contact modeling.....	43
4.6 Loading and boundary conditions .....	43
4.7 Analysis results .....	43
4.7.1 Effects of the M16 steel bar on overall strength .....	43
4.7.2 Effects of the M22 steel bar on overall strength .....	45
4.7.3 Stress distributions along the beams .....	47
4.7.4 Results for the base beam models .....	49
4.7.5 Results for the M16 steel core bar BRKB beam models .....	49
4.7.6 Results for the M22 steel core bar BRKB beam models .....	49
4.7.7 Detailed assessment of the spreading of plasticity in FEA .....	49
<b>5. EXPERIMENTAL STUDY FOR THE SLENDER BRKB</b>	<b>53</b>
5.1 General .....	53
5.2 Outline of the proposed BRKB dampers .....	53
5.3 Details of the proposed BRKBs.....	54
5.4 Design method for the proposed damper .....	57
5.5 Compression tests .....	59
5.5.1 Test specimens.....	59
5.5.2 Core bar and contraction allowances .....	61
5.5.3 Buckling restrainer and cover tube .....	62
5.5.4 Testing setup and data measurement.....	62
5.6 Compression loading test results.....	65
5.6.1 Load-displacement relationship .....	65
5.6.2 Variation in the strains for the cover tube and buckling restrainer.....	67
5.6.3 Residual deformation after compression loading.....	70
5.7 Cyclic loading tests .....	72

## Table of Contents

5.7.1 Test specimen .....	72
5.7.2 Testing setup.....	75
5.7.3 Data measurement of testing.....	76
5.7.4 Global rotation angles and loading conditions.....	79
<b>5.8 Cyclic loading test results .....</b>	<b>79</b>
5.8.1 Load and global rotation angle relationship.....	79
5.8.2 Strains for the cover tube and buckling restrainer.....	82
5.8.3 Residual deformation after cyclic loading .....	83
<b>6. CONCLUSIONS AND FUTURE RESEARCH NEED .....</b>	<b>89</b>
<b>6.1 Experimental and numerical study for assessment of spreading plasticity in RMC .....</b>	<b>89</b>
6.1.1 Conclusions .....	89
6.1.2 Future research need .....	89
<b>6.2 Experimental study for the novel slender BRKBs.....</b>	<b>90</b>
6.2.1 Conclusions .....	90
6.2.2 Future research need .....	91
<b>References .....</b>	<b>92</b>
<b>Appendix A.....</b>	<b>97</b>
<b>Appendix B.....</b>	<b>102</b>
<b>Related publications.....</b>	<b>109</b>



**LIST OF TABLES**

<b>Table 1</b> – Material properties of specimens .....	17
<b>Table 2</b> – BRKBs used for FEA.....	42
<b>Table 3</b> – Assessment of the spreading of plasticity for FEA.....	51
<b>Table 4</b> – Geometrical parameters of the test specimens used in the compression loading tests ...	59
<b>Table 5</b> – Material properties of the compression loading test specimens .....	61
<b>Table 6</b> – Section modulus of the tubes used in the compression tests .....	62
<b>Table 7</b> – Geometrical parameters of the proposed dampers used in the cyclic loading tests.....	74
<b>Table 8</b> – Material properties of the cyclic loading test specimens .....	74
<b>Table 9</b> – Section modulus of the tubes used in the cyclic loading tests .....	75
<b>Table A1</b> – Assessment of the spreading of plasticity for the TKB beams.....	99

**LIST OF FIGURES**

**Fig. 1.1.** The configuration of strengthened beam-to-column connections (AISC)..... 1

**Fig. 1.2.** KBs as an alternative to conventional rigid and pin connections. ....2

**Fig. 1.3.** Expected plasticity behaviors in various types of beam-to-column connections: .....3

**Fig. 1.4.** Flowchart of chapter dissertation structure.....6

**Fig. 2.1.** Application of the KBs in a single storey frame. ....8

**Fig. 3.1.** Scheme of the theoretical design method. .... 12

**Fig. 3.2.** Proposed BRKB..... 13

**Fig. 3.3.** Theoretical dimensions of the proposed BRKB damper..... 15

**Fig. 3.4.** Schemes for three specimens and their geometric measurements (units: mm). .... 16

**Fig. 3.5.** Detailed geometries of BRKB dampers..... 17

**Fig. 3.6.** General apparatus for testing specimens. .... 18

**Fig. 3.7.** Test setup and measurement plans. .... 21

**Fig. 3.8.** Global relative rotation of the test assembly..... 22

**Fig. 3.9.** Cyclic loading protocol..... 22

**Fig. 3.10.** Relationship between load and global relative rotation. .... 24

**Fig. 3.11.** Strain distributions of the specimen T-N..... 28

**Fig. 3.12.** Strain distributions of the specimen T-S. .... 30

**Fig. 3.13.** Strain distributions of the specimen T-L..... 32

**Fig. 3.14.** Comparisons of strain distributions along the beam between ..... 34

**Fig. 3.15.** Residual deformation of beams in the final stage of loading for three specimens. .... 35

**Fig. 3.16.** Residual deformation of BRKBs in the final stage of loading for two specimens. .... 38

**Fig. 4.1.** FE model of the proposed BRKB and beam..... 40

**Fig. 4.2.** Geometry of the BRKB dampers for the FE models: ..... 41

**Fig. 4.3.** Relationship between load and global rotation of beams ..... 44

**Fig. 4.4.** Relationship between load and global rotation of beams ..... 46

**Fig. 4.5.** Equivalent Von Mises stress distributions in the final stage of loading ..... 47

**Fig. 4.6.** Equivalent Von Mises stress distributions in the final stage of loading ..... 48

**Fig. 4.7.** Equivalent Von Mises stress distributions in the final stage of loading ..... 50

**Fig. 5.1.** Structural configuration of the proposed system: ..... 54

**Fig. 5.2.** Configuration of the proposed buckling-restrained knee brace (BRKB) damper ..... 55

**Fig. 5.3.** Details and exploded view of the proposed damper. .... 55

**Fig. 5.4.** Process followed to build the proposed damper. .... 56

## List of Figures

<b>Fig. 5.5.</b> Geometrical parameters of the proposed BRKB dampers:.....	57
<b>Fig. 5.6.</b> Basic dimensions of the specimens for the compression loading tests.....	60
<b>Fig. 5.7.</b> Test setup and measuring system for the compression loading tests. ....	63
<b>Fig. 5.8.</b> Strain gauge locations. ....	64
<b>Fig. 5.9.</b> Load–displacement relationship. ....	66
<b>Fig. 5.10.</b> Brace axial load and strain relations. (a) for L-BR and (b) and (c) for S-BR.....	67
<b>Fig. 5.11.</b> Brace axial load and strain relations for SCT48-D.....	68
<b>Fig. 5.12.</b> Brace axial load and strain relations for LCT48-2D.....	68
<b>Fig. 5.13.</b> Brace axial load and strain relations for SCT54-D.....	68
<b>Fig. 5.14.</b> Brace axial load and strain relations for LCT54-2D.....	69
<b>Fig. 5.15.</b> Brace axial load and strain relations for SCT57-D.....	69
<b>Fig. 5.16.</b> Brace axial load and strain relations for LCT57-2D.....	69
<b>Fig. 5.17.</b> Residual deformation in the final stage of loading for the reference specimens. ....	70
<b>Fig. 5.18.</b> Residual deformation in the final stage of loading for the SCT specimens.....	71
<b>Fig. 5.19.</b> Residual deformation in the final stage of loading for the LCT specimens. ....	72
<b>Fig. 5.20.</b> Basic dimensions of the dampers for the cyclic loading test specimens. ....	73
<b>Fig. 5.21.</b> General apparatus for the cyclic loading test. ....	76
<b>Fig. 5.22.</b> Photographs of the cyclic loading test setup.....	77
<b>Fig. 5.23.</b> Cyclic loading tests program. ....	77
<b>Fig. 5.24.</b> Vertical load and story drift angle relations for three specimens.....	80
<b>Fig. 5.25.</b> Brace axial load and strain relations for specimen SCT60-D.....	84
<b>Fig. 5.26.</b> Brace axial load and strain relations for specimen LCT60-2D. ....	84
<b>Fig. 5.27.</b> Brace axial load and strain relations for specimen LCT60-3D. ....	85
<b>Fig. 5.28.</b> Residual deformation in the final stage of cyclic loading for the BRKBs. ....	86
<b>Fig. A1.</b> Plastic strain energies for the BRKB and TKB.....	97
<b>Fig. A2.</b> Equivalent Von-Mises stress distributions.....	98
<b>Fig. A3.</b> Relationship between an axial load and axial deformation of the TKBs.....	100
<b>Fig. A4.</b> Relationship between load and global relative rotation for the TKB beam models.....	100

**NOMENCLATURE**

$A_b$	: cross-sectional area of the steel core bar
$c_s$	: clearance between the screw part of the core bar and buckling restrainer
$c_{sh}$	: clearance between the shank part of the steel core bar and buckling restrainer tube
$D$	: inner diameter of the buckling restrainer tube
$d_s$	: core bar screw diameter
$d_{sh}$	: core bar shank diameter
$d_t$	: averaged displacement values measured by d3 and d5
$d_b$	: averaged displacement values measured by d4 and d6
$d_{ct}$	: inner diameter of the cover tube
$D$	: outer diameter of the buckling restrainer tube
$D_{ct}$	: outer diameter of the cover tube
$E$	: Young's modulus of steel
$E_b$	: Young's modulus of steel core bar
$h_f$	: vertical distance between $d_t$ and $d_b$
$I$	: beam moment of inertia
$I_B$	: buckling restrainer moment of inertia
$L$	: total length of the beam
$l_b$	: effective buckling length of the core bar
$l_c$	: total length of the core bar
$M_y^B$	: restrainer tube flexural strength
$M_y$	: beam flexural strength
$M_B$	: bending moment of the beam at point B
$M_C$	: bending moment of the beam at point C
$N$	: brace axial force
$N_E^B$	: buckling strength of the restrainer tube
$N_y$	: core bar / brace yield strength
<b>SF</b>	: restrainer tube safety factor
$T$	: restrainer tube thickness
$P_y$	: concentrated load at the beam tip regarding yield strength
$P_{y1}$	: predicted load relative to the beam-end plasticity for specimen T-N
$P_{y2}$	: predicted load relative to the beam-end plasticity for specimen T-S
$P_{y3}$	: predicted load relative to the beam-end plasticity for specimen T-L
$R$	: global relative rotation angle

## Nomenclature and Abbreviations

$R_{total}$	: total global rotation angle
$R_j$	: beam end plate rotation angle
$R_{ct}$	: the ratio of the section modulus corresponding to the buckling restrainer and cover tube
$w_i$	: distance between points B and C
$Z_{ct}$	: elastic section modulus of the cover tube
$Z_{br}$	: elastic section modulus of the buckling restrainer
$\alpha$	: BRKB inclination angle
$\delta_b$	: elongation of the core bar
$\sigma_y$	: yield stress of the steel material
$\Delta_{BP_y}$	: deflection of the beam at point B due to force $P_y$
$\Delta_{BN_y}$	: deflection of the beam at point B due to axial force $N_y$

## ABBREVIATIONS

<b>AISC</b>	: American institute of steel construction
<b>BRKB</b>	: Buckling-restrained knee brace
<b>FEA</b>	: Finite element analysis
<b>KB</b>	: Knee brace
<b>RMC</b>	: Rigid moment connection
<b>TKB</b>	: Typical knee brace

## 1. INTRODUCTION

### 1.1 Background

The rigid moment beam-to-column connections (RMCs) play an essential role in the performance of the steel framing structures for gravity and lateral loadings. Since they transfer a bending moment to a column, the resulting concentrated forces of the beam flange at the column face can cause unexpected damage or brittle fracture in the vicinity of the connection, particularly if the connection design does not meet seismic design requirements. After unforeseen damage and modes of brittle failure were observed on the RMCs of framed structures during the Northridge (1994) and Hyogoken-nanbu (1995) earthquakes, various studies concluded that the welded areas for the RMCs were very vulnerable to seismic motion [1]–[6]. Expected plasticity tended to occur at beam ends without any yielding in the rest of the structure. Thus, the American Institute of Steel Construction (AISC) has adopted many improvements and strengthening strategies for welded RMCs based on making the connection stronger than the beam [7], [8]. Cover plates, haunches, and upstanding ribs were commonly welded to the beam flanges. Alternatively, beam flanges were widened to increase the strength of connection capacity, and beam flanges were reduced away from welds to decrease demand at the connections, as shown in **Fig. 1.1(a)-(e)**. In those design approaches, the plasticity occurrence is imposed in the beam away from the welded region at the column face.

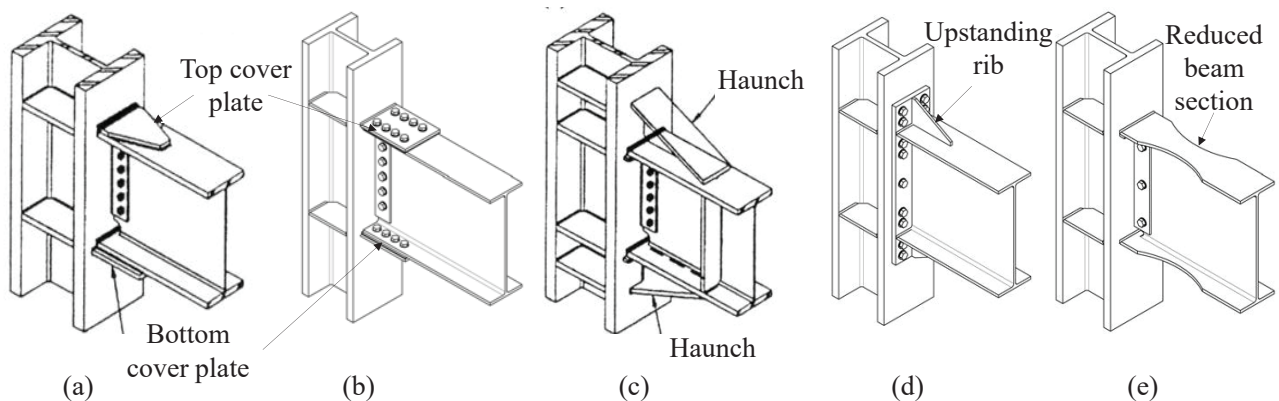


**Fig. 1.1.** The configuration of strengthened beam-to-column connections (AISC).

Following the Kobe earthquake (January 17, 1995), RMCs have been improved in various aspects to prevent brittle fractures around connection areas in Japan. To ensure adequate plastic deformation capacity of RMCs, improved scallop-type welding joints have been proposed and widely used for low-to-middle-rise steel building moment frames [9], [10]. Although these modified connections have demonstrated satisfactory performance in the laboratory, the quality of welds is difficult to control in practice. Therefore, researchers have proposed knee bracing (KB)<sup>1</sup> approaches for strengthening the

<sup>1</sup> In most cases, sufficient stiffness KBs are used to intend relocating the plastic hinges away from the column face.

connection to mitigate the stress concentration at the weld area. The advantages of the KB are replacement and repair costs can be less since the damage is concentrated in those elements. "This configuration provides more flexibility in architectural design than laterally braced frames and reduces construction difficulties of typical rigid connections such as implementing special welding and inspection of the quality on the welding" [11]. As shown in **Fig. 1.2(a)**, the KBs are generally used for the RMCs to relocate stress concentrations away from the welds and for the weld-free connections (pin-connections) as the main energy dissipater to resist the lateral load. The meaning of weld-free implies an idea in which bolts are utilized in beam-to-column connections to minimize the number of welds. When sufficient ductility KBs are adopted in the RMCs, the occurrence of plasticity initiates the outer portion of the KBs at the beam end, as shown in **Fig. 1.2(b)**. In this case, the force induced by lateral load is transmitted by KB through column flange mainly, while the beam-to-column connection absorbs a certain amount of energy simultaneously.

In contrast, when the KBs are adopted in pin-connections, as shown in **Fig. 1.2(c)**, the plasticity occurs at the KBs (KBs are buckled) without yielding the main elements such as beam and column, as shown in **Fig. 1.2(d)**. For instance, the KB absorbing whole energy may lead to early instability of the structural system due to brace buckling or connection damages. More and more sufficient ductility typical KBs than those used in RMCs are probably needed for pin-connection systems to ensure the stability of structural systems. To avoid such ineffective design, applications of BRKBs for weld-free connection systems have been widely accepted in Japan.

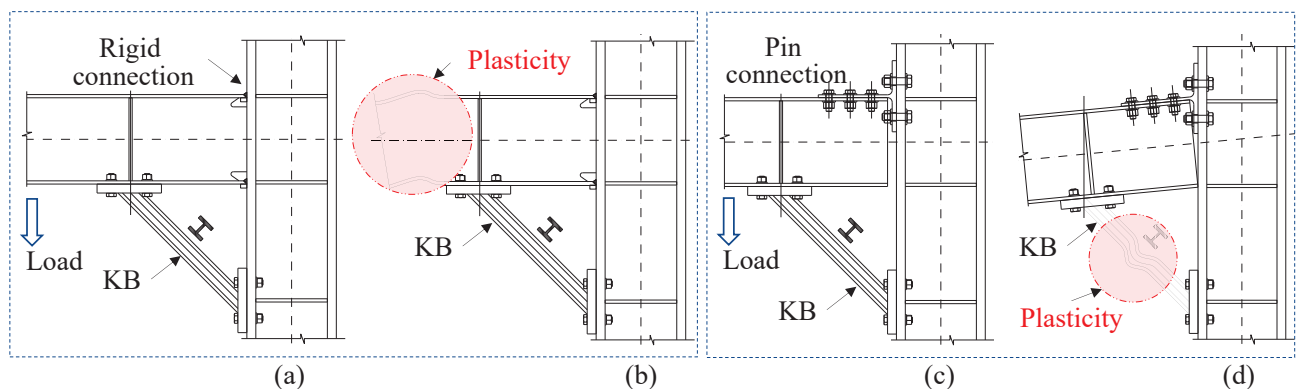


**Fig. 1.2.** KBs as an alternative to conventional rigid and pin connections.

- (a) RMCs with the KB, (b) Plasticity occurrence at the outer portion of the KB at the beam end,  
 (c) Weld-free connection with KB, and (d) Buckling of the KBs.

Since typical KBs exhibit buckling during the seismic motion, various configurations of non-buckling KBs named buckling-restrained KBs (BRKBs)<sup>2</sup> have been widely proposed in steel

<sup>2</sup> BRKBs consist of buckling restrainers and core elements.

structural systems. The amount of energy absorption in the BRKBs system is more than the typical KBs system. In addition, the cyclic behavior of the BRKBs is probably more stable than the typical KBs. Generally, to ensure the required ductility for the seismic design of a structural system, the possible yield mechanism should be determined in advance. If the beams and columns are intended to be in an elastic range, the yield mechanism should initiate by yielding of the knee element. In this structural system, mostly weld-free connections, in some cases known as simple shear or pin connections, are utilized with the BRKBs. These braces absorb the seismic energy as a replaceable ductile fuse.

In contrast, the influences of the slender BRKBs on the RMC systems have not been completely elucidated by the researchers. Their structural yield mechanism that affects the plasticity of beams is still little-known. Therefore, in order to fill this research gap, the study, which will be discussed in the following sections, is carried out in this research.

## 1.2 Problem Statement

In the RMCs, expected plasticity tends to occur at beam ends without any yielding in the rest of the structure, as shown in **Fig. 1.3(a)**. Additional strengthening methods need to be implemented to make a connection stronger unless the seismic performances of ordinary RMCs should meet the seismic design requirements. In this regard, the application of KBs is the most common strategy for rehabilitating existing structures and constructing new structures. When using typical KBs for RMCs, plasticity occurs outside the KBs at the beam end depending on the brace strength, as shown in **Fig. 1.3(b)**.

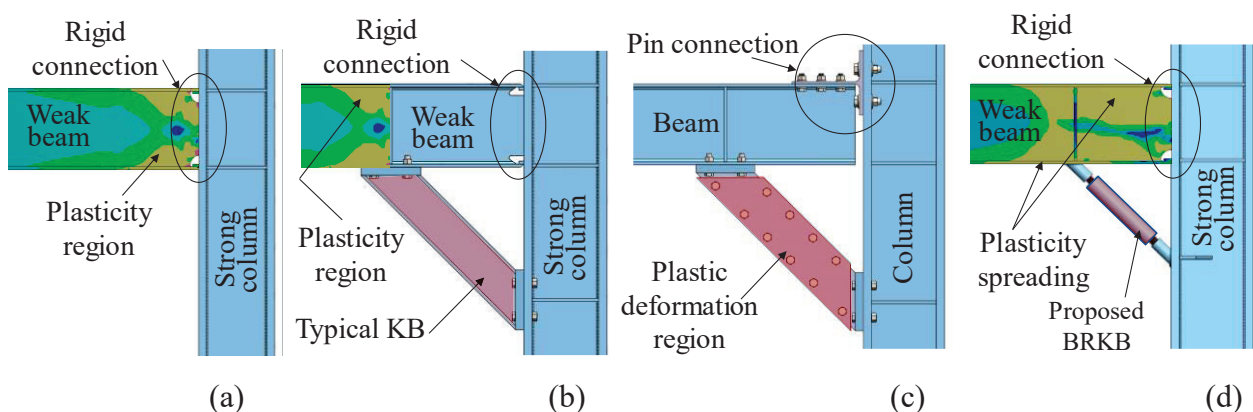


**Fig. 1.3.** Expected plasticity behaviors in various types of beam-to-column connections:

- (a) typical RMC, (b) RMC with a typical KB, (c) pinned connection with a BRKB,  
and (d) RMC with the proposed BRKB.

For the weld-free connections, mainly the BRKBs are used to remain the beams and columns in the elastic range. In this system, the energy induced by the seismic load is only dissipated by the



BRKBs, as shown in **Fig. 1.3(c)**. **Fig. 1.3(d)** shows the spreading plasticity around the beam end due to the proposed BRKBs with a proper configuration used for the RMCs. The study on this assumption has not been fully investigated for the seismic design procedure of the RMCs structural system so far. Therefore, this study proposes one of the possible BRKBs for design purposes, known as a steel core bar BRKB damper, and presented the study's progress in the first half of this dissertation. As a result of the first half of this study, this study also proposes a novel slender cover-tubed BRKB damper with steel core bars in the second half of this dissertation. In this novel slender BRKB damper, the cover tube increased the number of contraction allowances. Specifically, by increasing the number of contraction allowances, undesirable failure mechanisms that are global instability and local buckling of the restrainer ends can be suppressed effectively because the more uniform plastic deformation of the core bar can be achieved longitudinally. In addition, to overcome the struggle in weld quality assurance for the RMCs, the second proposal of this dissertation, which is the novel slender BRKB damper with the cover tube, can be utilized for weld-free connections. In these regards, the consistency of the proposed novel slender BRKB damper for both RMCs and weld-free connections should be assessed by experimental investigations within this study.

### 1.3 Research objectives

In general, this research consists of two objectives. The first objective was to investigate an innovative application of BRKBs for spreading plasticity at the beam ends of RMCs. The second objective was to investigate a novel slender BRKB damper for the spreading plasticity around the beam end in RMCs and the steel framing systems in weld-free connections.

### 1.4 Scope

The scope of this dissertation comprises two phases of the research program. Each phase has two substages. In the first phase, the steel bar core BRKB damper was proposed for the RMCs to decrease the stress concentration at the weld region during the seismic loads, as shown in **Fig. 1.3(d)**. In this regard, one experimental program with an extended numerical analysis was conducted to investigate the behavior of the spreading plasticity in the RMCs based on the applicable design criteria of the proposed BRKB dampers. The extended numerical analysis verified the results of the experimental program and assessed the additional design criteria of the proposed dampers, which have not been tested in the experimental program.

In the second phase, a novel slender cover-tubed buckling-restrained BRKB damper was developed for both RMC and weld-free beam-to-column connections. Two substages of experimental programs have been carried out to assess the major cyclic behavior of the proposed BRKBs affecting the performance of weld-free connections. A series of experimental studies on relatively long and slender

## Chapter 1 Introduction

BRKBs with round steel core bars were conducted using monotonic and cyclic loading tests for the first substage and second substage, respectively, in this phase.

### 1.5 Dissertation outline

As shown in **Fig. 1.4**, the study follows two main key phases: assessment of spreading plasticity in improved-scallop RMC using the proposed damper; assessment of the cyclic performance of the proposed slender damper with the cover tube. Based on the key phases, this dissertation has been structured in the following chapters:

Chapter 1 starts with a background of the strengthening methods of the steel beam-to-column connections used in steel construction and gives brief explanations of the yield mechanisms of the beam-to-column connections when a knee brace is implemented on them. In addition, the problem statement, the research objectives, and the scope of the dissertation are presented in this section.

Chapter 2 presents preliminary studies beginning with a literature review of the historical development of the research process on the knee brace systems and summarizing further research on the energy dissipation capacities of the different configurations of knee braces used for beam-to-column connections. This section also discusses the recent studies on applications of a steel bar used as an energy dissipator for beam-to-column connections.

Chapter 3 examines the performance of the spreading plasticity around the beam end using the proposed steel core bar BRKB dampers for the improved-scallop RMCs. In this regard, the beam-to-column connection subassembly specimens with two different lengths of the proposed dampers were tested. Their results are compared with the result of the reference specimen (no-brace beam-to-column connection subassembly). The discussion then considers the relationships between load and global relative rotation, strain distributions of upper and lower flanges of beams, and visual inspection of plasticity behavior of both beams and dampers for each specimen.

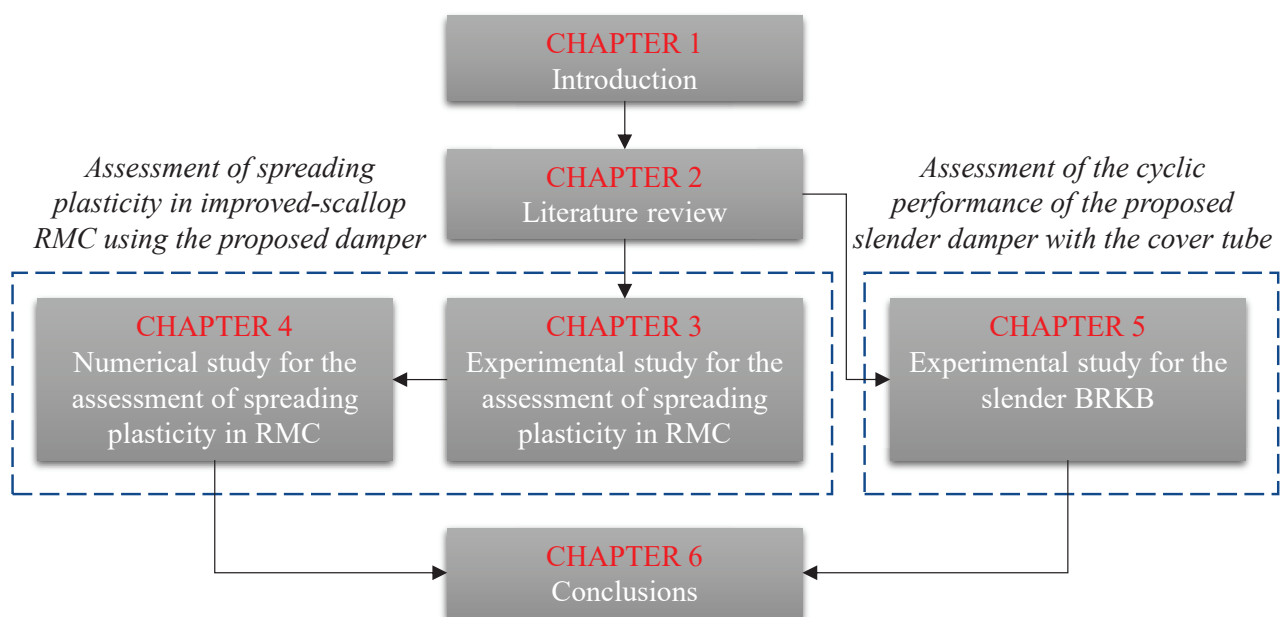


**Fig. 1.4.** Flowchart of chapter dissertation structure

This chapter reveals that the shorter damper has shown a high satisfaction for the spreading plasticity around the beam end in stable conditions (no damage). As against, for the longer brace, a noticeable bending behavior with minor thread failure was observed in the upper exposed section of the core bar after the cyclic loading tests. Based on the discussion on the comparison of the behavior of spreading plasticity for each specimen, the extensive numerical analysis was conducted in the following chapter 4.

Chapter 4 presents the extensive numerical studies using finite element analysis to examine the additional design criteria for the proposed shorter dampers. Specifically, to this end, the one-directional one-way loading analysis provided by ANSYS was employed in this section. The analysis results exhibit good agreement with the laboratory testing results. In addition, the percentage of the difference between the FE analysis and test results in each specimen for the relationship between load and global relative rotation is less than 7% regarding each peak value of the cyclic loadings. Moreover, detailed descriptions of the FEA parameters and results are provided in this chapter.

Chapter 5 examines the energy dissipation capacities of the proposed novel slender cover tube BRKB dampers using weld-free beam-to-column connections. Since chapter 3 revealed that noticeable damage was inspected in the exposed portion of the steel core bar for the longer BRKB damper, the number of contraction allowances were provided by the cover tube in this novel slender BRKB damper. Specifically, by increasing the number of contraction allowances, undesirable failure mechanisms that are global instability and local buckling of the restrainer ends can be suppressed effectively because the more uniform plastic deformation of the core bar can be achieved longitudinally. To examine the energy dissipation capacities of this new damper, two series of test programs, such as compression and cyclic loading tests, were carried out, and their results are discussed and summarized in this chapter. In addition, this new damper can be applied in weld-free beam to column connection to overcome the struggle in weld quality assurance in the RMC.

Chapter 6 summarizes the conclusions of this entire study within two subsections and offers suggestions for further inquiry investigations because future research is highly needed to extend this study. The last section contains several appendices with the comparative numerical studies in which an effect of the typical knee brace on the spreading plasticity at the beam was contrasted with the proposed design plasticity mechanisms. In addition, in the last part of this dissertation, the more precise drawing schemes of the test setups with geometric explanations are attached.

## 2. LITERATURE REVIEW

The KBs were used as the main ductile fuse element for conventional diagonal bracing systems in the early stages of their development [12]–[15][16]. For example, one of the earliest studies of knee bracing systems was proposed by Aristizabal-Ochoa in 1986 [17]. In that research, the conventional bracing technique was composed of two structural elements: knee and diagonal braces, as depicted in **Fig. 2.1**. The bracing technique was known as the Disposable Knee Bracing system (DKB), and in which it was recommended that the size of knee elements should be 50% lighter than the beam or column size. The knee element provides ductility, whereas the diagonal brace remains elastic when the test specimen is subjected to a lateral load. The study concluded that a system comprising a knee brace and diagonal braces was effective in rigid and semi-rigid beam-to-column connections.

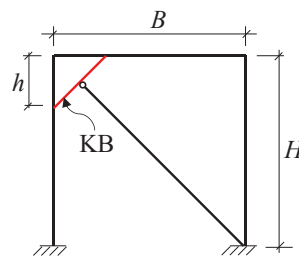


**Fig. 2.1.** Application of the KBs in a single storey frame.

Mofid et al. [18] and Huang et al. [19] conducted additional two studies based on the achievement of the above studies. They investigated a particular form of DKB and proposed a simple technique, using graphs and charts for the design of the DKB. In addition, they revealed that position and stiffness of the knee were the most important factor affecting the lateral resisting ability of the KB frame, followed by a strong influence on its energy dissipating behavior.

Leelataviwat et al. [20] conducted an experimental study on the knee-braced moment frames. They utilized relatively short knee braces without a diagonal brace to relocate plastic hinges away from the column face. In that study, plastic activities of the beam, which form outside of the knee brace portion at the beam end, were confined by the knee brace. They concluded that cyclic tests on relatively large-scale specimens indicated that knee-braced RMCs behave in a ductile manner with stable hysteretic characteristics. Energy was dissipated by KB buckling and beam yielding outside of the KB regions.

Hsu and Li [6] assessed the seismic performance of RMC frame systems with the H-section knee braces. The KBs were placed for the frame systems in two plane directions: in-plane and out-of-plane. The test results showed that the cyclic energy dissipated significantly regardless of whether buckling of the KB occurred in two plane directions. However, they suggested that KBs with an in-plane controlled buckling mechanism can practically be adapted for knee bracing frame systems.

As it can be seen that most of the previous studies on typical knee braced systems intended to design the KBs yielding followed by the occurrence of plastic hinges is formed out of the knee portion at the beam end. Since typical KBs exhibit buckling when the load induced by the seismic activities reaches a certain critical value, other approaches for the KB systems have been introduced to restrict that failure mechanism. In this respect, various configurations with a different ductile manner of buckling-restrained knee braces (BRKBs) that meet the requirements of the high architectural versatility of the structures have been investigated for weld-free connection frames. The approach referred to as the BRKB weld-free system, also called the simple shear beam-to-column connection, is becoming popular in Japan and other countries.

Chusilp et al. [21] first proposed a new structural system known as the weld-free system with a compact BRKB comprising the core plate coated by a friction-reduced material and steel tee section buckling restrainer. It can be mentioned here that the configuration of their proposed BRKB was more compact than devices previously proposed in studies by Watanabe [22], and Iwata et al.[23]. The study revealed that the hysteretic behavior of their proposed weld-free system was shown to be four times greater than expected design consideration against the large ground motions. To construct a bi-directional frame, Kawai et al. [24] suggested a new weld-free system using square tube columns instead of wide-flange columns. Their study tested the full-scale beam-to-column connection with the BRKBs. The suggested connection with the proposed damper could possess stable hysteresis characteristics under large seismic excitation. Thus, the application of a multistory or a single-story structural frame system with BRKBs has been investigated marginally with the time-history and nonlinear static and dynamic analyses [25]–[27]. Meanwhile, researchers have also extensively carried out studies of experimental verification on the performance of the BRKB in different design aspects [28], [29].

Inoue and Suita [30] and Tagawa and Kaneko [31] proposed BRKBs that consist of two main parts, namely buckling-restrainers and core elements, in which the core elements are placed between two buckling-restraining plates. These studies adopted the pin beam-to-column joint to examine the damper deformation. Consequently, research has revealed that BRKBs with the proper configuration have shown good hysteretic behavior under cyclic loads up to controlled story drifts. In these systems, the beams were fully elastic under the forces caused by the knee braces.

Although diverse forms of steel core elements have been used in various BRKBs, studies on steel core bars for BRKBs are still in their infancy. Steel core bar BRKB dampers are essential advanced energy dissipation technology for precast concrete, timber, and steel beam-to-column connections [32]–[36]. Previous studies on post-tensioned structures have proven that steel core bar BRKB dampers are effective for external fuse-type dissipaters for beam-to-column connections. For example,

a recent study by Tagawa et al. [37] investigated the application of buckling-restrained round steel bar dampers to bolted steel beam-to-column connections. Dampers were attached between the bottom flange of the beam and column flange to dissipate energy as same as that damper used in timber structures. A curious consideration on that study was that the authors revealed that the screwing process through the bar ends plays an essential role in the performance of the core bar dampers. The study also concluded that the geometrical characteristics of the shank parts should be carefully taken in the application of the proposed dampers. The cases of using steel round bars for the bracing systems are addressed in the next paragraphs in more detail.

Fujii and Tagawa [38] proposed a buckling-restrained brace (BRB) using steel core bars restrained by double-round steel tubes separated by spacers. Their study revealed that the proposed BRBs with steel core bars provided sufficient capacity under cyclic loading by controlling contraction allowances. Takamatsu and Tamai [39] experimented with a non-compression knee brace in which steel bars were used as the main braces for T-shaped RMCs. In their study, the steel bars exhibited excellent behavior under cyclic loading. Such RMCs are applicable to the rehabilitation of moment-resisting framed structures, although steel core bar compressive states were not considered in their study.

Mateus et al. [40] have proposed a buckling-restrained brace composed of round steel bar cores restrained by inner round steel tubes and an outer square tube. Their experimental results revealed three important design factors: the applicability, restraining capacity, and end-coupler performance of the proposed braces. One crucial statement on their conclusions related to our study was that "when the number of contraction allowance zones is increased, the efficacy and performance of the brace becomes more satisfactory."

Reviewing the literature may lead back to the following summaries: The less stability or excessive strength and stiffness of the typical knee braces (TKBs) cause stress concentration in the beam end or induce plastic strain energy concentration outside of the knee brace portion at the beam, respectively. Instead of expecting the occurrence of the failure mechanism in desired positions as stated above, spreading the plasticity around the beam end can be one of the critical aspects of the research on strengthening steel beam-to-column connections. As seen from previous studies, a lack of studies on the spreading plasticity around the beam end has been investigated. Hence, the spreading plasticity around the beam end for the RMCs will be assessed by experimental and numerical investigations applying a steel bar core BRKBs damper. Overall, two types of slender BRKBs will be considered in this research. One of them is proposed for RMCs to spread plasticity, while another novel slender BRKB is proposed for both RMCs and weld-free beam-to-column connections to retrofit existing or new structures. Finally, the proposed damper's performances will also be examined in various design criteria using a series of experiments and numerical studies.

### 3. EXPERIMENTAL STUDY FOR THE ASSESSMENT OF SPREADING PLASTICITY IN RMC

#### 3.1 General

This chapter first describes the design and theory of the proposed BRKB. Next, cyclic loading experimental studies with steel core bar BRKBs are presented to demonstrate the ability to disperse stress concentrations from beam-to-column connection areas. Additionally, an extended numerical analysis of one-way loading (brace compression side) is presented. Based on the results of our analysis, several applicable BRKB design criteria for the spread of plasticity in connection areas are established.

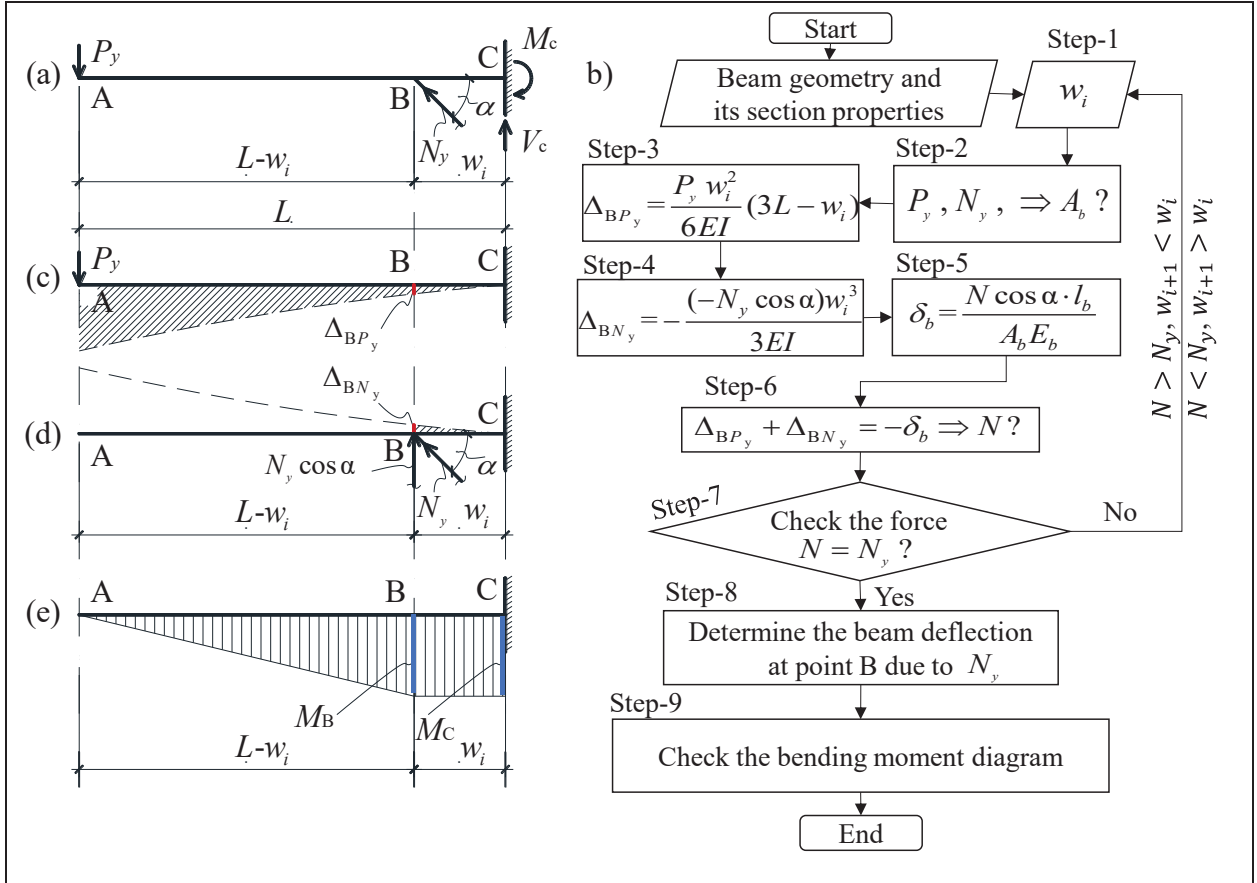
To mitigate the stress concentration at the weld area using the improved scallop-type moment beam-to-column connections, this study proposes an innovative application of steel core bar BRKBs to spread plasticity around beam ends. The typical knee braces (TKBs) cannot achieve a similar effect for the spreading of plasticity compared to our proposed BRKB damper. TKBs' less stability or excessive strength and stiffness cause stress concentration in the beam end or induce plastic strain energy concentration outside of the knee brace portion at the beam, respectively (see Appendix A). When slender BRKBs are used for RMCs, KB yielding followed by beam end plasticity is spread both inside and outside the KB areas. In this study, an excessively stiff column was intentionally used because the behavior of the column was discarded entirely.

#### 3.2 Design and theory of the proposed BRKB

##### 3.2.1 Determination of the position and strength of the proposed BRKB

This study proposed that a cross-section of the steel core bar in the BRKB and the distance  $w_i$  at which the BRKB is connected to the beam at point B, as depicted in **Fig. 3.1(a)**, can be determined using a simplified theoretical design method in the elastic range, as illustrated in **Fig. 3.1(b)**. The cantilever beam is subjected to a concentrated load  $P_y$  at its free end, as depicted in **Fig. 3.1(a)**. First, the downward deflection of the beam at point B due to the concentrated load  $P_y$  is determined, as shown in **Fig. 3.1(c)**. Second, the upward deflection of the beam at point B due to the reaction force,  $N_y$ , produced in the steel core bar is determined, as shown in **Fig. 3.1(d)**. The reaction force,  $N$ , produced in the steel core bar is obtained using the compatibility equation of the total deflection of the beam at point B and the elongation of the steel core bar. Finally, the appropriate distance  $w_i$ , corresponding to the selected steel core bar, is obtained when the bending moment between points B and C is equalized ( $M_B = M_C$ ), as shown in **Fig. 3.1(e)**, after several iterations of the above-mentioned procedure.





**Flowchart description:**

Step-1. Selection of an arbitrary distance  $w_i$ .

Step-2. Calculation of the cross-sectional area of the steel core bar  $A_b$ ,

$$\text{Set } M_B = M_C = M_y, P_y = N_y \cos \alpha$$

$$P_y = \frac{M_y}{L-w_i}, N_y = \frac{P_y}{\cos \alpha} \Rightarrow A_b = \frac{N_y}{\sigma_y} = \frac{M_y}{(L-w_i) \sigma_y \cos \alpha}$$

Step-3. Determination of the downward deflection of the beam at point B due to the concentrated load  $P_y$ .

Step-4. Determination of the upward deflection of the beam at point B due to the reaction force  $N_y \cos \alpha$  in the steel core bar.

Step-5. Determination of the elongation of the steel core bar due to the reaction force  $N$ .

Step-6. Determination of the force  $N$  using the equilibrium compatibility equation at point B.

Step-7. Check whether force  $N = N_y$ ?

Step-8. Determination of the beam deflection at point B.

Step-9. Check the bending moment diagram.

**Fig. 3.1.** Scheme of the theoretical design method. (a) cantilever beam subjected to a concentrated load at beam tip, (b) flowchart of selection of distance  $w_i$ . (c) downward deflection of the beam at point B due to  $P_y$ , (d) upward deflection of the beam at point B due to force  $N_y \cos \alpha$  in the steel core bar. (e) bending moment diagram.

### 3.2.2 Details of the proposed BRKB

**Fig. 3.2** presents the components and assembled views of the proposed BRKB. The primary loading-resistant member, namely the steel core bar, is placed inside a round steel tube (buckling-restrainer), as shown in **Fig. 3.2(a)**. The left and right screw connectors connect it to the column and beam flanges, respectively, where the right screw connector is welded to the beam at a steel fabrication plant in advance. For ease of construction, the left screw connector is prepared separately by the fabricator and erected with the other members at the construction site. The two opposing screws provide adjustment capabilities during assembly. To avoid collisions between the tube restrainer and surrounding connectors caused by global relative rotation angles, beam deflection, etc., two contraction allowances are provided in the proposed BRKB based on previous experimental experience [38], [40]–[43]. A commercial spring is attached to the lower contraction allowance zone to hold the tube restrainer during cyclic loading testing, as shown in **Fig. 3.2**. According to the FEMA-350 standard, for RMC frames, a service median strength degradation global relative rotation angle capacity of 0.02 rad and ultimate capacity of 0.03 rad are required [44]. The expected elongations of the steel core bars were calculated for the BRKB specimens based on these criteria. The screw parts of the steel bar are inserted into the connectors and restrainer tube, as shown in **Fig. 3.2(b)**. The theoretical dimensions and design theory of the proposed BRKB are described in the following section.

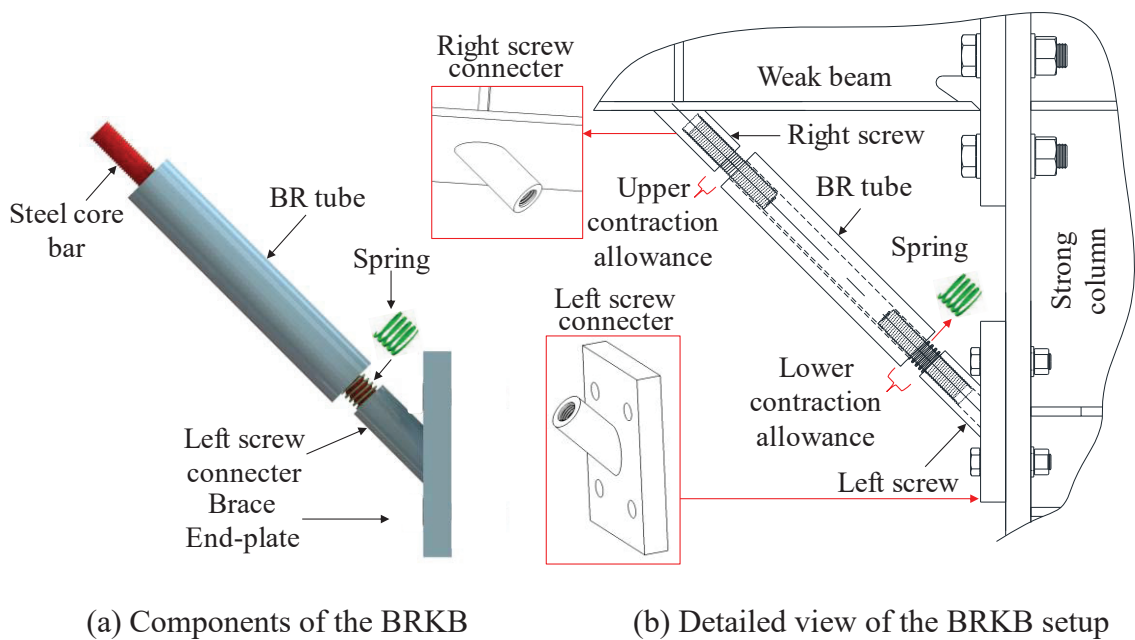


**Fig. 3.2.** Proposed BRKB.

### 3.2.3 Design theory of the buckling restrainer

**Fig. 3.3** presents the theoretical dimensions of the proposed BRKB, where  $D$ ,  $d$ , and  $t$  represent the outer diameter, inner diameter, and thickness of the buckling restrainer, respectively. To prevent instability in the steel core bar, the screw parts are inserted into the restrainer and connector at a distance of  $2d_s$ , where  $d_s$  indicates the diameter of the screw part of the steel core bar. The proposed BRKB member selection process uses theories introduced in previous studies [41]–[43], [45]. The theory and design of the proposed BRKB consider the interactions between restrainers and core elements in terms of their strength and stiffness. The restrainer flexural yield strength should satisfy Eq. (3.1).

$$M_y^B \geq \frac{N_c c_{sh}}{1 - N_c/N_E^B} \quad (3.1)$$

where  $M_y^B$  is the yielding moment capacity of the buckling restrainer,  $N_c (= \xi N_y)$  is the core bar yield strength amplified by the compression-to-tension overstrength and strain hardening, and an amplification factor of  $\xi = 1.5$  is assumed. The parameter  $c_{sh}$  is the clearance between the shank part of the steel core bar and buckling restrainer tube.  $N_E^B$  is the Euler buckling load of the buckling restrainer, which is defined by Eq. (3Error! Reference source not found..2).

$$N_E^B = \frac{\pi^2 EI_B}{l_b^2}$$

(3Error! Reference source not found..2)

where  $EI_B$  is the flexural rigidity of the restrainer, and  $l_b$  is the effective buckling length of the steel core bar (between the edges of the left and right screw connectors). For our design purposes, Eq. (3.1) can be rearranged to incorporate the safety factor, as shown in Eq. (3.3).

$$\text{SF} = \frac{(M_y^B)}{\left( \frac{\xi N_y c_{sh}}{1 - (\xi N_y/N_E^B)} \right)} \geq 1 \quad (3.3)$$

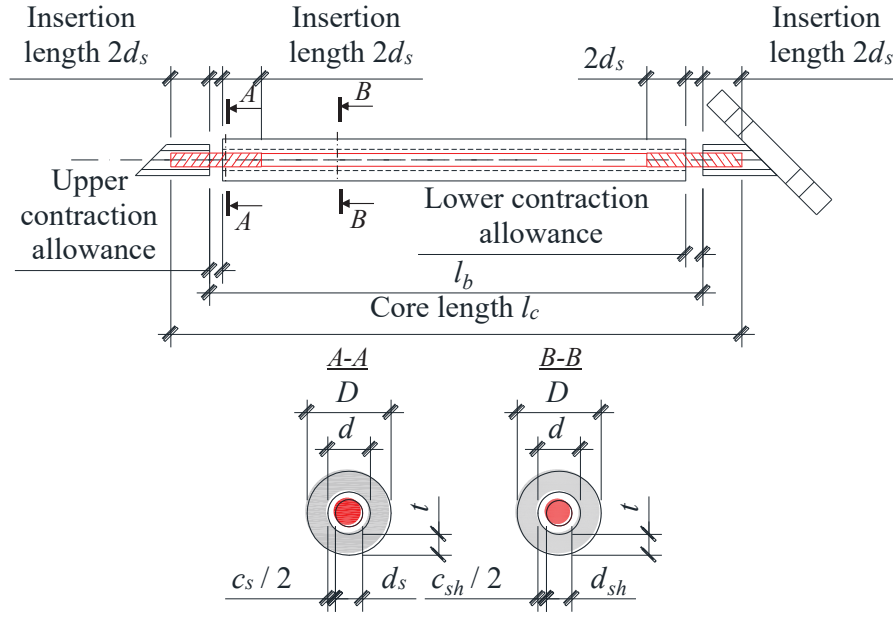


**Fig. 3.3.** Theoretical dimensions of the proposed BRKB damper.

### 3.3 Cyclic loading tests

#### 3.3.1 Test specimens

In this section, three specimens were fabricated and tested to investigate the spreading of the plasticity behavior of beams. These specimens are representative of a no-brace beam (T-N), short-brace beam (T-S), and long-brace beam (T-L). **Fig. 3.4** presents the three specimens and their geometries. **Table 1** lists the material properties of the specimens. A section of H-250 × 125 × 6 × 9 (H-depth × flange width × web thickness × flange thickness) beam with a length of 1.4 m was utilized for each specimen and attached to a section of H-250 × 250 × 19 × 25 column (built-up section), as shown in **Fig. 3.4**. The strong built-up column is completely fixed to the reaction frame. Additionally, BRKBs are attached to either the beam or column at a 45° inclination. The experimental study test parameters were selected based on the brace lengths  $l_b$  and  $l_c$ , as shown in **Fig. 3.4** and **Fig. 3.5**, where  $l_b$  represents the core bar effective buckling length (between the edges of the left and right screw connectors) and  $l_c$  represents the actual length of the core bar.

A clearer description of the BRKBs is presented in **Fig. 3.5**. A round steel tube section with dimensions of 48.6 × 12 mm (diameter  $D$  × thickness  $t$ ) is used for the buckling restrainer in all BRKB specimens. Structural double-threaded anchor bolts with the ABR product specification are used for the core bars. A preliminary simplified finite element analysis (FEA) study was conducted to analyze the spreading of plasticity along RMC beams, where only a steel bar was used as a KB under brace tension state loading [46]. In this analysis, various geometric characteristics, such as longer and

shorter knee braces with M16, M22, and M30 steel bar sections, were considered in our models. This preliminary study revealed that the M22 bar positively affected the spreading of plasticity around connections. Therefore, the M22 steel core bar was selected to test in this section. The core bars have M22 threads at both ends and have a non-threaded section (called the shank) with a diameter of 20.2 mm based on the JIS B 1220 standard. According to the ABR specification, the shank section should deform instead of the threaded sections before yielding.

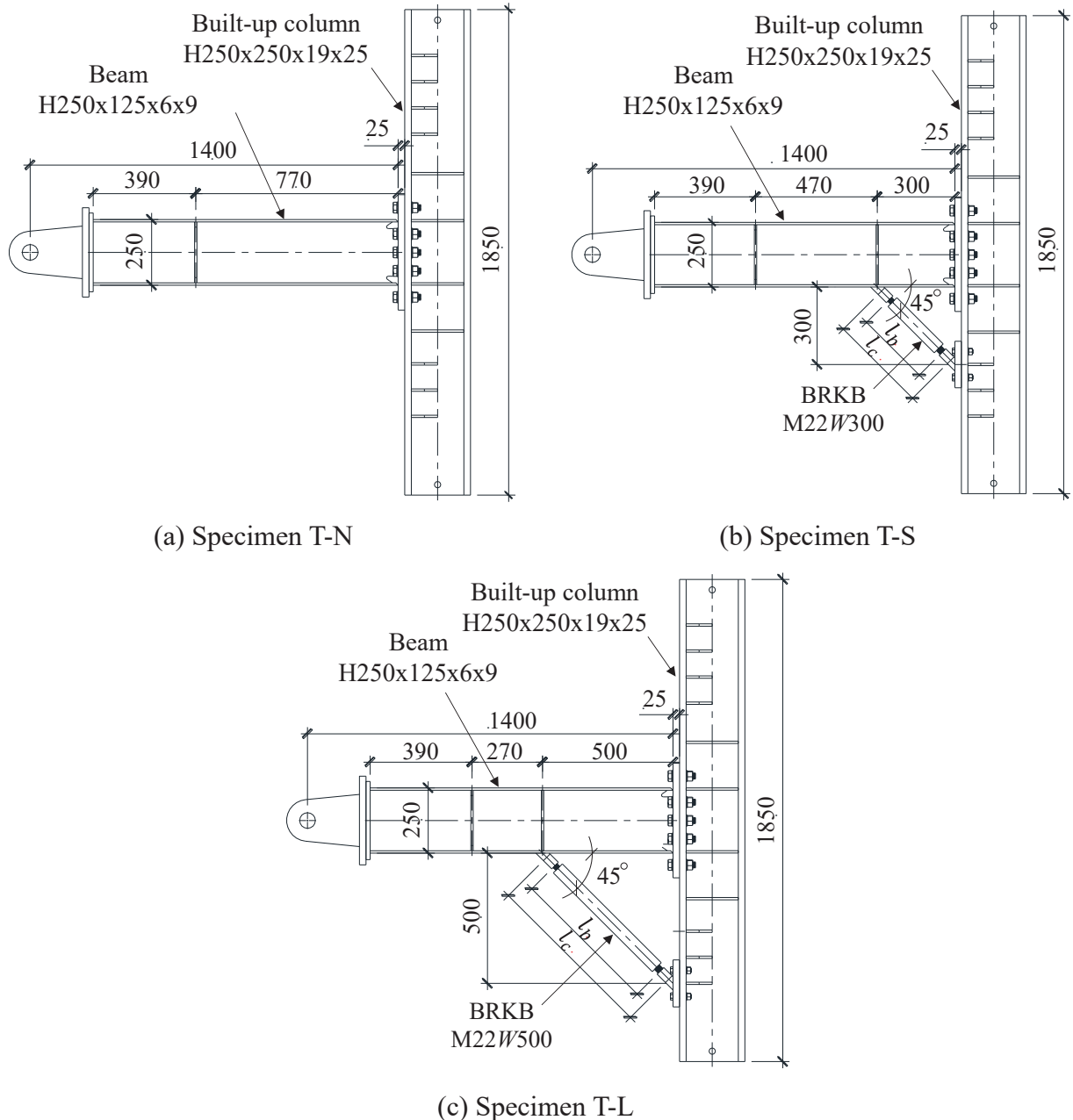


**Fig. 3.4.** Schemes for three specimens and their geometric measurements (units: mm).

Our experimental study adopted a steel core bar with a sufficiently stiff restrainer to prevent unexpected buckling when the brace was subjected to compressive force. However, a relatively thin buckling restrainer will be discussed later in Sections 1 and 4.7. As mentioned previously, the core

bar threaded sections are inserted into the restrainer and screwed into the end connector by a distance of 45 mm.

**Table 1** – Material properties of specimens

Steel grade	Name	Yield stress (N/mm <sup>2</sup> )	Ultimate stress (N/mm <sup>2</sup> )	Elongation (%)
SN400B	Beam	313	458	27
SN400B	Column	303	452	30
ABR400	M22 bar	307	461	32
STKM 13A	Round tube	287	464	58
SN400B	End plate	351	483	28

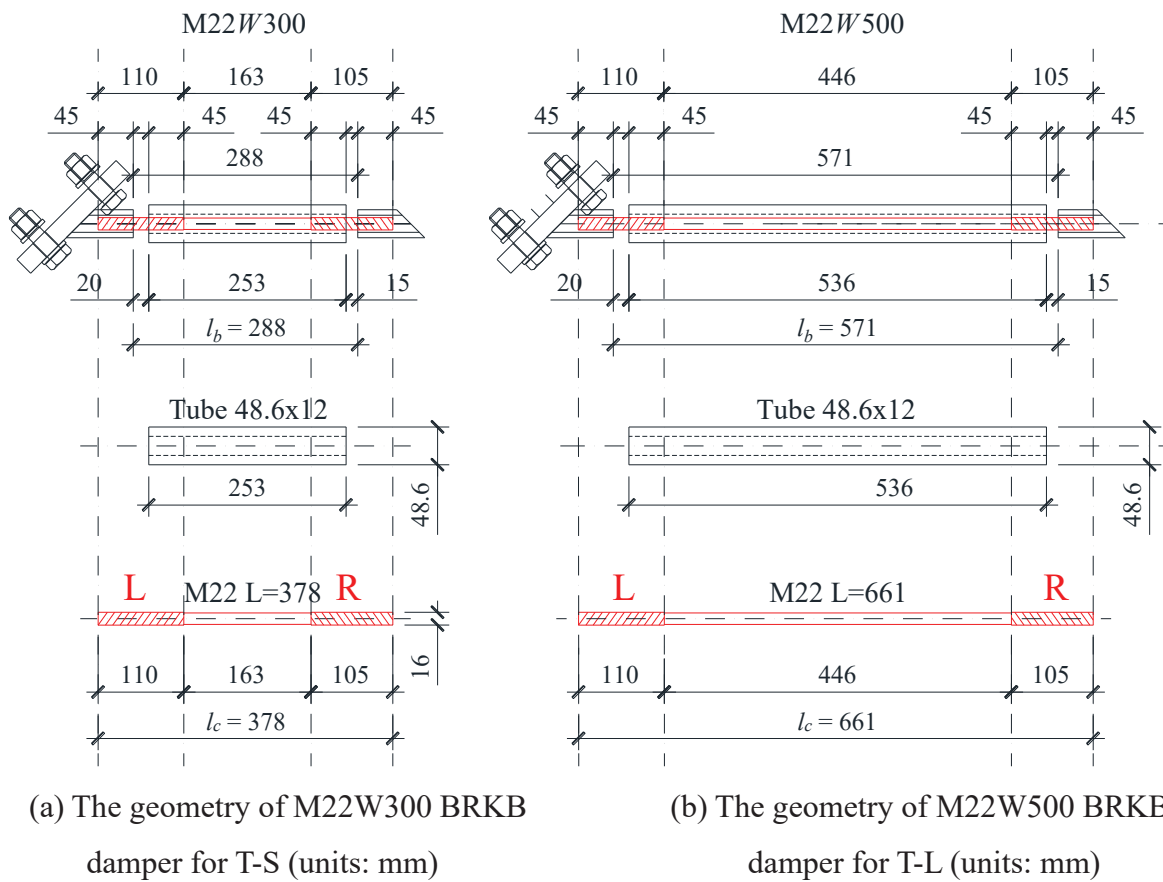


**Fig. 3.5.** Detailed geometries of BRKB dampers.

Therefore, the shank sections will not be exposed when the rotation angle reaches 0.02 rad, which can occur in a large earthquake event. The contraction allowance was determined based on a conventional design check, which was mentioned in Section 3.2.2, and a length of 35 mm was selected to satisfy the requirements.

### 3.3.2 Testing setup

Tests were performed at the building structure laboratory of Hiroshima University. **Fig. 3.6** presents the general apparatus used for testing specimens. A built-up BRKB is assembled on the beam and column, as shown in **Fig. 3.6** (detail A). In general, out-of-plane displacements are entirely constrained by out-of-plane stoppers, as shown in **Fig. 3.6** (B and C). In this experimental study, the column of the specimen attached to the reaction frame is fully fixed. Thus, the beam-sway mechanism can likely be different in our experimental study. However, because the goal of this study is to examine the wider area of plasticity on the beam, a strong column/weak beam philosophy is valid to eliminate plasticity in the column in this entire study proposal.

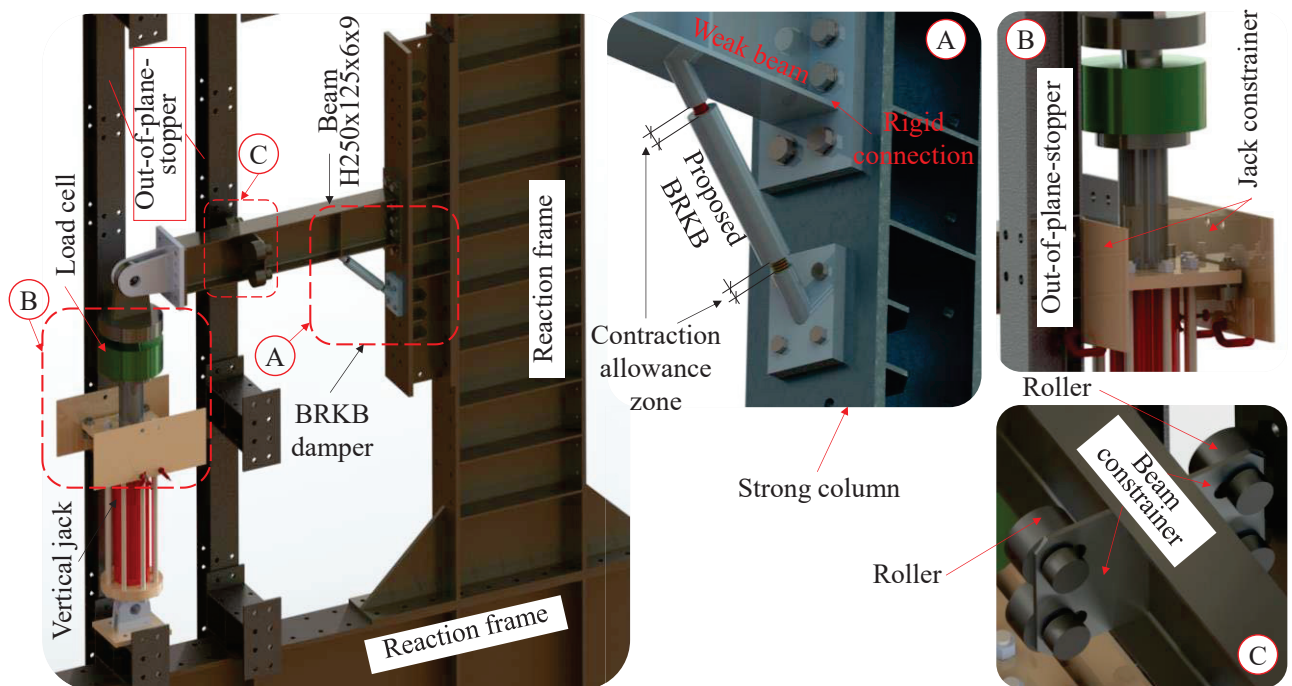


**Fig. 3.6.** General apparatus for testing specimens.

### 3.3.3 Testing data measurement

A vertical load  $P$  was applied using a hydraulic actuator (maximum force of 1000 kN and stroke of 500 mm) at the beam tip. The downward direction is assigned a positive sign, as shown in **Fig. 3.7** and **Fig. 3.8**. The following testing data were measured: (1) vertical load and corresponding vertical displacement of the beam tip, (2) rotation of the beam-end plate, (3) strains of the beam upper and lower flanges, and (4) deformation of the BRKBs for specimens T-S and T-L.

Displacement sensor d1 is used to obtain the vertical displacement of the beam tip. Displacement sensors d3 to d6 are utilized to measure the displacement of the beam end-plate rotation, as shown in

**Fig. 3.7(b)**. Displacement sensors d7 and d8 are attached to the BRKBs to measure the elongation of the steel core bars in the T-S and T-L specimens. Finally, the beam upper and lower flange strains are measured by a series of strain gauges corresponding to each specimen, as shown in **Fig. 3.7(c)** and **Fig. 3.7(d)**.

### 3.3.4 Loading conditions and global relative rotation (drift) angles

As mentioned in the previous section, the rigid columns prevent any influence from column deformation on the test results. Additionally, to exclude influence of the beam end-plate rotation angle  $R_j$ , global relative rotation angle  $R$  as defined in **Fig. 3.8** is used for loading protocol. Note that  $R$  is continuously obtained during the test using measured values of  $R_j$  and the total rotation angle  $R_{total}$ .  $R$ ,  $R_{total}$ , and  $R_j$  are calculated using Eqs. (3.4), (3Error! Reference source not found..5), and (3Error! Reference source not found..6).

$$R = R_{total} - R_j \quad (3.4)$$

$$R_{total} = \frac{d1}{L} \quad (3Error! Reference source not found..5)$$

$$R_j = \frac{d_t - d_b}{h_f} \quad (3Error! Reference source not found..6)$$

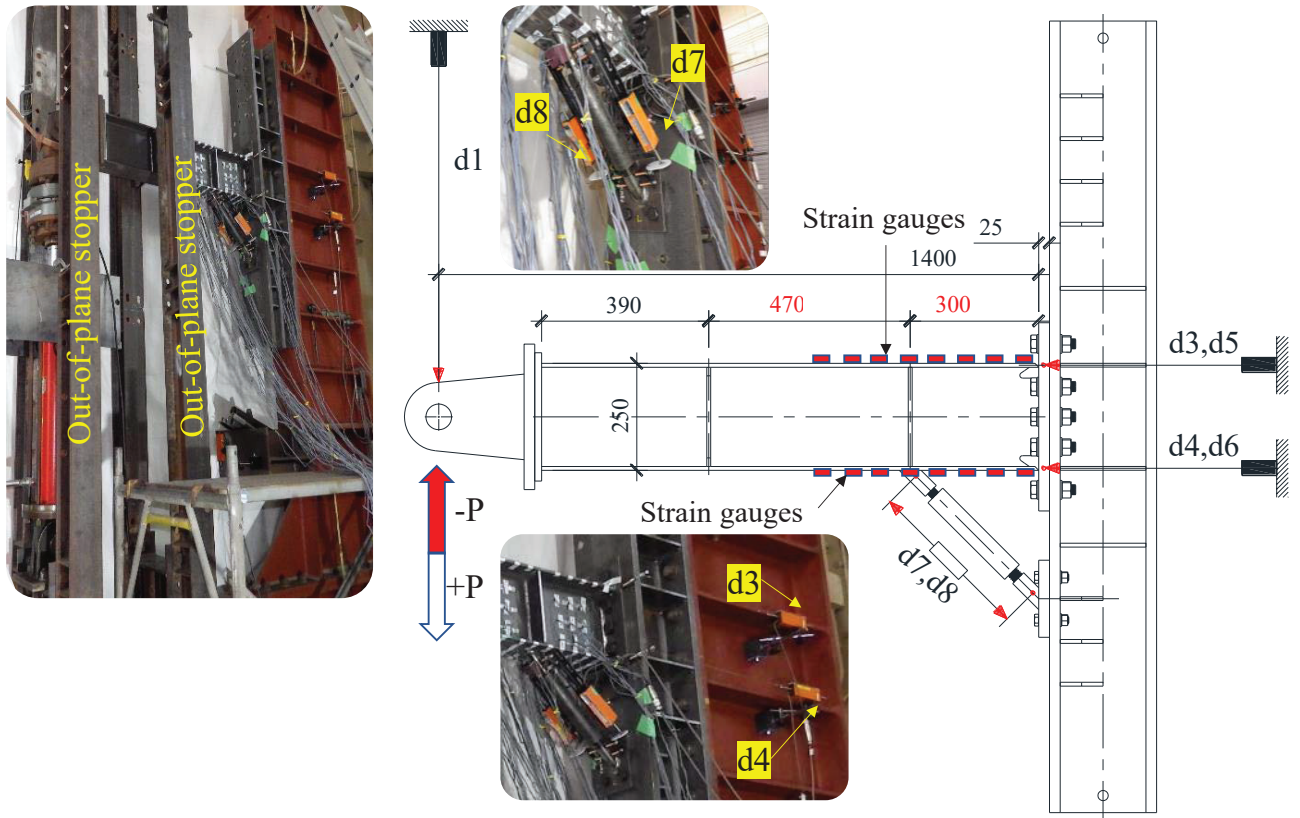
where  $d_t$  and  $d_b$  represent the averaged displacement values measured by d3 and d5 at the beam top flange level, and d4 and d6 at the beam bottom flange level, respectively, and  $h_f$  represents the vertical distance between the  $d_t$  and  $d_b$  displacements. The loading protocol is presented in **Fig. 3.9**. The left vertical axis represents the global relative rotation angle, and the right vertical axis represents the beam tip displacement. Displacement-controlled cyclic loading was applied in the test program, and it increased gradually until the beam exhibited strength deterioration. Two loading cycles were performed for each amplitude level of  $\delta_p$ ,  $2\delta_p$ ,  $3\delta_p$ ..., and  $8\delta_p$ . Despite the effects of the brace on the test specimen, the full plastic moment of the beam tip deflection  $\delta_p$  was determined based on the T-N specimen. This value was determined to be 9 mm in this study.



### 3.4 Test results

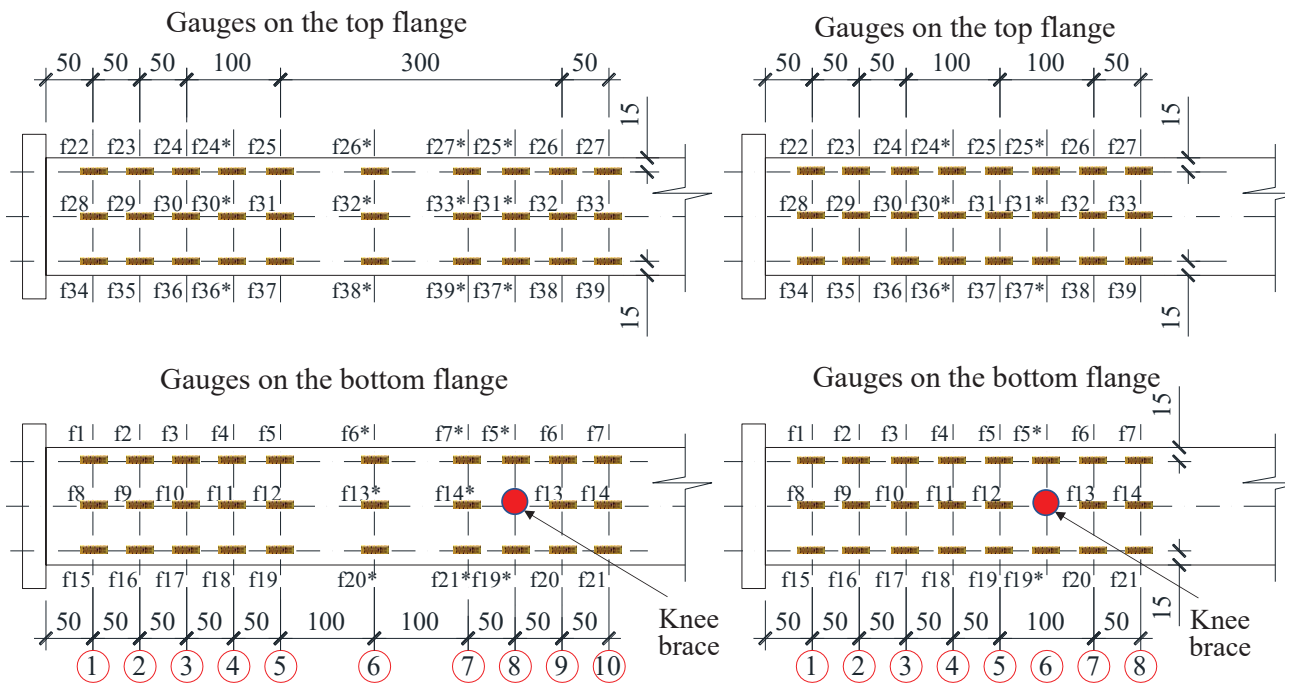
#### 3.4.1 Load and global relative rotation angle relationship

**Fig. 3.10** presents the test results for the cyclic responses of the three specimens, which were subjected to cyclic loading, reaching  $R(\text{rad}) = 5.14\%$ . As shown in **Fig. 3.10**, the hysteretic loops of each loading cycle exhibit suitable shapes for each specimen. The horizontal dashed lines in each graph indicate that the vertical loading reaches the plastic moment limit in the corresponding cross sections of the beams. The notation  $P_{y1}$  indicates the predicted load relative to the beam-end plasticity for specimen T-N. For  $P_{y2}$  and  $P_{y3}$ , the predicted loads are relative to the beam plasticity at the brace top-end connections associated with specimens T-S and T-L, respectively, as shown in **Fig. 3.10(e)**. Any load beyond these points results in fully plastic deformation. **Fig. 3.10(d)** presents comparisons between the peak strength values of each specimen in each cycle. Up to  $R(\text{rad}) = \pm 3.21\%$ , no significant changes in strength were observed between the positive and negative loading sides for the three specimens. In addition, all three specimens met the AISC seismic requirements [47], i.e., the measured flexural resistance at the moment connection should be at least  $0.8M_p$  of the connected beam at a story angle of  $R(\text{rad}) = \pm 4\%$ , where  $M_p$  denotes the nominal plastic moment of the beam. For the T-N specimen, no changes were observed in the peak strength values for both the positive and negative loadings. For the T-L and T-S specimens, the strengths continued to increase beyond  $R(\text{rad}) = +4\%$ . For the T-L specimens, strength degradation was initiated before the story drift reached  $R(\text{rad}) = -4\%$ . In addition, it can be seen from the T-S specimen that the appropriate parameters of the proposed brace can increase the seismic resistance under cyclic loads. The residual deformation behavior up to the final loading stage is discussed in Section 3.4.4.



(a) Photograph of the test setup

(b) Displacement sensor positions (T-S)



(c) Strain gauges (T-N) and (T-L)

(d) Strain gauges (T-S)

**Fig. 3.7.** Test setup and measurement plans.

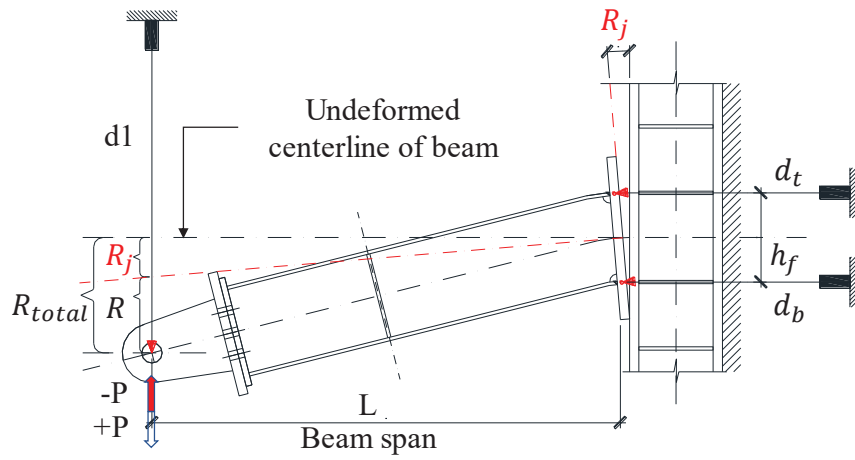


Fig. 3.8. Global relative rotation of the test assembly.

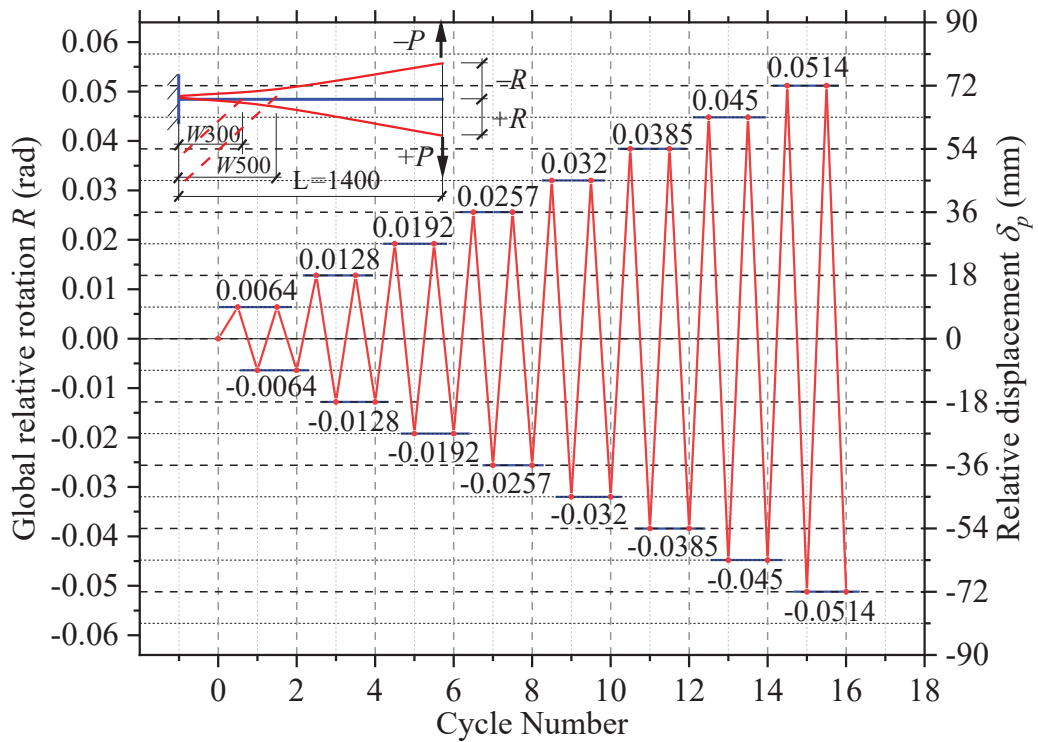
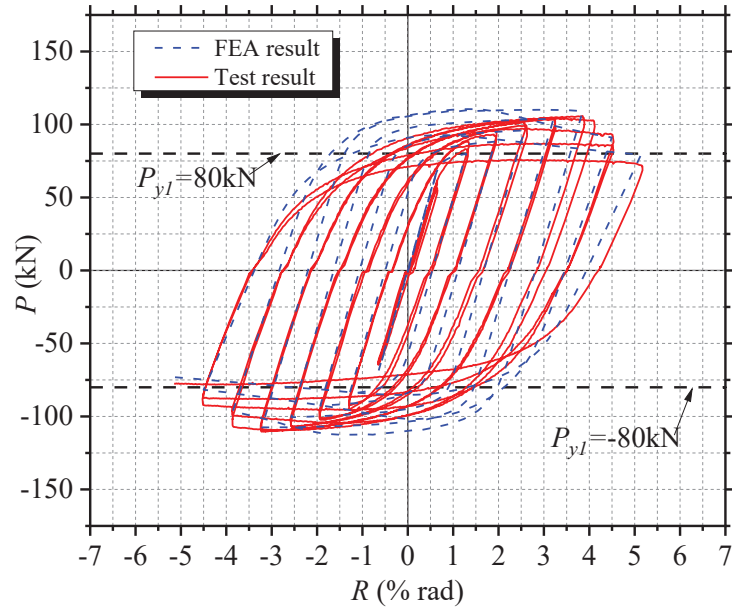


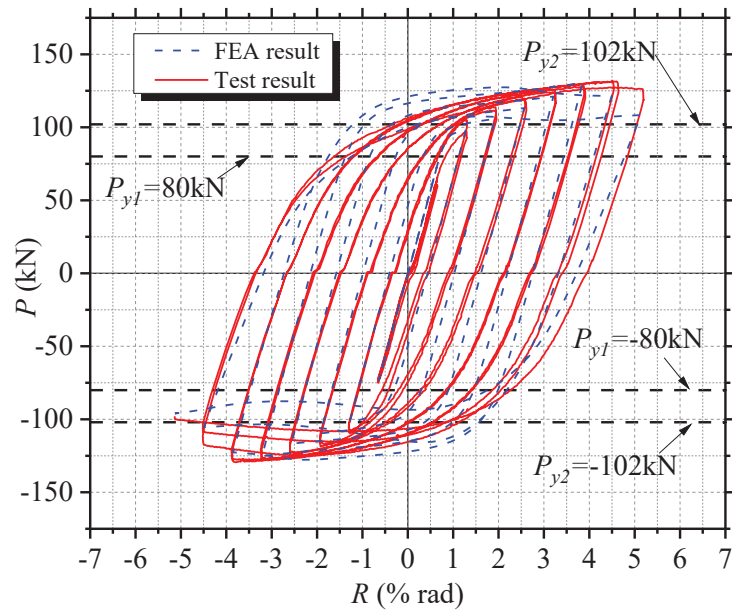
Fig. 3.9. Cyclic loading protocol.

### 3.4.2 Full plasticity initiation

In this section, the full plasticity initiation for each specimen is described using a skeleton curve. **Fig. 3.10(e)** presents comparisons between the skeleton curves of the three specimens. There are six points: A, B, and C (representing the full plasticity predicted loadings  $P_{y1}$ ,  $P_{y2}$ , and  $P_{y3}$  on the negative side), and A\*, B\*, C\*, (representing the full plasticity predicted loadings  $P_{y1}$ ,  $P_{y2}$ , and  $P_{y3}$  on the positive side), which were compared to reveal the loads at the full plasticity initiation points for each specimen. The first full plasticity that occurred close to the beam end for specimen T-N was initiated from  $R(\text{rad}) = +1.13\%$  (Point A\*) and  $R(\text{rad}) = -0.9\%$  (Point A). In the case of specimen T-S, full plasticity was initiated at  $R(\text{rad}) = +1.45\%$  (Point B\*) and  $R(\text{rad}) = -1.23\%$  (Point B). In the case of specimen T-L, full plasticity was initiated at  $R(\text{rad}) = +2.37\%$  (Point C\*) and  $R(\text{rad}) = 2.1\%$  (Point C). Overall, the full plasticity of each specimen initiates slightly earlier on the negative loading side than on the positive loading side. It is noteworthy that the proposed BRKB can enhance a system's strength capacity and delay the full plasticity initiation along the beam adequately. Furthermore, in the following section, the strain distribution behaviors are presented for the test specimens to describe additional details of the plasticity distributions along the beams.

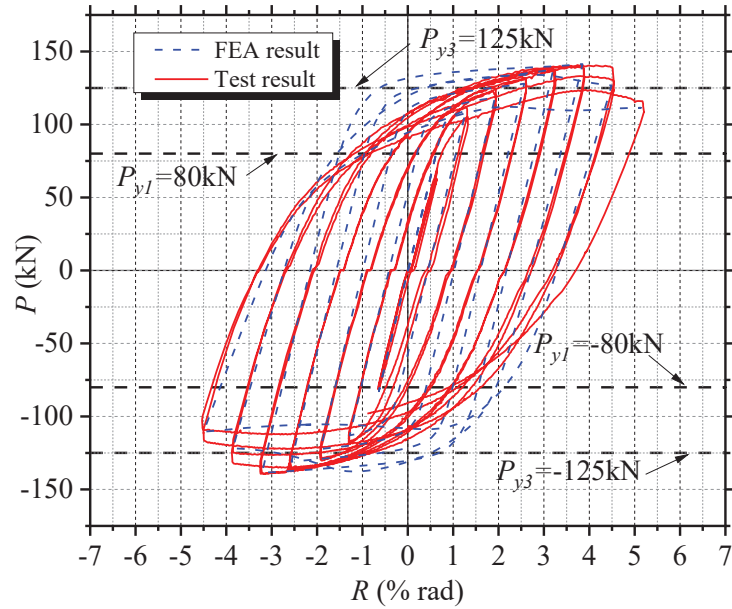


(a) T-N

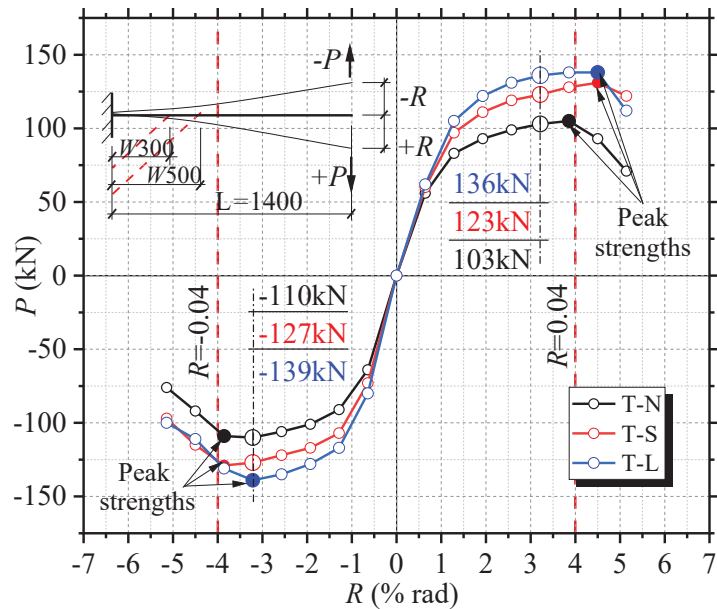


(b) T-S

**Fig. 3.10.** Relationship between load and global relative rotation.

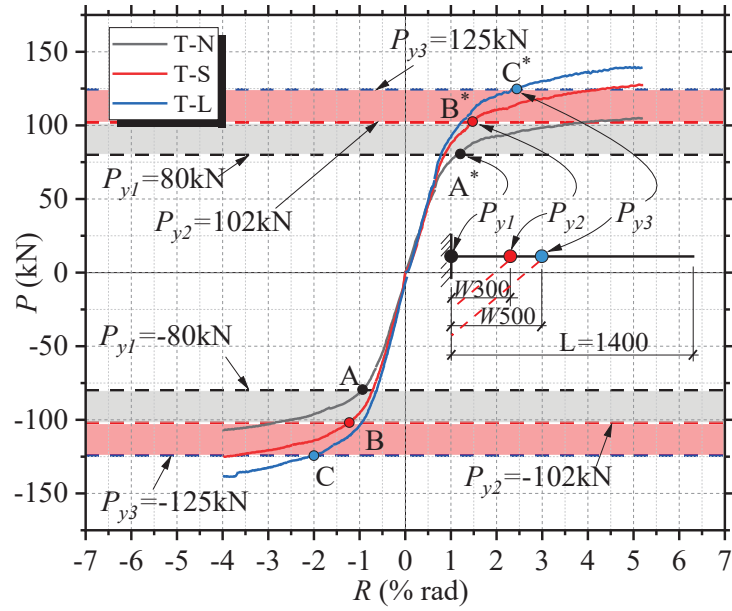


(c) T-L



(d) Peak values of strength per cycle

**Fig. 3.10.** Relationship between load and global relative rotation (continued).



(e) Skeleton curves of three specimens

**Fig. 3.10.** Relationship between load and global relative rotation (continued).

### 3.4.3 Variation in strain distributions

In our experimental study, the strain distributions of the beam upper and lower flanges were monitored at 8 to 10 longitudinal positions, depending on the BRKB length. **Fig. 3.11** to **Fig. 3.13** present the strain distributions (gauge position versus microstrain) of the beam flanges for each specimen under a given external load. The strain in the range of the global relative rotation angle up to  $R(\text{rad}) = \pm 3.85\%$  was considered in this study.

For all specimens, position 1 experiences dominant strains with respect to the observed drift angle in the tensile states of the beam flanges, as shown in **Fig. 3.11(a)** and **Fig. 3.11(d)**. However, the peak values of the compressive strain state for both the upper and lower flanges of the beam for specimen T-N are dominant at position 2, as shown in **Fig. 3.11(b)** and **Fig. 3.11(c)**. These strain distribution behaviors along the beam flanges are particularly evident for the pure cantilever RM connection frame.

Furthermore, in the short BRKB specimen T-S, the strain distributions slightly decrease from positions 1 to 8 in terms of the tensile states of the upper and lower flanges, as shown in **Fig. 3.12(a)** and **Fig. 3.12(d)**. However, for the compressive states of the upper and lower flanges, the dominant strains occur at different positions. For example, as shown in **Fig. 3.12(c)**, there is no significant increase or decrease in the strain distribution along the beam when the global relative rotation angles are  $R(\text{rad}) = -0.64\%$  and  $R(\text{rad}) = -1.28\%$ . Furthermore, when the global relative rotation angle

reaches  $R(\text{rad}) = -3.85\%$ , the dominant strain is observed at position 2. This can be explained as follows. When the

BRKB steel core bar yields, position 2 exhibits less resistance to the large amplitude of cyclic loading. In contrast, for the lower flange compressive state, the strain, which is correlated to all corresponding global relative rotation angles, is distributed continuously along the beams, as shown in **Fig. 3.12(b)**.

Furthermore, in the long BRKB specimen T-L, the strain distributions are dominant in the BRKB inner portion of the beam in each tensile and compressive stress state, as shown in Fig. 14. For example, when the values of the global relative rotation angles are between  $R(\text{rad}) = +0.64\%$  and  $R(\text{rad}) = +3.21\%$ , the strain values spread dominantly along the inner portion of the BRKB on the beam, as shown in **Fig. 3.13(a)** and **Fig. 3.13(b)**. However, slight spreading can be observed in the outer portion of the BRKB for large amplitudes of rotation angles. Therefore, the strain values are dominant in the BRKB inner portion in both the lower and upper beam flange tensile and compressive states, as shown in **Fig. 3.13(c)** and **Fig. 3.13(d)**.

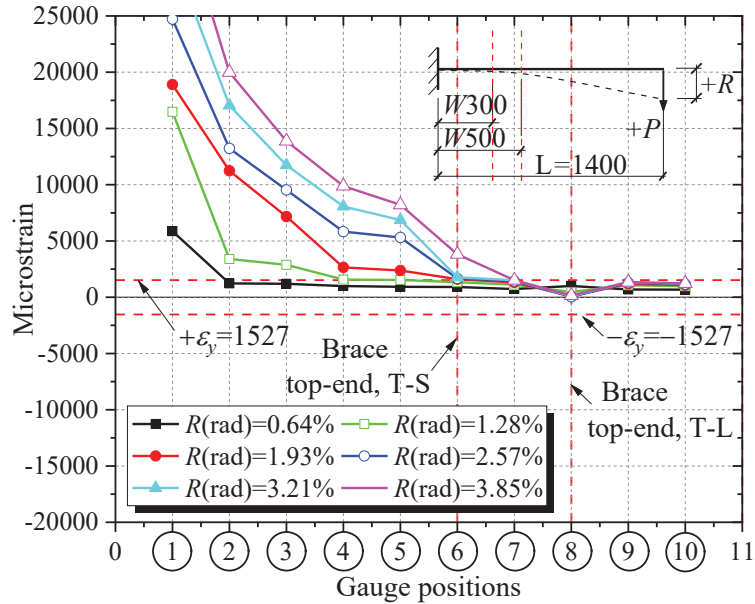
The strain distributions of the three specimens only exhibit differences of  $R(\text{rad}) = \pm 3.21\%$  compared to each other, as shown in **Fig. 3.14**. The strain distribution along the beam tends to stabilize the corresponding beam flanges at the monitored positions of specimen T-S. It can be observed that the brace length significantly affects the strain distribution. The effects of the shorter brace are significant in terms of the spread of plasticity of the BRKB RMC developed in this study. In addition, for both the T-S and T-L specimens, the stress concentrations around gauge position-1 were significantly reduced compared to that in the T-N specimen. For instance, it can be seen from **Fig. 3.14(a)** and **Fig. 3.14(b)** that the strain value at gauge position-1 was higher than  $25000 \mu\text{m/m}$  for the T-N specimen and lower than  $20000 \mu\text{m/m}$  for the T-S and T-L specimens in both the brace compression and tension sides.

#### 3.4.4 Residual deformation in the final stage of loading

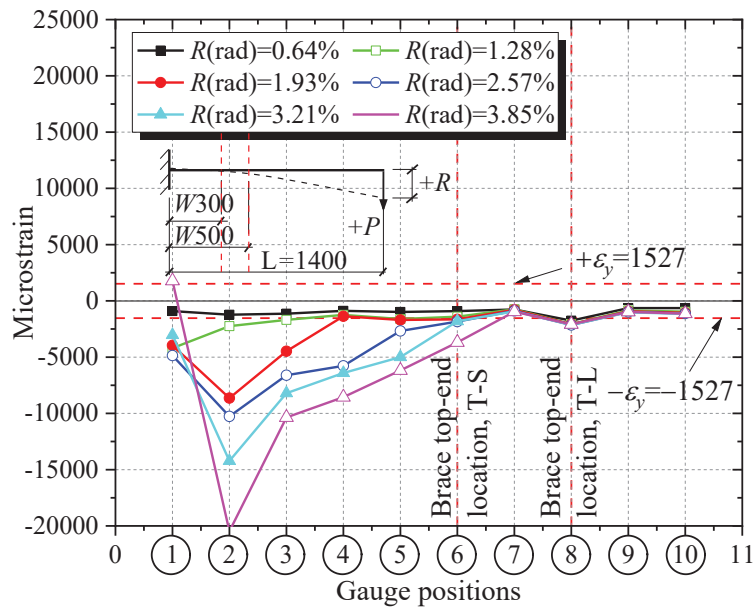
**Fig. 3.15** presents the residual deformation at the beam flanges after the loading tests. Overall, local buckling was initiated beyond  $R(\text{rad}) = \pm 3.85\%$  for all three specimens. The yellow circles in each figure represent the local buckling locations, which can be observed at the flanges around the beam end close to the column face for specimen T-N, as shown in **Fig. 3.15(a)**. The local buckling behaviors of the upper and lower flanges are relatively symmetric and asymmetric relative to the beam's neutral plane and symmetry plane, respectively.



The local buckling in the lower flange is smaller than that in the upper flange of the T-S specimen, as shown in Fig. 3.15(b). For this specimen, on the lower flange backside, new local buckling developed outside of the BRKB area after extensive cyclic loading, as shown in Fig. 3.15(b-2).

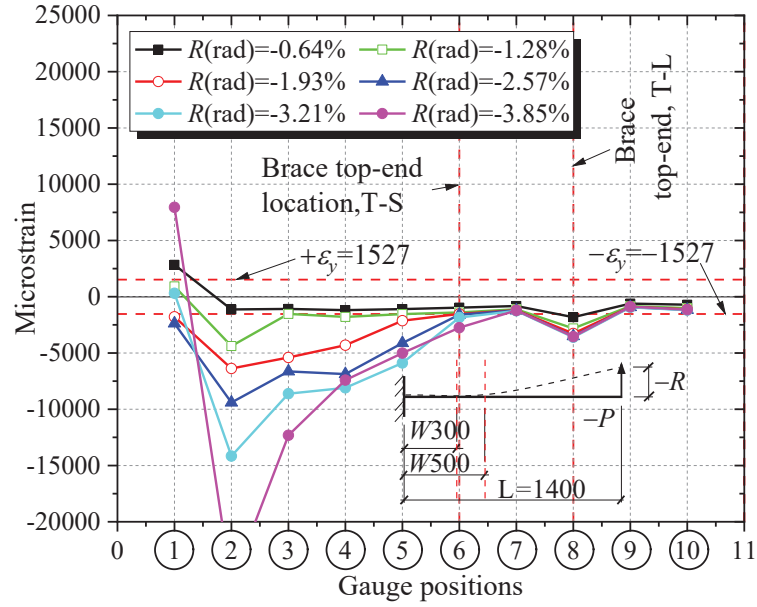


(a) Upper flange for tensile

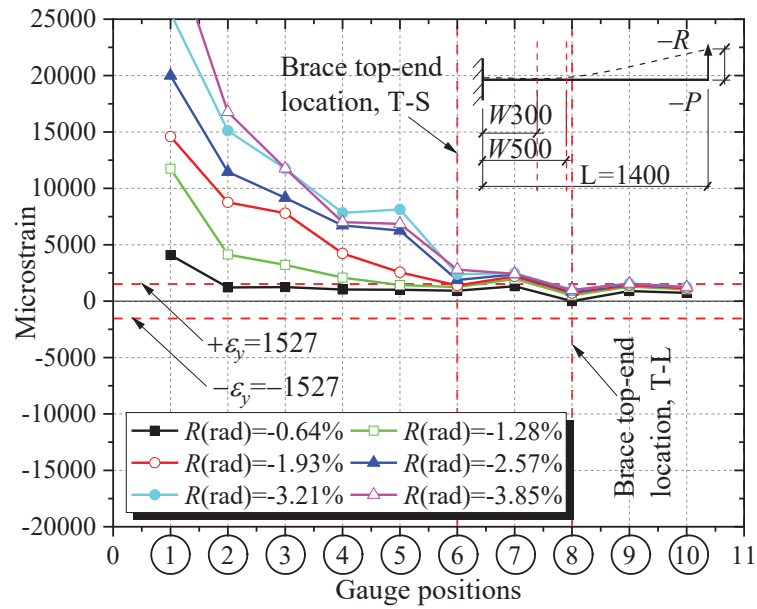


(b) Lower flange for compressive

Fig. 3.11. Strain distributions of the specimen T-N

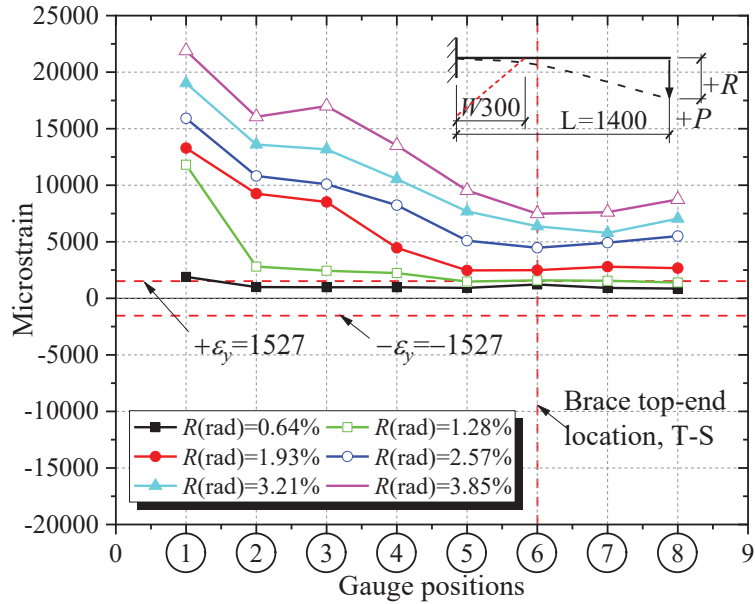


(c) Upper flange for compressive

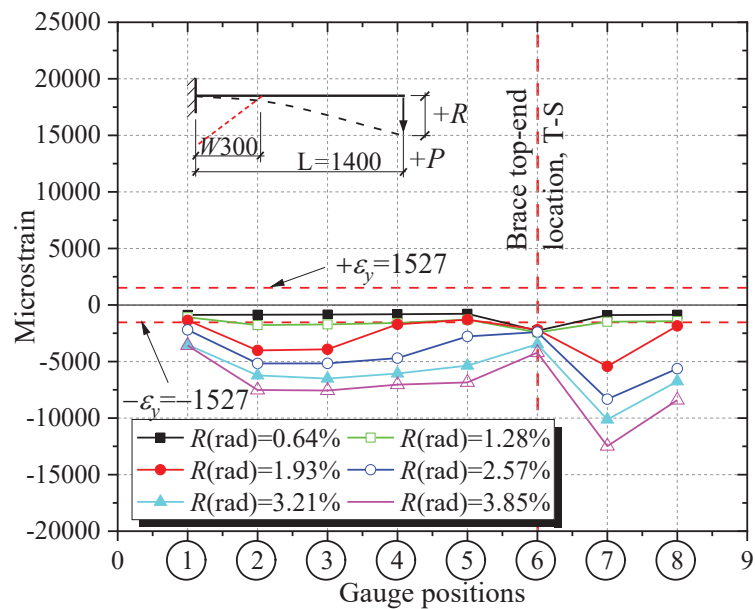


(d) Lower flange for tensile

Fig. 3.11. Strain distributions of the specimen T-N (continued).

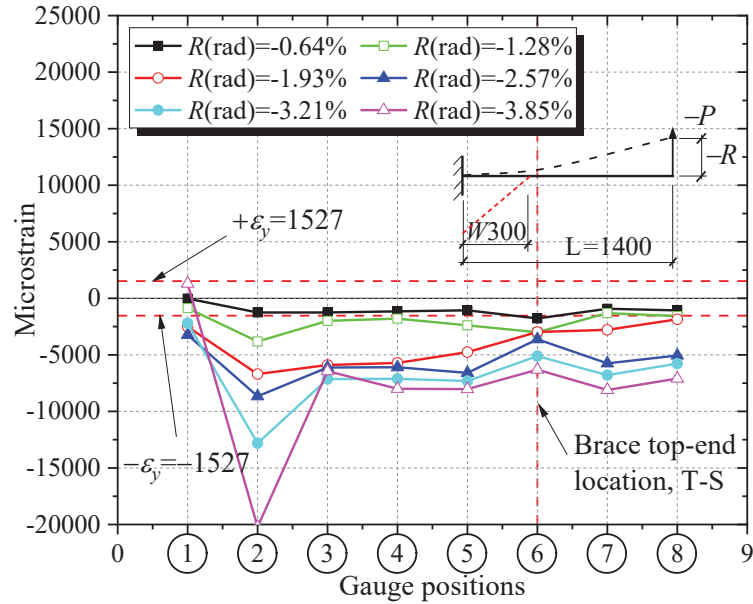


(a) Upper flange for tensile

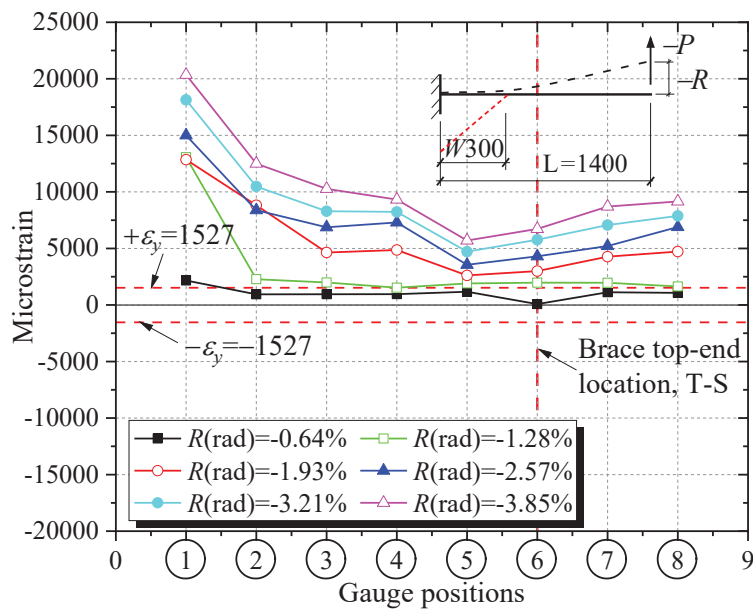


(b) Lower flange for compressive

**Fig. 3.12.** Strain distributions of the specimen T-S.

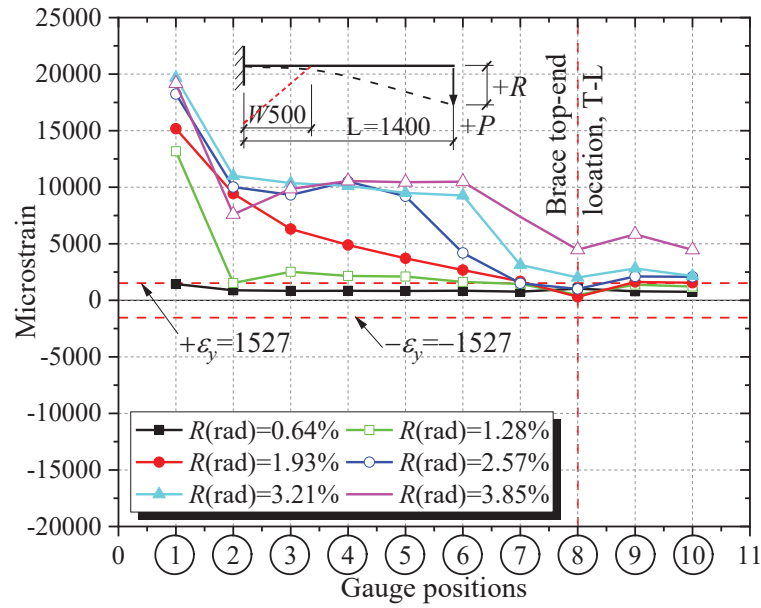


(c) Upper flange for compressive

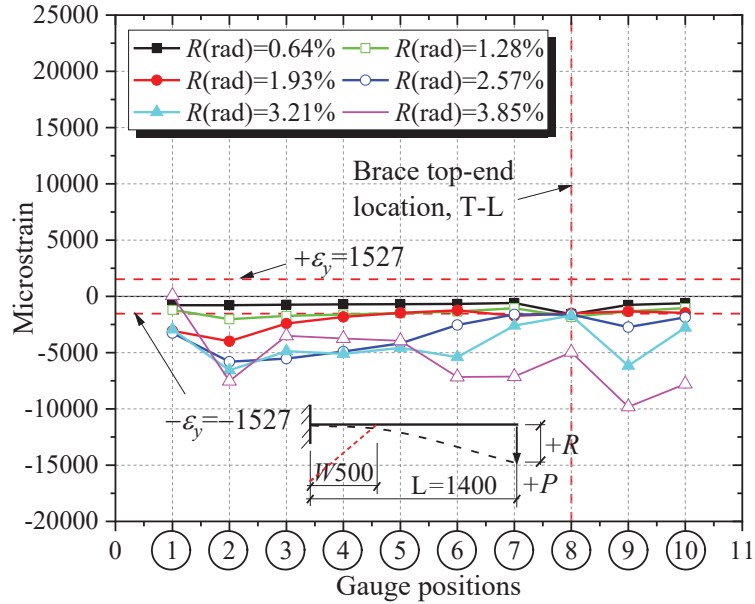


(d) Lower flange for tensile

Fig. 3.12. Strain distributions of the specimen T-S (continued).

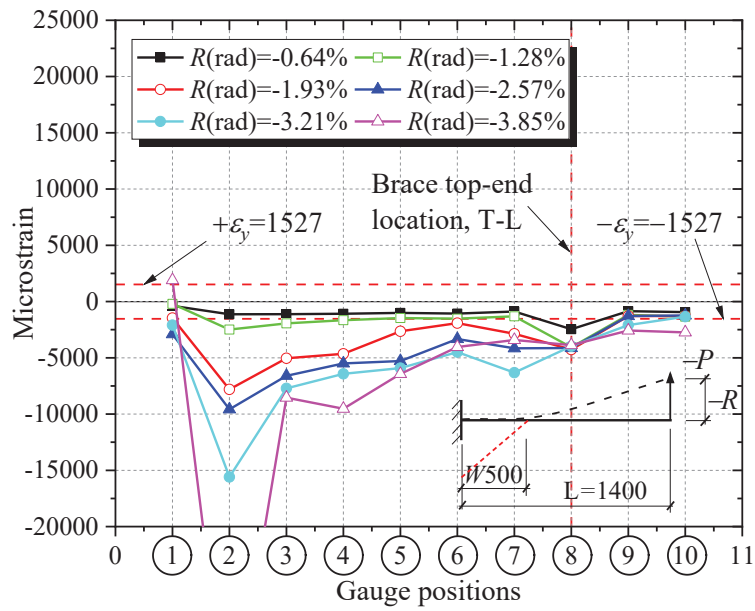


(a) Upper flange for tensile

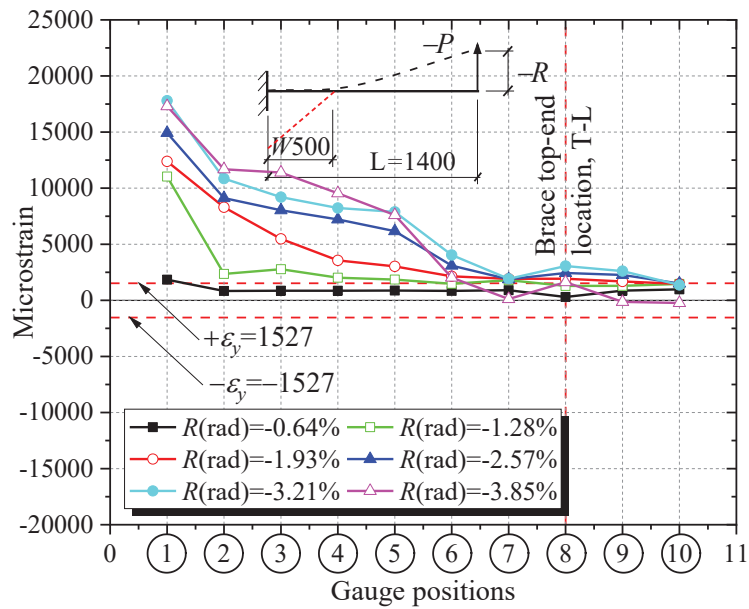


(b) Lower flange for compressive

**Fig. 3.13.** Strain distributions of the specimen T-L.

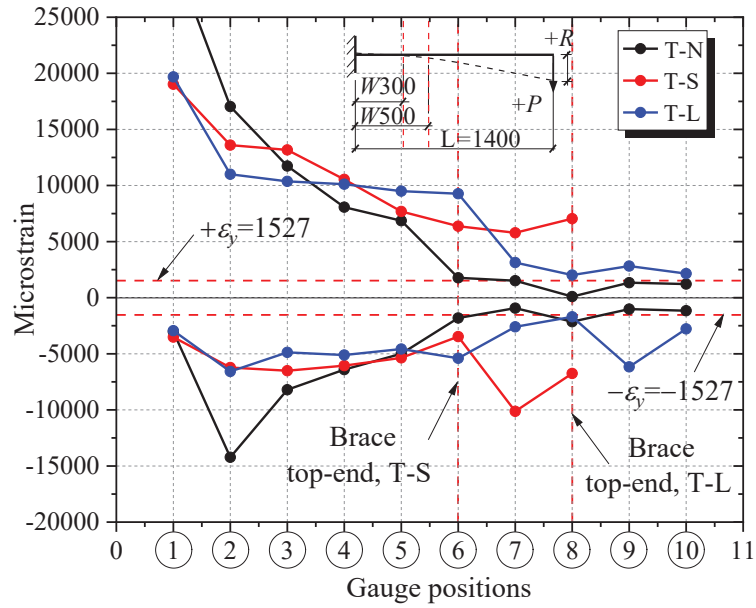


(c) Upper flange for compressive

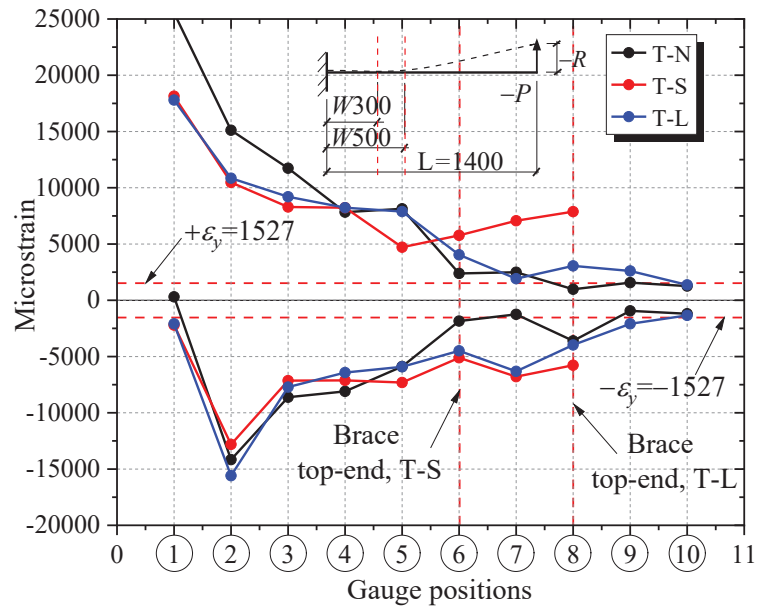


(d) Lower flange for tensile

Fig. 3.13. Strain distributions of the specimen T-L (continued).



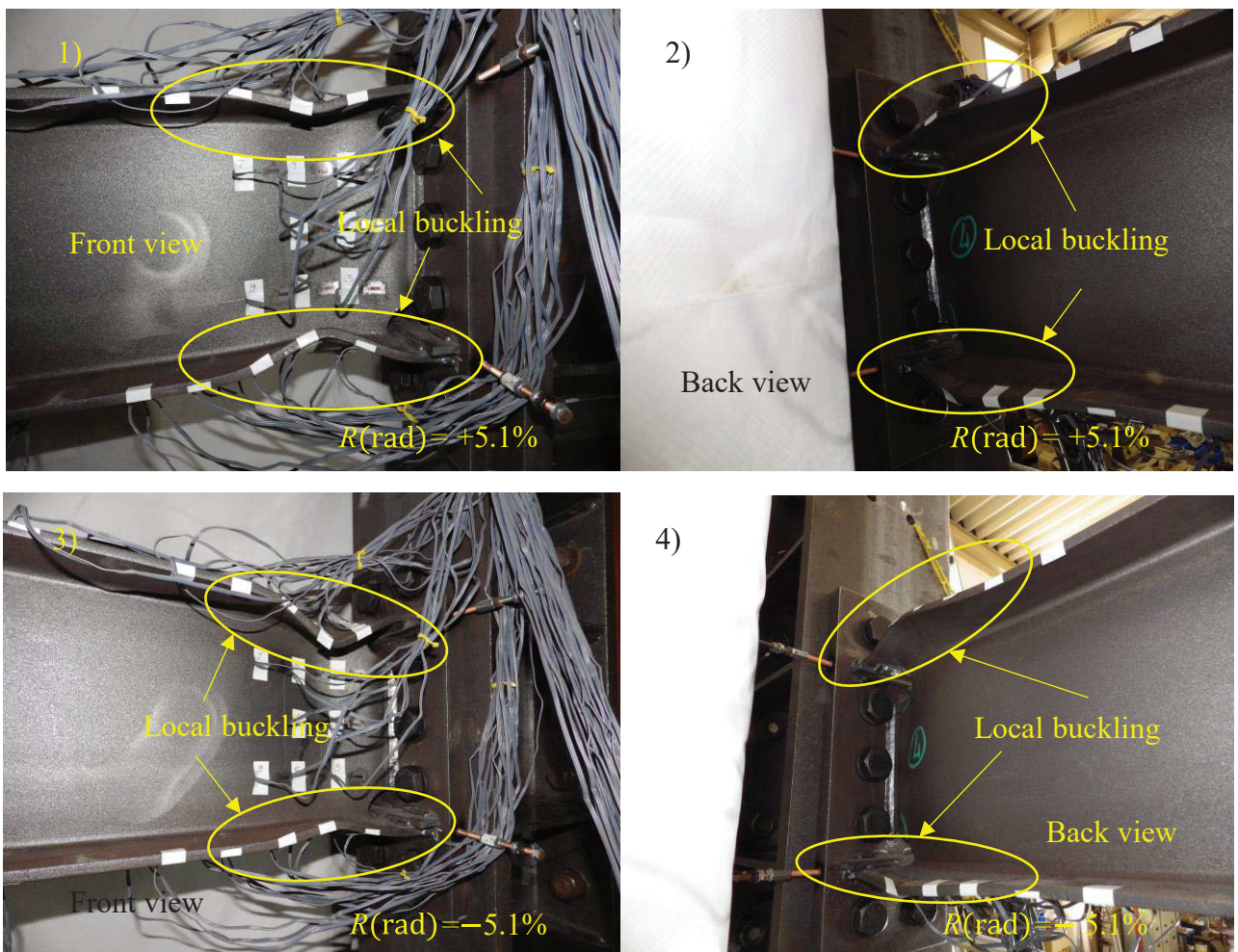
(a) Three specimens for  $R(\text{rad}) = +3.21\%$



(b) Three specimens for  $R(\text{rad}) = -3.21\%$

**Fig. 3.14.** Comparisons of strain distributions along the beam between three specimens for  $R(\text{rad}) = \pm 3.2\%$ .

For the long BRKB specimen T-L, residual deformation occurred in the beam BRKB inner area, as shown in **Fig. 3.15(c)**. The occurrence of local buckling differs from that on the column faces of the other specimens. It can be concluded that a properly sized slender BRKB relative to the beam length can spread plasticity over long distances both inside and outside of the BRKB area under large global relative rotation. Based on these findings, the proposed short BRKB specimen T-S is more effective for the spreading of plasticity on the beam than the other two specimens.

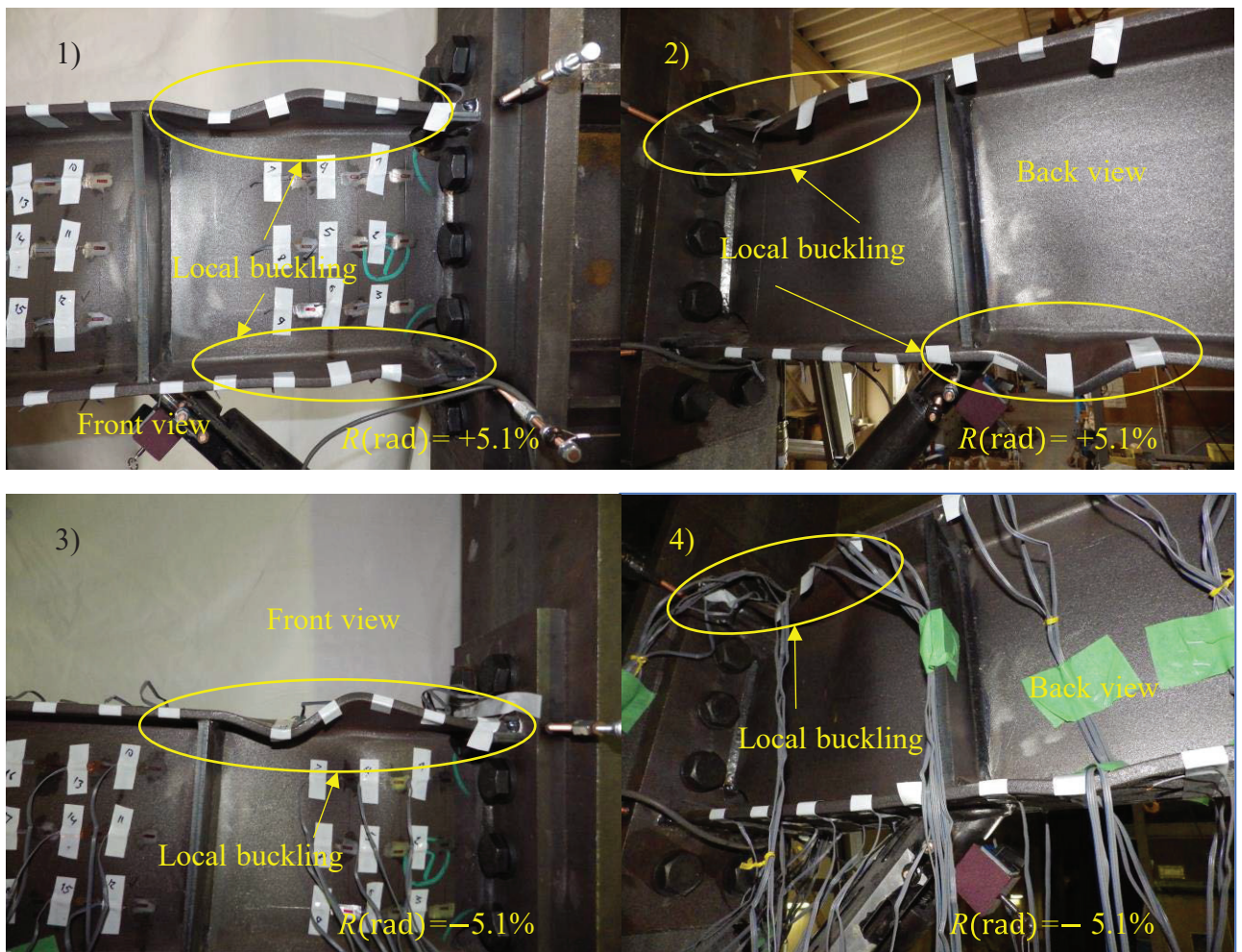


(a) Specimen T-N

**Fig. 3.15.** Residual deformation of beams in the final stage of loading for three specimens.

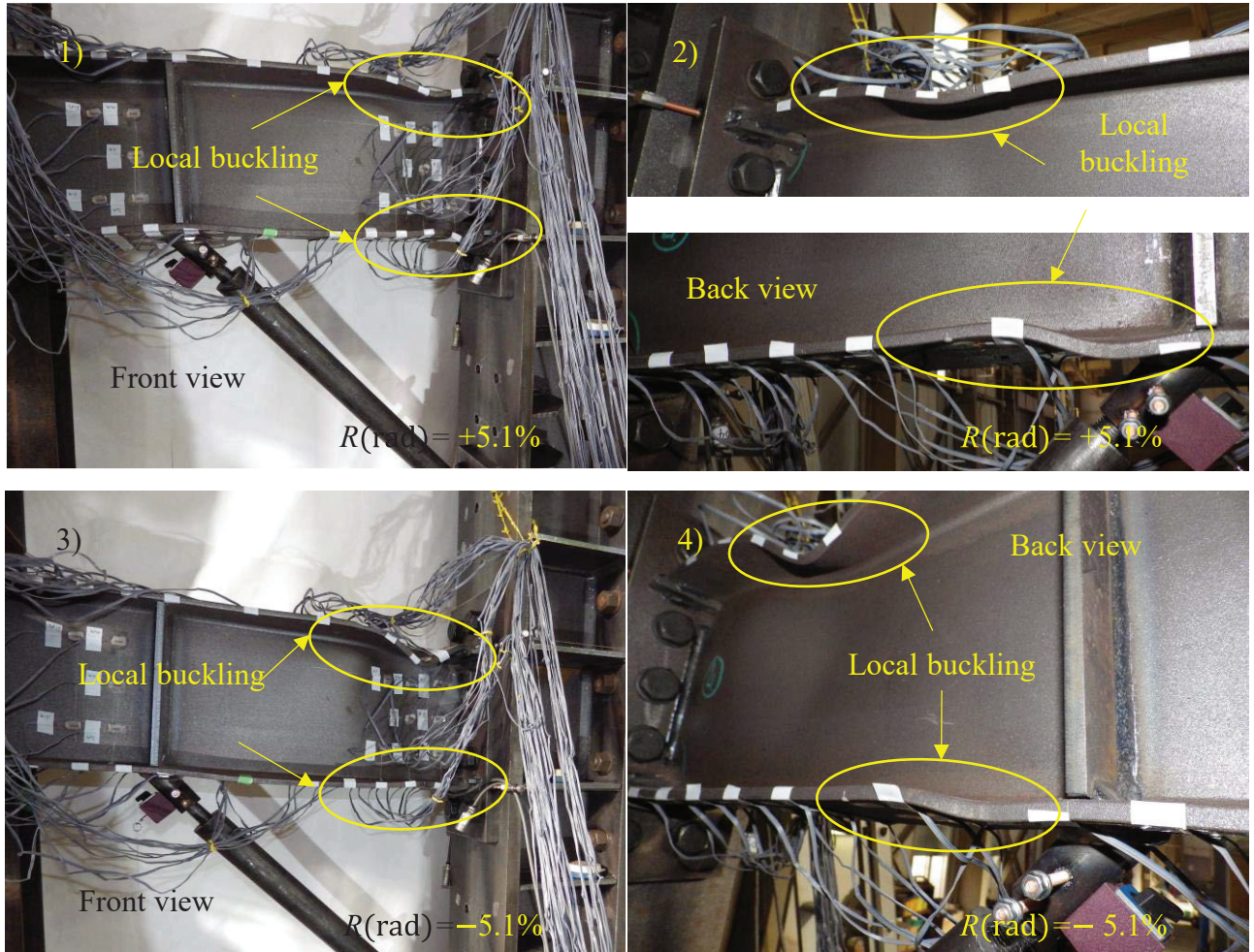


**Fig. 3.16** presents the BRKB behaviors of the T-S and T-L specimens in the latter stages of loading. It can be seen that the ductility of both the shorter and longer braces is satisfactory. No damage can be observed on the exposed screw sections for the shorter brace core bar, indicating that these areas maintained elasticities during our tests, as shown in **Fig. 3.16(a)**. However, for the longer brace, a noticeable bending behavior with minor thread failure is observed in the upper exposed section of the core bar after the cyclic loading test, as depicted in **Fig. 3.16(b)**. The shorter and longer braces adopted the same commercial springs at the lower exposed portion of the core bar to hold the tube restrainer, as depicted in **Fig. 3.2**. Therefore, the weight of the longer brace tube restrainer enlarges the upper contraction allowance zone.



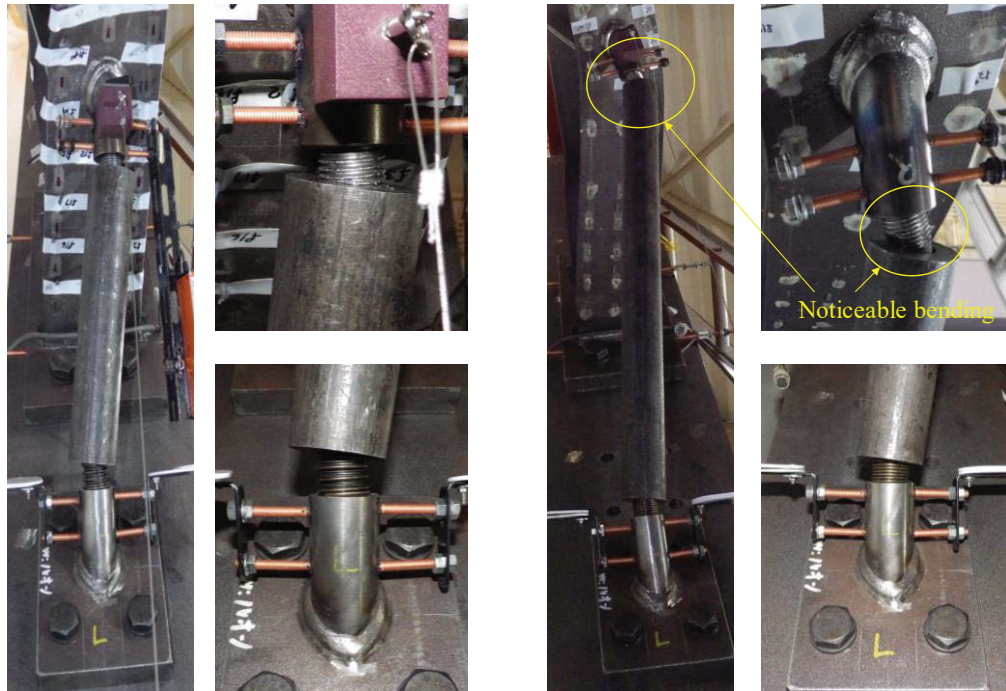
(b) Specimen T-S

**Fig. 3.15.** Residual deformation of beams in the final stage of loading for three specimens (continued).



(c) Specimen T-L

**Fig. 3.15.** Residual deformation of beams in the final stage of loading for three specimens (continued).



(a) BRKB for specimen T-S

(b) BRKB for specimen T-L

**Fig. 3.16.** Residual deformation of BRKBs in the final stage of loading for two specimens.

## 4. NUMERICAL STUDY FOR THE ASSESSMENT OF SPREADING PLASTICITY IN RMC

### 4.1 Scope of the finite element analysis

The main goal of the finite element analysis (FEA) in this study was to examine the spreading of plasticity on beams using diverse parameters for the proposed BRKB that were not considered in the experimental study. To this end, the one-directional one-way loading analysis provided by ANSYS 15.0 [48] was employed in our numerical simulations. RMC models with diverse geometric characteristics for the proposed BRKBs were developed using this software. The analysis results exhibit good agreement with the laboratory testing results discussed in the previous section, as shown in **Fig. 3.10(a)** to **Fig. 3.10(c)**. Slight differences were observed between the test and FEA results, except for the Bauschinger effect due to the bilinear isotropic hardening rules. In addition, the percentage of the difference between the FE analysis and test results in each specimen for the relationship between load and global relative rotation is less than 7% regarding each peak value of the cyclic loadings. Moreover, detailed descriptions of the FEA parameters and results are provided in the following sections.

### 4.2 Element selection

Because shell elements facilitate thin feature modeling, six-degree-of-freedom four-node SHELL181 elements were used for beam modeling. These elements have capabilities for plasticity and large deformation and are relatively easy to mesh. They can also reduce computational expenses to a certain degree. However, depending on the variety of buckling restrainer thicknesses and their interactions with core damper surfaces, SOLID186 (high-order 3D 20-node solid elements that exhibit quadratic displacement) elements were used in our simulations of the BRKB dampers, allowing the bending responses of the dampers to be captured more accurately than those of the shell elements.

Additionally, 3D node-to-surface CONTA175 elements were used between the surface elements in the beam, while 3D eight-node surface-to-surface CONTA174 elements were applied to the solid components in the BRKB model. For the target elements, 3D TARGE170 elements, which are associated with the aforementioned contact elements, were utilized in both the shell and solid elements. **Fig. 4.1** presents the geometric characteristics of the numerical model and its meshing. To achieve the highest possible solution accuracy, hexahedron (hex) meshes were used for all numerical models. Additionally, stress concentration areas, such as scallop regions, were meshed more delicately than the other parts. In **Fig. 4.2**, the core bar damper, restraining tube geometries, and meshing are illustrated in detail. The mesh sizing process began with a course meshing until the mesh was fine

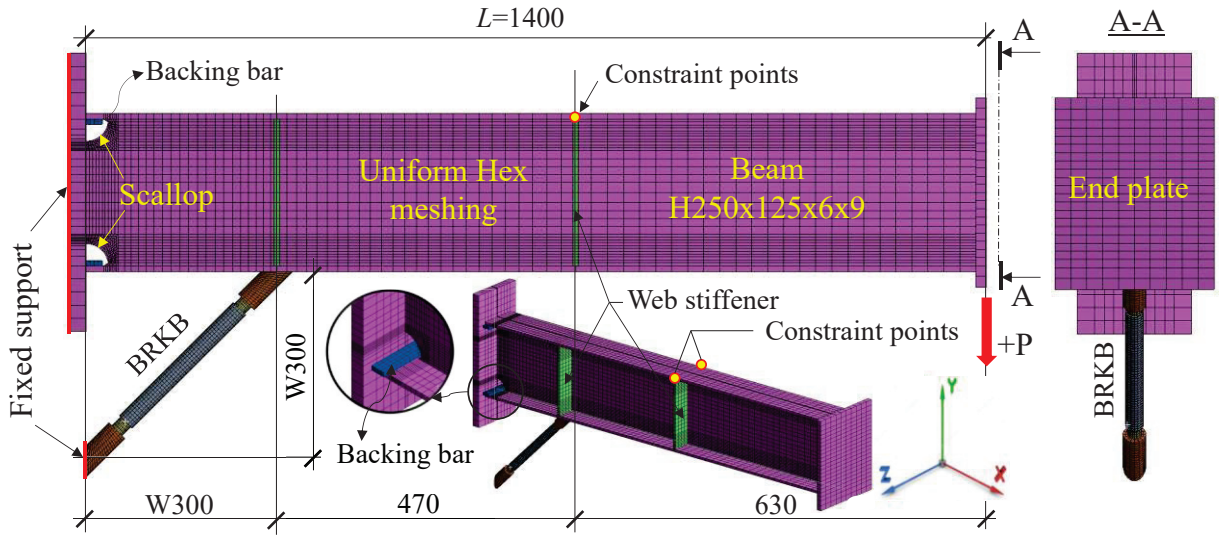
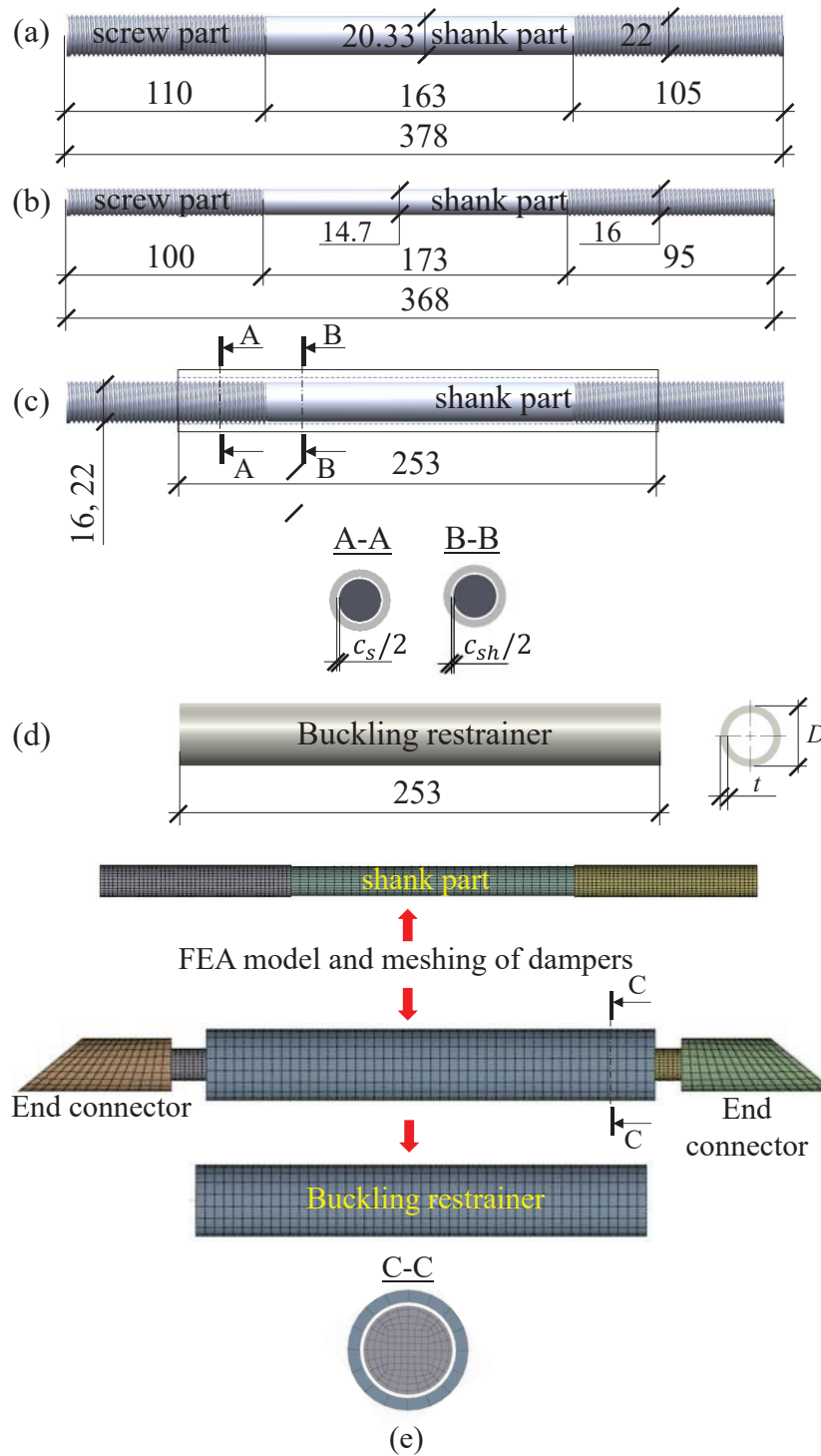


Fig. 4.1. FE model of the proposed BRKB and beam.

enough to prevent any further changes in the observed results. As a result of several attempts of the above-mentioned procedure, sufficient fine mesh sizing for the plasticity-relevant zone was adopted in the FE analysis, as shown in Fig. 4.1. The core bar threads were not considered in our numerical analysis because they were already evaluated in a previous study [37]. This type of screw bar FEA using a simplified model without screws is applicable with high accuracy. The bonded contact assumption described in the following section represents the high-strength screw sections in our numerical analysis.

### 4.3 Key parameters of FEA models

All of the FE BRKB models listed in Table 2 were analyzed and an H-section  $H250 \times 125 \times 6 \times 9$  beam was used in all models. For convenience, each model is numbered and named in the first and second columns, respectively. A total of 30 BRKB models, excluding the base models, were analyzed to investigate the behavior of the distributed plasticity on the beams. Base models such as non-braced and non-restrained models are shown in rows one to three. Here, “c0t0” represents a non-restrained steel bar KB beam model. The characteristics of  $c_s$  and  $c_{sh}$ , and  $t$  represent the clearances between the core bar and restraining tube, and the thickness of the tube, respectively, as shown previously in Fig. 3.3. Because the clearance between the restrainer and the core member strongly affects design performance [43], [49]–[52], determining an appropriate clearance is one of the most important processes for the BRKB damper design. This process was conducted by examining the various safety factors of BRKB beams under compressive loads in our numerical analysis. The parameter  $D / t$  represents the diameter-to-thickness ratios of the restraining tubes. Based on the theory discussed in section 3.2.3, each BRKB model's safety factor (denoted as SF) was determined, as shown in Table 2.



**Fig. 4.2.** Geometry of the BRKB dampers for the FE models:

(a and b) M22W300 and M16W300 shank bars, respectively, (c) complex configuration of the BRKB damper, (d) buckling restrainer, and (e) numerical model of the damper and its meshing.

Table 2 – BRKBs used for FEA

№	Name	BR tube			Clearance				Brace safety factor, SF
		D	t	D/t	Shank part		Screw part		
					$c_{sh}$	$c_{sh}/2$	$c_s$	$c_s/2$	
<b>Base beam models</b>									
1	Non-braced beam (bare beam)								
2	M16W300 - c0t0 (only bar with no BR tube)								
3	M22W300 - c0t0 (only bar with no BR tube)								
M16 steel core bar BRKB beam models									
<b>M16W300 c1t1–t5</b>									
4	M16W300 - c1t1	20	1	20	3.29	1.65	2	1	-0.05
5	M16W300 - c1t2	22	2	11	3.29	1.65	2	1	0.34
6	M16W300 - c1t3	24	3	8	3.29	1.65	2	1	0.78
7	M16W300 - c1t4	26	4	6.5	3.29	1.65	2	1	1.29
8	M16W300 - c1t5	28	5	5.6	3.29	1.65	2	1	1.85
<b>M16W300 c2t1–t5</b>									
9	M16W300 - c2t1	22	1	22	5.29	2.65	4	2	0.03
10	M16W300 - c2t2	24	2	12	5.29	2.65	4	2	0.32
11	M16W300 - c2t3	26	3	8.7	5.29	2.65	4	2	0.64
12	M16W300 - c2t4	28	4	7	5.29	2.65	4	2	1.01
13	M16W300 - c2t5	30	5	6	5.29	2.65	4	2	1.41
<b>M16W300 c3t1–t5</b>									
14	M16W300 - c3t1	24	1	24	7.29	3.65	6	3	0.07
15	M16W300 - c3t2	26	2	13	7.29	3.65	6	3	0.32
16	M16W300 - c3t3	28	3	9.3	7.29	3.65	6	3	0.59
17	M16W300 - c3t4	30	4	7.5	7.29	3.65	6	3	0.89
18	M16W300 - c3t5	32	5	6.4	7.29	3.65	6	3	1.23
M22 steel core bar BRKB beam models									
<b>M22W300 c1t1–t5</b>									
19	M22W300 - c1t1	26	1	26	3.67	1.835	2	1	0.002
20	M22W300 - c1t2	28	2	14	3.67	1.835	2	1	0.31
21	M22W300 - c1t3	30	3	10	3.67	1.835	2	1	0.64
22	M22W300 - c1t4	32	4	8	3.67	1.835	2	1	1.01
23	M22W300 - c1t5	34	5	6.8	3.67	1.835	2	1	1.42
<b>M22W300 c2t1–t5</b>									
24	M22W300 - c2t1	28	1	28	5.67	2.835	4	2	0.04
25	M22W300 - c2t2	30	2	15	5.67	2.835	4	2	0.27
26	M22W300 - c2t3	32	3	10.7	5.67	2.835	4	2	0.52
27	M22W300 - c2t4	34	4	8.5	5.67	2.835	4	2	0.79
28	M22W300 - c2t5	36	5	7.2	5.67	2.835	4	2	1.09
<b>M22W300 c3t1–t5</b>									
29	M22W300 - c3t1	30	1	30	7.67	3.835	6	3	0.06
30	M22W300 - c3t2	32	2	16	7.67	3.835	6	3	0.25
31	M22W300 - c3t3	34	3	11.3	7.67	3.835	6	3	0.46
32	M22W300 - c3t4	36	4	9	7.67	3.835	6	3	0.68
33	M22W300 - c3t5	38	5	7.6	7.67	3.835	6	3	0.93

#### 4.4 Steel materials

The primary material properties used for FEA were the same as those listed in **Table 1**. The von Mises yield criterion was adopted to identify yielding. This criterion obeys the bilinear stress-strain relationship with the isotropic hardening rule, where the hardening ratio is considered to be 0.005. Additionally, material and geometric nonlinearities were adopted in our FE simulations.

#### 4.5 Contact modeling

Modeling the contact interactions between bodies was the most critical component of our numerical analysis. In this study, pairs of contacts were established as follows. Shell assembly meshes such as the web, flanges, and beam end-plate model were connected at their edges using mesh connection contact techniques. This connection method is faster than using contact elements at the edges of surface bodies. Additionally, a bonded contact, which is a linear type of contact, was placed between the brace right screw connector and beam bottom flange. The core bar and brace connectors interacted with the bonded contact. Regarding the small frictional force of the BRKBs, no significant benefits were observed in terms of the strength of the beam models used in this study. Therefore, to reduce the computational expense, the friction forces between the restraining tube and core bar were represented by the greasy surfaces.

#### 4.6 Loading and boundary conditions

As shown in **Fig. 4.1**, a fixed support with six degrees of freedom was established at the BRKB lower connector and beam end. As mentioned previously, monotonic loading analysis using the displacement control method was adopted for our numerical analysis. The displacement at the beam tip was as high as 63 mm (0.045 rad), which is greater than the global relative rotation angle of 0.02 to 0.03 rad. To avoid out-of-plane global buckling of the beam, the displacement in the Z direction was constrained at both the loading position and constraint points on the beam top flange, as shown in **Fig. 4.1**. **Fig. 4.2** presents the geometry of the BRKB damper and its meshing method for our FEA models.

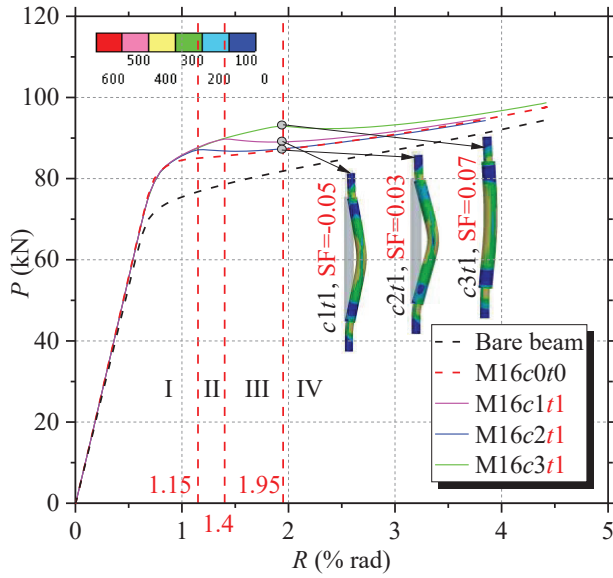
#### 4.7 Analysis results

##### 4.7.1 Effects of the M16 steel bar on overall strength

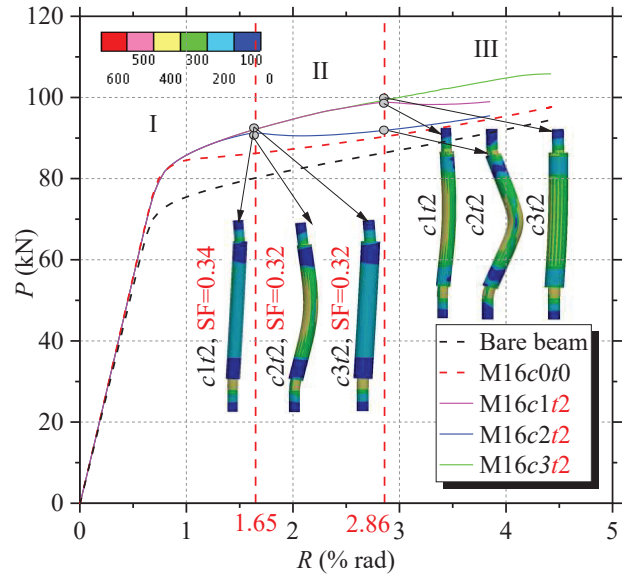
The load-displacement relationships for the different safety factors of our BRKB models are plotted in **Fig. 4.3** and **Fig. 4.4**.

In **Fig. 4.3**, one can see that the M16 steel bar models provide a large safety factor that can significantly enhance the system strength. In these graphs, the red and black dashed lines represent the base model results. To investigate the influence of restraining tubes on the overall strength

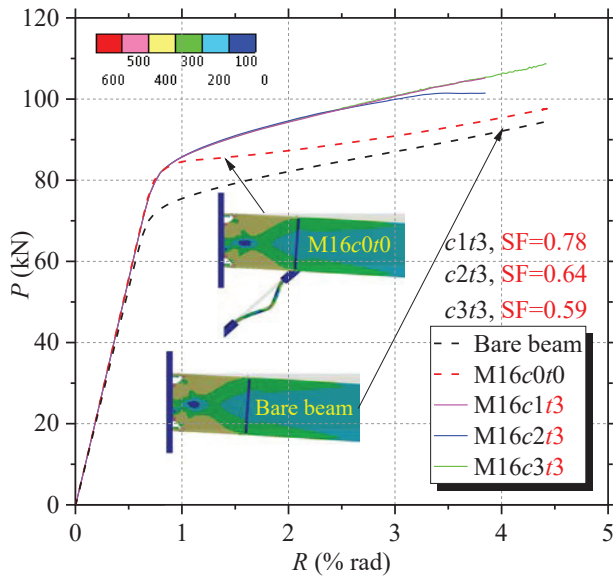




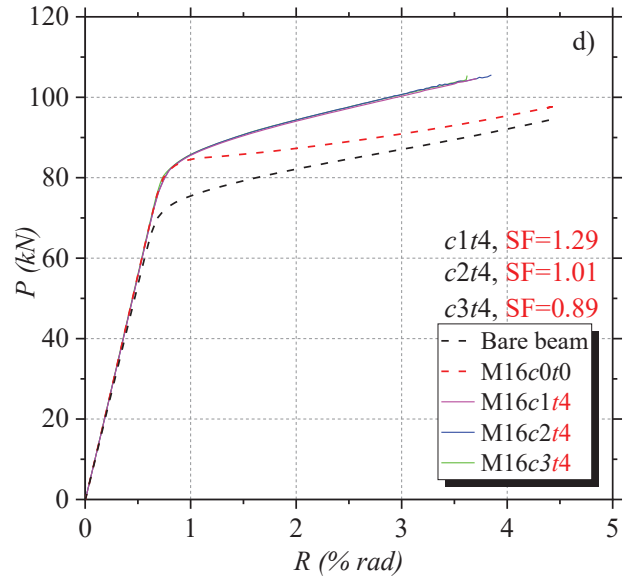
(a) M16W300-c (1,2,3) t1



(b) M16W300-c (1,2,3) t2

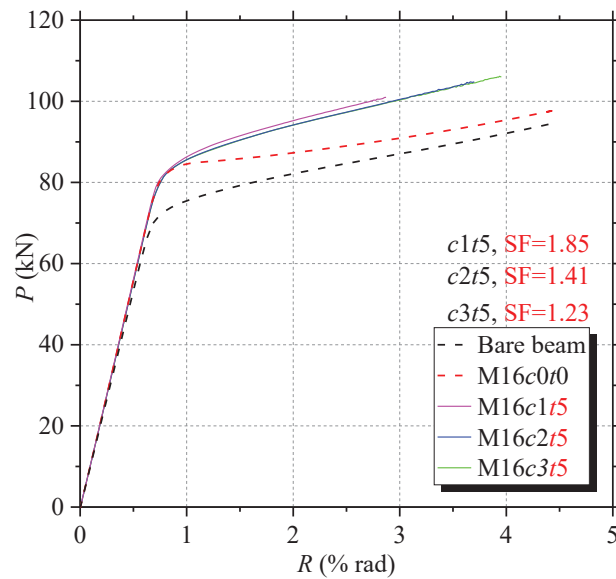


(c) M16W300-c (1,2,3) t3



(d) M16W300-c (1,2,3) t4

**Fig. 4.3.** Relationship between load and global rotation of beams for M16W300-c (1,2,3), t (1,2...5) models.

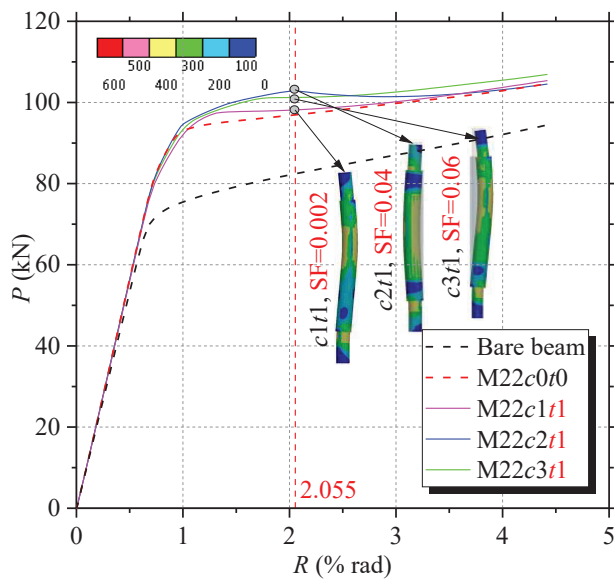
(e) M16W300- $c$  (1,2,3)  $t5$ 

**Fig. 4.3.** Relationship between load and global rotation of beams for M16W300- $c$  (1,2,3),  $t$  (1,2...5) models (continued).

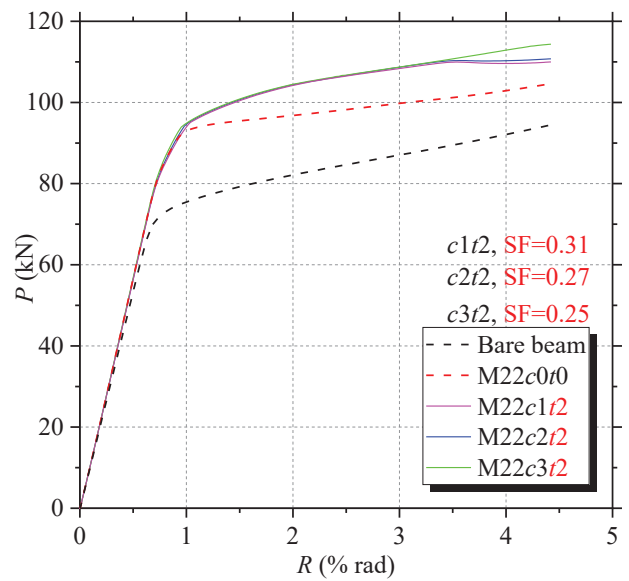
performance of the models, the curved lines were divided into several ranges for the small-safety-factor brace models, as shown in **Fig. 4.3(a)** and **Fig. 4.3(b)**. As a result, the strength variations can be observed more clearly. In each graph, one can see that even a slight increase in the brace safety factor delays strength degradation significantly. The strength degradation of the systems was initiated beyond the ranges “I” corresponding to different global relative rotation angles as a result of brace buckling. It is noteworthy that the small-safety-factor models with large clearances, such as  $c3t1$  (SF = 0.07) and  $c3t2$  (SF = 0.32) exhibit significant load-bearing capacity, as shown in **Fig. 4.3(a)** and **Fig. 4.3(b)**. This can be attributed to the fact that increasing the clearance leads to enhanced tube restrainer stiffness (area moment of inertia). The models with large thicknesses and small clearances, such as  $c2t3$  (SF = 0.64),  $c1t4$  (SF = 1.29),  $c2t4$  (SF = 1.01),  $c1t5$  (SF = 1.85), and  $c2t5$  (SF = 1.41) exhibit adequate strength capacities under the applied loading, as shown in **Fig. 4.3(c)**, **Fig. 4.3(d)**, and **Fig. 4.3(e)**. In such cases, the buckling of the core member is sufficiently restrained.

#### 4.7.2 Effects of the M22 steel bar on overall strength

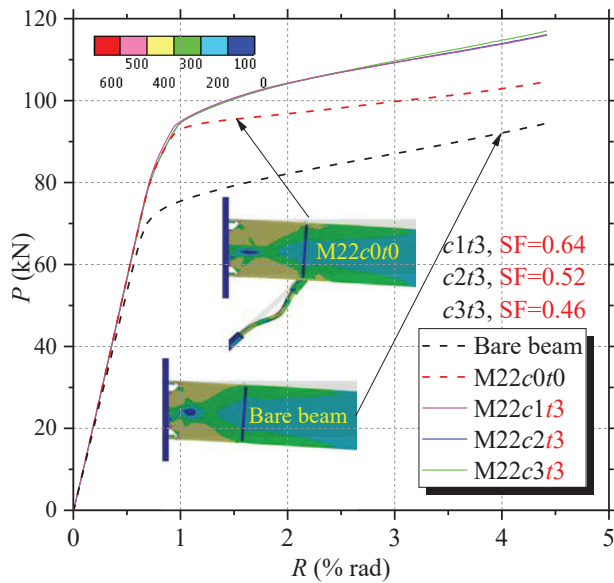
As shown in **Fig. 4.4**, as the steel core bar diameter increases to 22 mm, strength deterioration is noticeably delayed in each load-displacement curve. It is evident that models with  $t = 1$  mm result in greater strength deterioration with respect to the global relative rotation angles. The BRKB buckling behavior is plotted more clearly in **Fig. 4.4(a)**. The design of a slender BRKB with a steel core bar



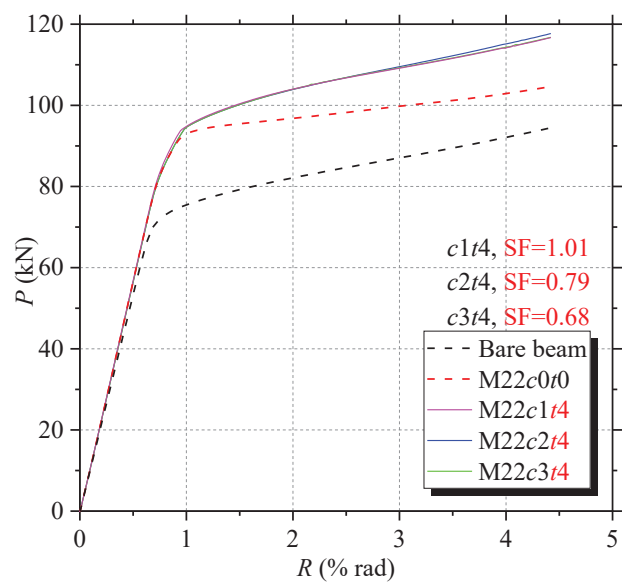
(a) M22W300-c (1,2,3) t1



(b) M22W300-c (1,2,3) t2

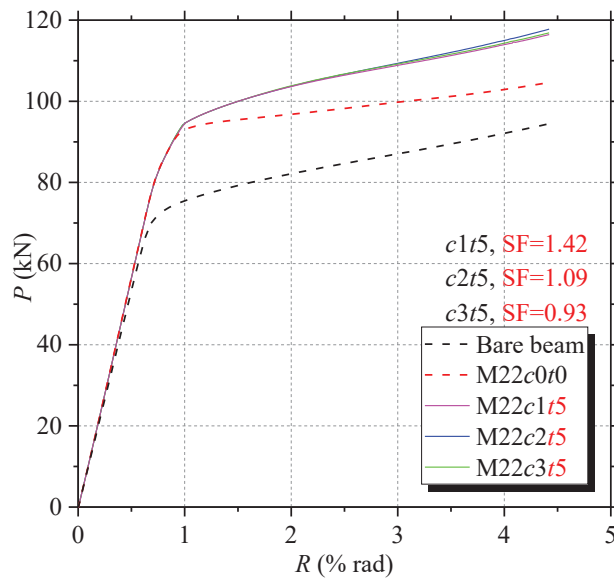


(c) M22W300-c (1,2,3) t3



(d) M22W300-c (1,2,3) t4

**Fig. 4.4.** Relationship between load and global rotation of beams for M22W300-c (1,2,3), t (1,2...5) models.



(e) M22W300-c (1,2,3) t5

**Fig. 4.4.** Relationship between load and global rotation of beams for M22W300-c (1,2,3), t (1,2...5) models (continued).

should be considered when determining the core bar cross-section. The influence of the proposed BRKBs on each model's plasticity development is detailed in the following section.

#### 4.7.3 Stress distributions along the beams

**Fig. 4.5** to **Fig. 4.7** present the equivalent von Mises stress distributions in the final loading stage from our analysis.

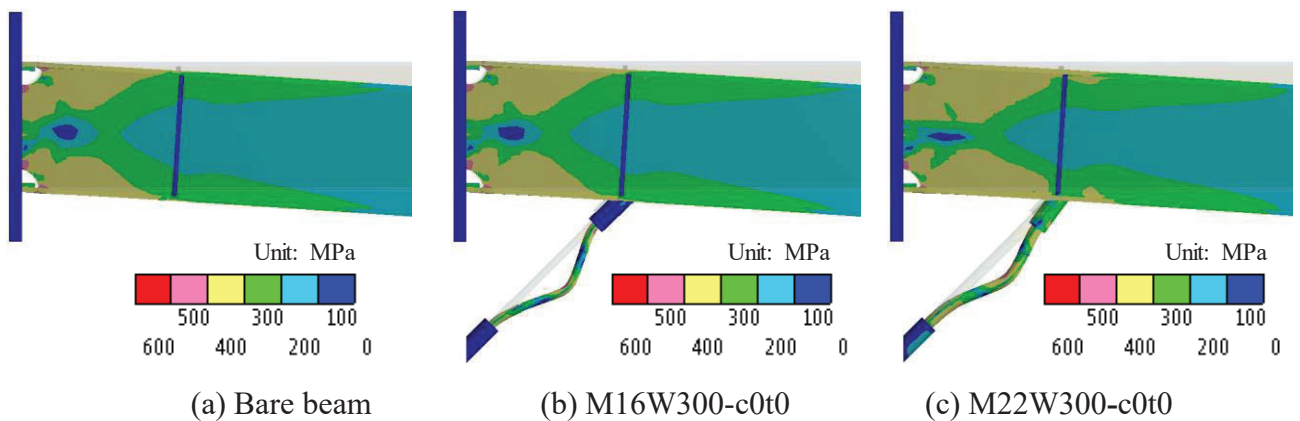


**Fig. 4.5.** Equivalent Von Mises stress distributions in the final stage of loading for the reference models.

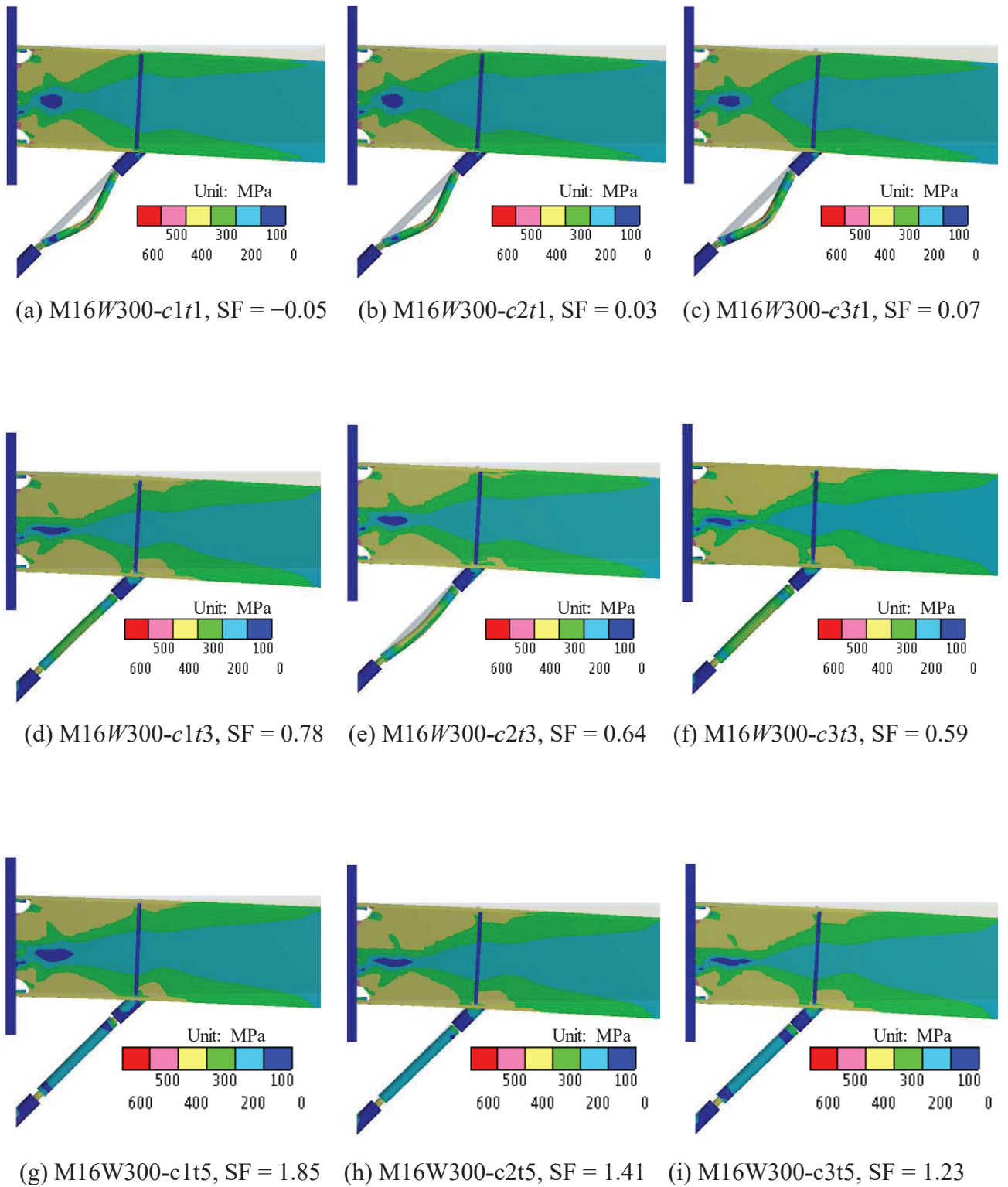


**Fig. 4.6.** Equivalent Von Mises stress distributions in the final stage of loading for the M16 steel core bar BRKBs.

#### 4.7.4 Results for the base beam models

The stress distributions of the base beam models are presented in **Fig. 4.5(a)** to **Fig. 4.5(c)**. The yellow areas in these graphs represent the yielding of each member under external loading. It is apparent that an unrestrained core bar cannot disperse plasticity along the beam under an applied force.

#### 4.7.5 Results for the M16 steel core bar BRKB beam models

**Fig. 4.6(a)** to **Fig. 4.6(i)** present the M16 steel core bar BRKB beam model results, where plastic stresses are dominant in the beam-to-column connection areas of all models. As the safety factor increases to or exceeds one, plasticity is spread along the beam flanges without restrainer yielding, as shown in **Fig. 4.6(g)** to **Fig. 4.6(i)**. Yielding is initiated from the beam-to-column connection area and brace damper simultaneously, followed by slight yielding of the beam flanges in the outer area of the KB. Therefore, our numerical analysis indicates that the thinner steel core bars (M16) have a weaker influence on the spreading of plasticity in the beams.

#### 4.7.6 Results for the M22 steel core bar BRKB beam models

**Fig. 4.7(a)** to **Fig. 4.7(i)** present the results of the equivalent von Mises stress distributions in the final loading stage for the M22 steel core bar BRKB beam models. The majority of the M22 steel core bar BRKB models with large or small safety factors exhibit satisfactory performance for our design purposes by spreading plasticity along the beams. However, for the small-safety-factor models, the restraining tubes exhibited significant instability during our analysis, similar to the M16 models, as shown in **Fig. 4.7(a)** to **Fig. 4.7(f)**. However, the proposed BRKBs with M22 steel core bars and a safety factor greater than or equal to one are able to disperse the plasticity along the beam sufficiently, as shown in **Fig. 4.7(g)** to **Fig. 4.7(i)**. In these cases, yielding is initiated in both the KB and beam inner/outer sections at the brace location simultaneously without brace buckling.

#### 4.7.7 Detailed assessment of the spreading of plasticity in FEA

For all FEA models, the behavior of plasticity spreading in the beams, which depends on the BRKB dimensions, was assessed for the small and large plasticity spreading ranges, as shown in **Table 3**. These ranges correspond to the inner and outer sections of the KBs. First, the three symbols  $\Delta$  (plasticity same as the base model),  $\odot$  (plasticity spreading in the large range), and  $\ominus$  (plasticity spreading in the small range) refer to the range of plasticity spreading in the relevant sections. The performances of the buckling restrainers, which are denoted by the “+” signs in **Table 3**, were assessed based on the elasticity, plasticity, and buckling behavior of each model. Finally, all models were classified into one of three plasticity categories: A (very satisfactory), B (satisfactory), and C (unsatisfactory).

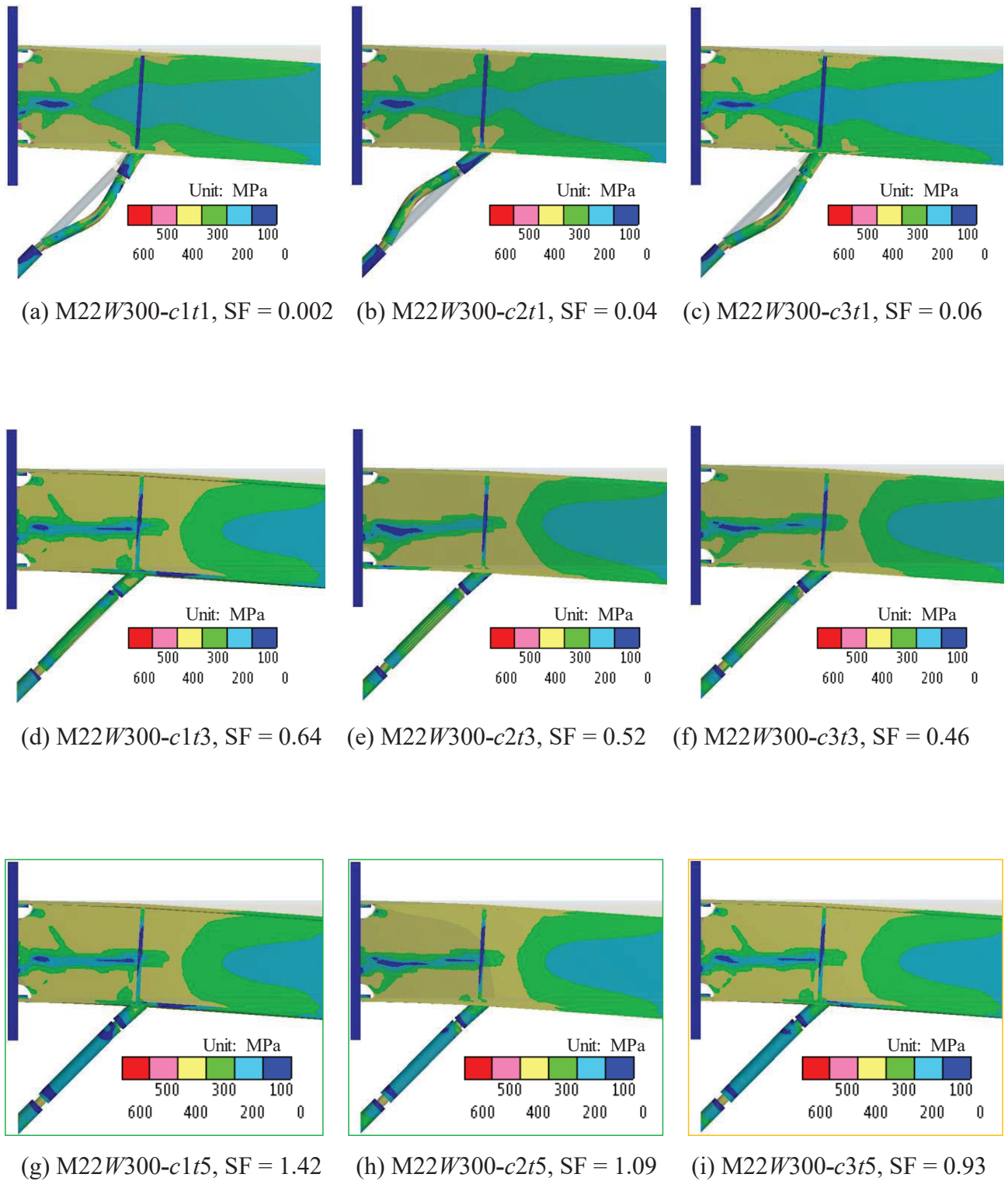


**Fig. 4.7.** Equivalent Von Mises stress distributions in the final stage of loading for the M22 steel core bar BRKBs.

According to these classifications, the three base models are unsatisfactory because the non-restrained steel bars could not spread plasticity under the applied loads. Instead, plasticity was concentrated in the connection areas, as mentioned in Section 4.7.4.

**Table 3**– Assessment of the spreading of plasticity for FEA

№	Name	Plasticity spreading ranges in the beams					Performance of the buckling restrainer			Safety factor	Spreading of plasticity Satisfaction					
		KB inner portion			KB outer portion		Buckled	Under plasticity	Under elasticity		Eq. (3)	A	B	C		
		as base	small	large	small	large										
<b>Base beam models</b>																
<b>1</b>	Non-braced beam (bare beam)												√			
<b>2</b>	M16W300 - c0t0 (only bar with no BR tube)												√			
<b>3</b>	M22W300 - c0t0 (only bar with no BR tube)												√			
<b>M16 steel core bar BRKB beam models</b>																
M16W300 c1t1–t5																
<b>4</b>	M16W300 - c1t1	Δ					+			-0.05			√			
<b>5</b>	M16W300 - c1t2	Δ					+			0.34			√			
<b>6</b>	M16W300 - c1t3			⊙	⊙			+		0.78			√			
<b>7</b>	M16W300 - c1t4			⊙	⊙				+	1.29			√			
<b>8</b>	M16W300 - c1t5			⊙	⊙				+	1.85			√			
M16W300 c2t1–t5																
<b>9</b>	M16W300 - c2t1	Δ					+			0.03			√			
<b>10</b>	M16W300 - c2t2	Δ					+			0.32			√			
<b>11</b>	M16W300 - c2t3			⊙	⊙		+			0.64			√			
<b>12</b>	M16W300 - c2t4			⊙	⊙			+		1.01			√			
<b>13</b>	M16W300 - c2t5			⊙	⊙				+	1.41			√			
M16W300 c3t1–t5																
<b>14</b>	M16W300 - c3t1	Δ					+			0.07			√			
<b>15</b>	M16W300 - c3t2			⊙	⊙		+			0.32			√			
<b>16</b>	M16W300 - c3t3			⊙	⊙			+		0.59			√			
<b>17</b>	M16W300 - c3t4			⊙	⊙			+		0.89			√			
<b>18</b>	M16W300 - c3t5			⊙	⊙				+	1.23			√			

A, B, and C indicate very satisfactory, satisfactory, and unsatisfactory, respectively.

⊙, ⊙, and Δ represent the rates of the spreading of plasticity along the beams for “high,” “low,” and “same as the non-braced base model,” respectively.

For the M16W300 models, excluding the  $t = 1$  and  $t = 2$  models with small tube restrainer thicknesses, the plasticity was spread slightly along the outer portions of the KBs. However, the plasticity spreading ranges in the beams adjacent to the KB outer sections did not increase until the final loading stage. This can be explained by the excessive buckling of the BRKBs, which occurred because the small diameters of the steel core bars could not resist the applied loads, as discussed in



Table 3– Continued

№	Name	Plasticity spreading ranges in the beams					Performance of the buckling restrainer			Safety factor	Spreading of plasticity Satisfaction		
		KB inner portion			KB outer portion		Buckled	Under plasticity	Under elasticity		Eq. (3)	A	B
		as base	small	large	small	large							
M22 steel core bar BRKB beam models													
M22W300 c1t1–t5													
19	M22W300 - c1t1			⊙	⊙		+			0.002			√
20	M22W300 - c1t2			⊙		⊙	+			0.31			√
21	M22W300 - c1t3			⊙		⊙	+			0.64			√
22	M22W300 - c1t4			⊙		⊙		+		1.01			√
23	M22W300 - c1t5			⊙		⊙			+	1.42	√		
M22W300 c2t1–t5													
24	M22W300 - c2t1			⊙	⊙		+			0.04			√
25	M22W300 - c2t2			⊙		⊙	+			0.27			√
26	M22W300 - c2t3			⊙		⊙	+			0.52			√
27	M22W300 - c2t4			⊙		⊙		+		0.79			√
28	M22W300 - c2t5			⊙		⊙			+	1.09	√		
M22W300 c3t1–t5													
29	M22W300 - c3t1			⊙	⊙		+			0.06			√
30	M22W300 - c3t2			⊙		⊙	+			0.25			√
31	M22W300 - c3t3			⊙		⊙	+			0.46			√
32	M22W300 - c3t4			⊙		⊙		+		0.68			√
33	M22W300 - c3t5			⊙		⊙			+	0.93		√	

A, B, and C indicate very satisfactory, satisfactory, and unsatisfactory, respectively.

⊙, ⊙, and Δ represent the rates of the spreading of plasticity along the beams for “high,” “low,” and “same as the non-braced base model,” respectively.

Section 4.7.5. Therefore, all M16W300 models were included in category C for the classification of plasticity.

Our FEA revealed that the M22W300-c1t5 and M22W300-c2t5 models provide very satisfactory performance, as indicated by the green color in Fig. 4.7(g) and Fig. 4.7(h). In these models, the plasticity spreads over wide areas in both the inner and outer sections without BRKB buckling. Therefore, it was concluded that the theoretical safety factor (value of at least one) of the proposed BRKB could be achieved for our design purposes. The half clearance between the screw section of the steel core bar and restraining tube  $c_s/2$  should be controlled in the range of 1 to 2 mm.

## 5. EXPERIMENTAL STUDY FOR THE SLENDER BRKB

### 5.1 General

This chapter developed a novel slender cover-tubed BRKB damper with the steel bar core to spread plasticity around the beam end in the RMC, and experimental verification of its deformation capacity was performed using weld-free beam-to-column connection. The advantages of the proposed damper are reduced weight compared to conventional knee braces or mortar-filled BRKBs and high architectural flexibility for the retrofitting of large-span welded steel moment-resisting systems. It was revealed that the proposed damper could also effectively improve the lateral stiffness of weld-free connection systems. Specifically, by increasing the number of contraction allowances, undesirable failure mechanisms that are global instability and local buckling of the restrainer ends can be suppressed effectively because the more uniform plastic deformation of the core bar can be achieved longitudinally. In other words, the adoption of several contraction allowance zones with the proper design of the cover tubes for the proposed dampers significantly improves the performance of the proposed dampers. The study conducted compression loading tests on nine BRKBs and cyclic loading tests on three full-scale specimens with a weld-free beam-to-column connection. The test results are discussed, emphasizing the deformation capacities of the proposed dampers.

### 5.2 Outline of the proposed BRKB dampers

**Fig. 5.1** presents possible configurations of the structural system with the proposed novel slender BRKB damper. In some cases, retrofitting is more complex and difficult to organize because of the extreme diversity and the aesthetic focus on the structural integrity in existing buildings and obstacles of the non-structural or structural elements such as wall and bolted connection of the column-tree connection. **Fig. 5.1(a)** presents an application of the BRKB for either retrofitting or strengthening the column-tree connection. Likewise, the proposed damper can be applied to the pin-connection interior or external steel frames, as shown in **Fig. 5.1(b)** and **Fig. 5.1(c)**, to dissipate the seismic input energy during ground motion. In this weld-free system (pin connection), the beams are connected to the column flanges only at the top flanges by T-stub members with bolts. The beams rotate about the ends of their top flanges. As a result of implementing the BRKB in a weld-free system, the damper can freely deform without causing significant damage to the beams, floor slab, and other non-structural members under excessively large story drifts. Therefore, in Section 5.7, a description of an experimental study in which only a weld-free connection is used with BRKBs to reveal the cyclic response of the proposed dampers is provided.

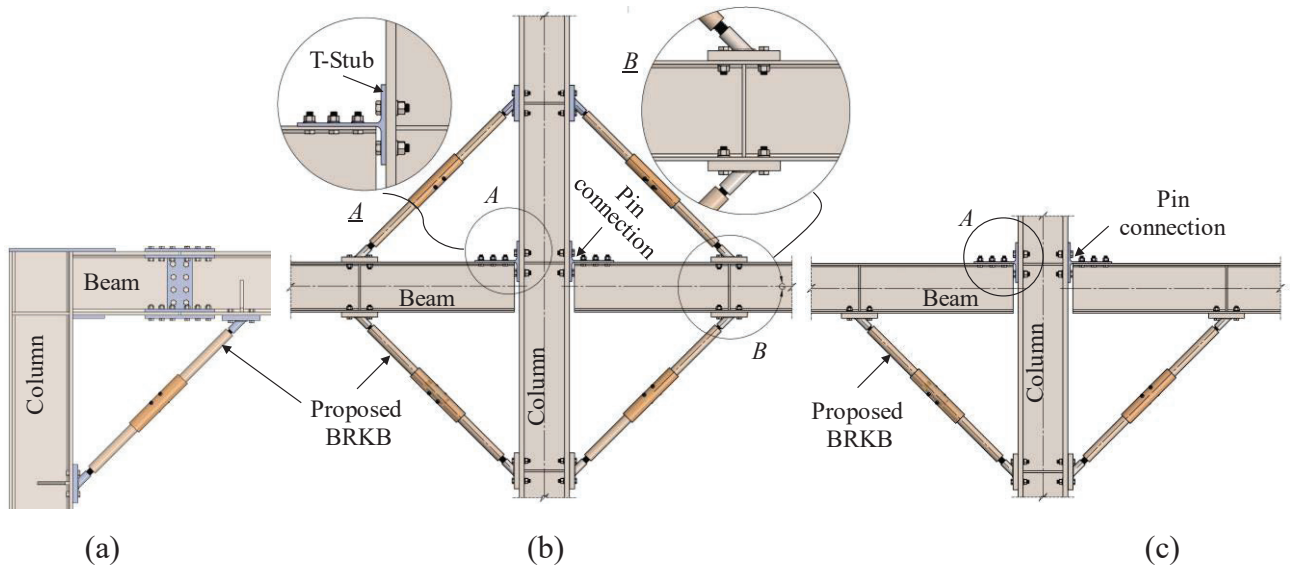


**Fig. 5.1.** Structural configuration of the proposed system:

(a) bracing for the column-tree connection; (b) double-side bracing; and (c) single-side bracing.

### 5.3 Details of the proposed BRKBs

The configuration of the proposed BRKB is shown in **Fig. 5.2**. **Fig. 5.3** shows the details and exploded view of the proposed damper, where each element of the BRKB is numbered from 1 to 11. The roll-threaded ends of the steel bar cores **2** and **3** are connected by a central coupler **1** and placed inside detached round steel tubes **5** and **6** (buckling restrainers). The coupler acts as a connector and transmits the force from one core bar to another. Buckling restrainer tubes with sufficient stiffness and strength are set outside the core bars to ensure the stability of the steel core bars. For ease of construction, one of the steel bar cores is threaded by right screws at its ends, and the other is threaded by right and left screws at its ends. The two opposing screws make available adjustment capabilities during the erection process. In addition, a sufficient-strength steel cover tube **8** is placed at the center of the damper and locked by Allen bolts **9** to ensure the damper remains stable under axial loading, as shown in **Fig. 5.2**. The relative movement of the cover tube along the longitudinal direction of the damper is prevented by four pieces of the Allen bolts screwed through the central coupler. In this study, four contraction allowances, as indicated by the roman numbers I, II, III, and IV, are adopted in the proposed BRKB based on preceding experimental experience [29], [38], [40]. These contraction allowances provide high flexibility to the steel bar core during applied loading conditions. Two pieces of commercial springs **4** and **7** are inserted into the core bars at the lower construction allowance zones to hold the tube restrainer during the loading tests, as shown in

**Fig. 5.2**, in regions I and III. Finally, the left and right screw connectors [10] and [11] are attached to the assembled damper to achieve sufficient holding force during earthquakes. **Fig. 5.4** presents explanations of the step-by-step built-up processes of the proposed damper.

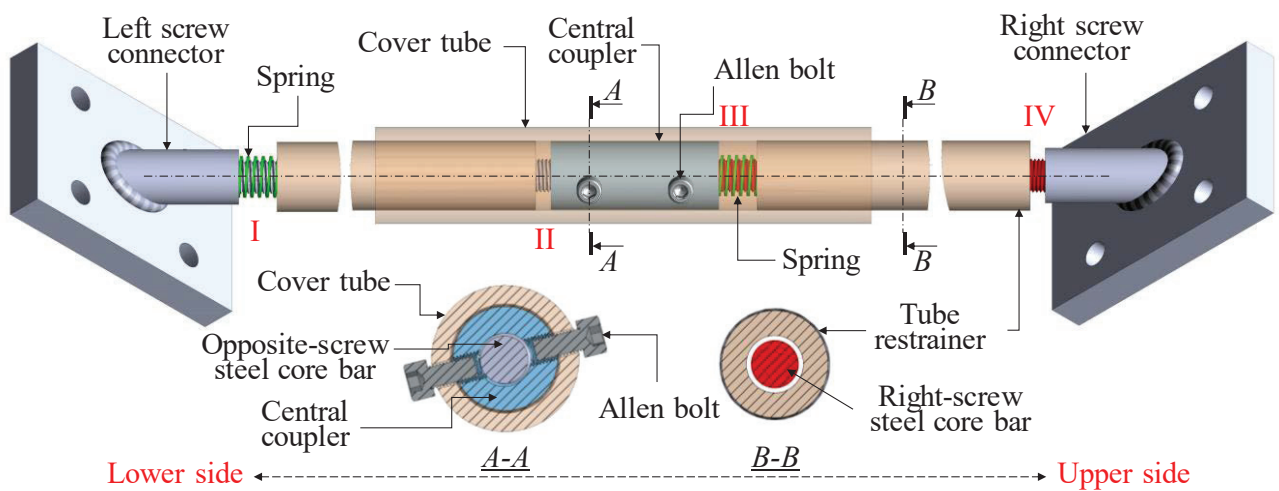


**Fig. 5.2.** Configuration of the proposed buckling-restrained knee brace (BRKB) damper

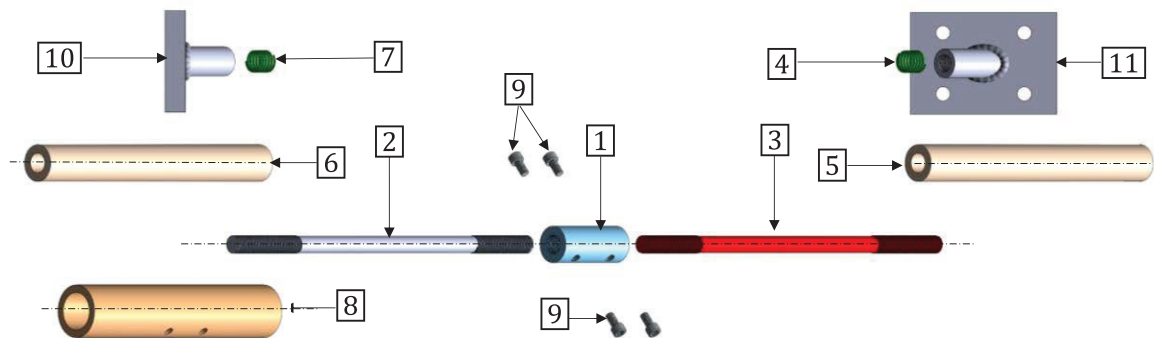


**Fig. 5.3.** Details and exploded view of the proposed damper.

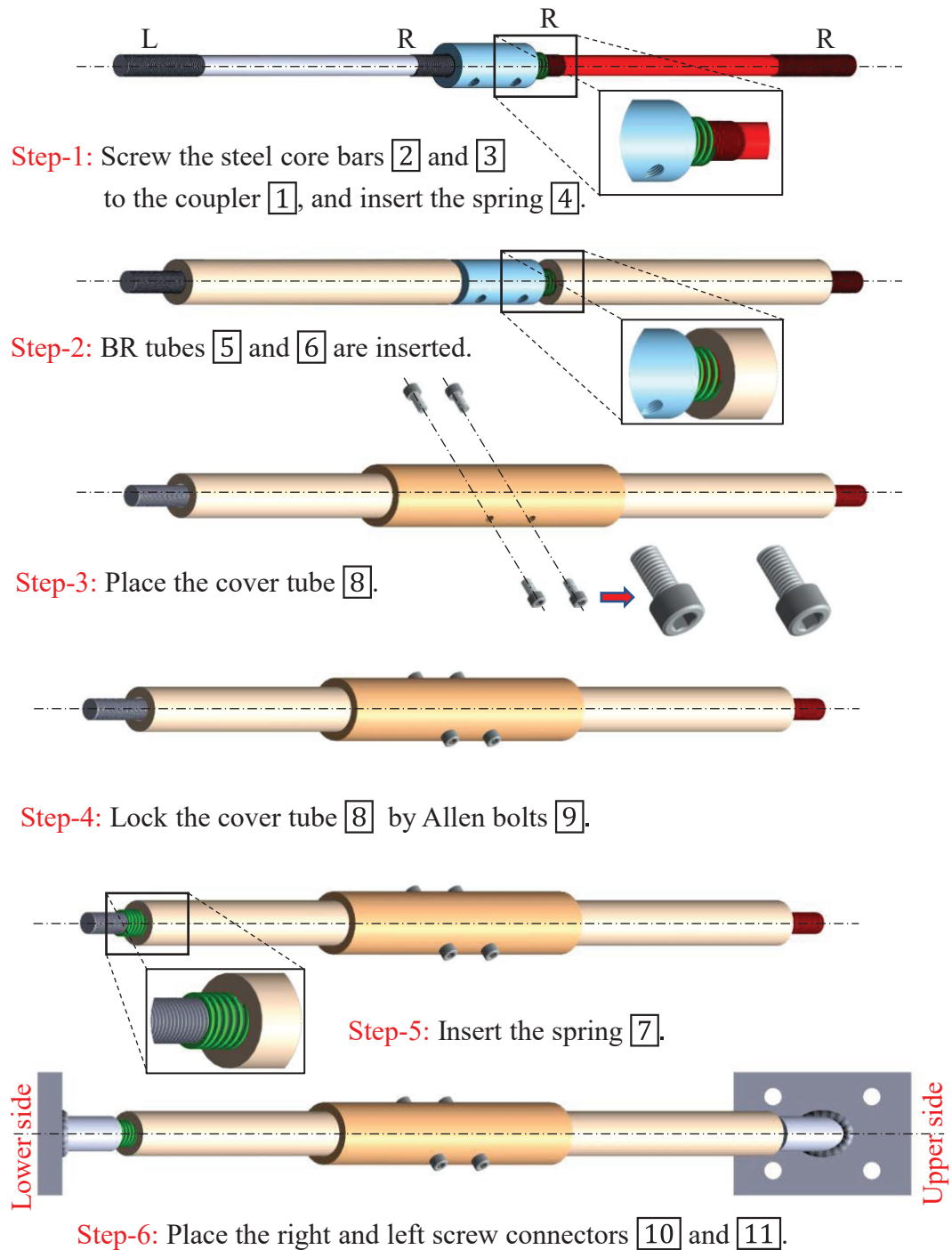


**Fig. 5.4.** Process followed to build the proposed damper.

### 5.4 Design method for the proposed damper

Fig. 5.5 presents the geometrical parameters of the proposed BRKBs. First, a superior stiff buckling restrainer for the base damper (L-BR) (Fig. 5.5(a) and Fig. 5.5(b)) was selected based on the theory discussed in previous Section 3.2.3 [41], [43]. For example, the flexural rigidity and yield strength of the restrainer were designed with a safety factor, SF, utilizing the design method described in Section 3.2.3.

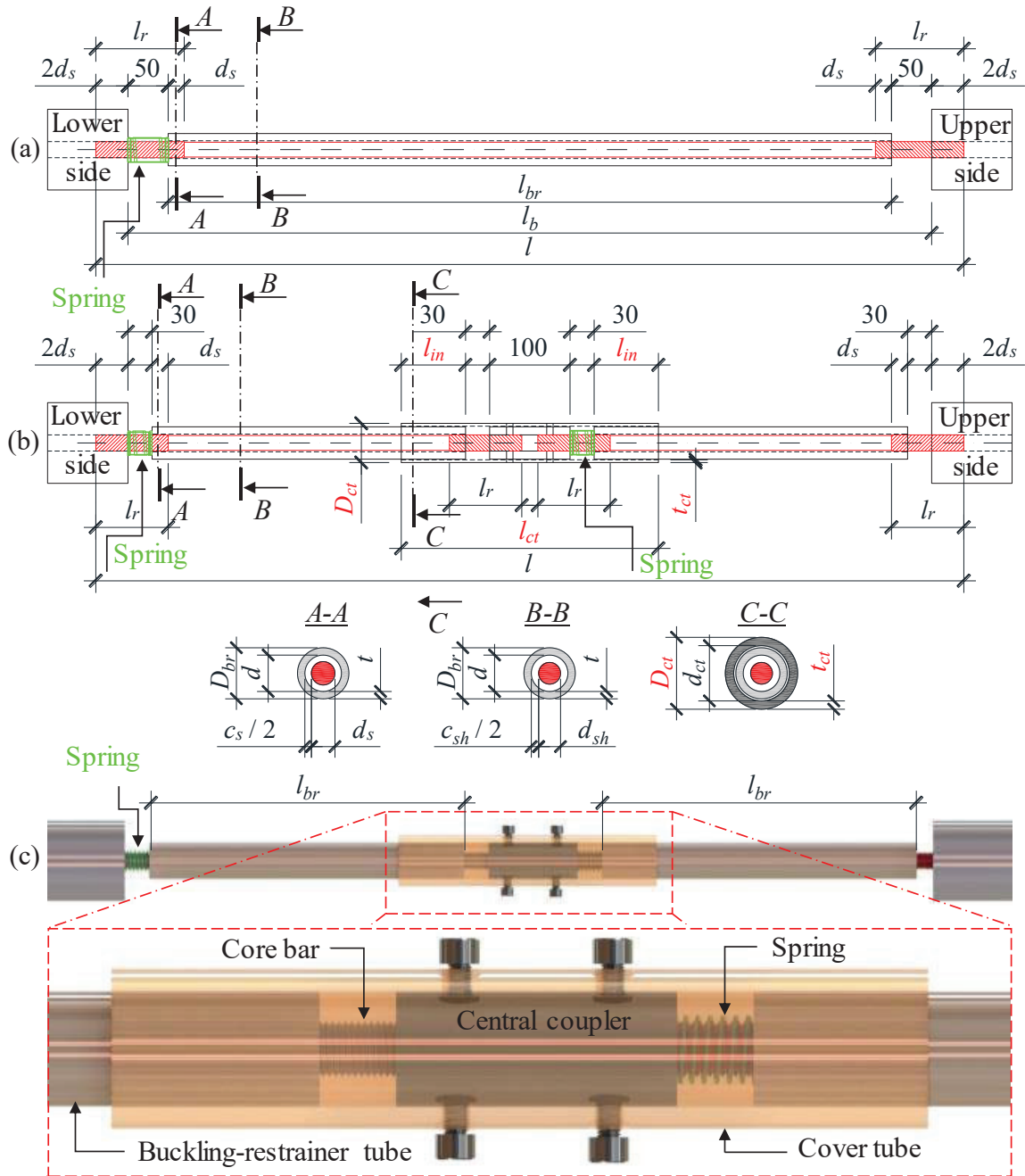


Fig. 5.5. Geometrical parameters of the proposed BRKB dampers:

(a) Base damper, (b) proposed damper, and (c) detailed view of the proposed damper.

The steel bar core was considered to be relatively flexible in the proposed damper. A sufficiently stiff restrainer is expected to restrain the buckling amplitude of the steel bar core under compression loads without rippling. The threaded sections of the steel bar core were inserted through the connector at a distance of  $2d_s$  for both the compression and cyclic loading tests, where  $d_s$  expresses the diameter of the threaded section. In contrast, the insertion length of the threaded sections in the buckling restrainer must satisfy the following condition: if the rotation angle of the connection reaches 0.03 radian, the shank part should not be exposed [37]. In this regard, the insertion lengths of the threaded parts into the buckling restrainer were designed with a dimension of  $2d_s$  in the cyclic loading test, whereas only  $d_s$  could be adopted in the compression tests. Two contraction allowance zones were adopted for the base damper (L-BR specimen, which is discussed in Section 5.5.1), considering the expected axial deformation of the steel bar core under given loads.

**Fig. 5.5(b)** and **Fig. 5.5(c)** show the proposed cover-tubed BRKB. As the number of contraction allowance zones was increased, the efficacy and performance of the damper were expected to become more satisfactory [40]. Thus, the central coupler split the base damper into two parts. Four contraction allowance zones were employed. A detailed description of the proposed damper is presented in Section 5.3. To ensure stability of the proposed damper, a cover tube with an outer diameter  $D_{ct}$  and thickness  $t_{ct}$  was utilized, as shown in **Fig. 5.5(b)**. To obtain the optimal parameters of the cover tubes, the ratio of the section modulus corresponding to the buckling restrainer and cover tubes was considered. A cover tube with a larger elastic section modulus than the buckling restrainer can probably support a load that is capable of inducing flexural loads in the buckling restrainer that are then transferred to the cover tubes. This ratio can be determined by Eq. (5.1).

$$R_{ct} = \frac{Z_{ct}}{Z_{br}} \quad (5.1)$$

where  $Z_{ct}$  and  $Z_{br}$  are the elastic section modulus of the cover and buckling restrainer tubes, respectively, which are defined by Eqs. (5.2) and (5.3), respectively:

$$Z_{ct} = \frac{\pi(D_{ct}^4 - d_{ct}^4)}{32D_{ct}} \quad (5.2)$$

$$Z_{br} = \frac{\pi(D_{br}^4 - d^4)}{32D_{br}} \quad (5.3)$$

$D_{ct}$  and  $d_{ct}$  are the outer and inner diameters of the cover tube, respectively, and  $D_{br}$  and  $d$  are the outer and inner diameters of the buckling restrainer, respectively, as shown in the section views in Fig. 5.5(b).

## 5.5 Compression tests

### 5.5.1 Test specimens

Compression tests were conducted on nine specimens, including the base damper (L-BR), to reveal the load-bearing capacities of the proposed BRKB. The proposed damper specimens differed in the geometrical parameters of their cover tubes, such as the insertion length,  $l_{in}$ , and cross sections. Fig. 5.6 shows the geometrical dimensions of all the specimens, while Table 4 summarizes the detailed characteristics of the specimens.

**Table 4**– Geometrical parameters of the test specimens used in the compression loading tests

	Name	Cont. allow.	Core bar			Buckling Restrainer tube			Cover tube					
			Quantity	Screw diameter, $d_s$ (mm)	Screw length, $l_r$ (mm)	Core length, $l$ (mm)	Outer diameter, $D_{br}$ (mm)	Thickness, $t$ (mm)	Length, $l_{br}$ (mm)	Outer diameter, $D_{ct}$ (mm)	Thickness, $t_{ct}$ (mm)	Inner diameter, $d_{ct}$ (mm)	Length, $l_{ct}$ (mm)	Insertion length, $l_{in}$ (mm)
<b>Group1 (Reference specimens)</b>														
1	N-BR	-	M20	110	1080									
2	L-BR	2	M20	110	1080	40	9	900						
3	S-BR	4	M20	90	530	40	9	390						
<b>Group2 (Short cover tube specimens)</b>														
4	SCT48-D	4	M20	90	530	40	9	390	48.6	3.5	41.6	240	40	
5	SCT54-D	4	M20	90	530	40	9	390	54	6	42	240	40	
6	SCT57-D	4	M20	90	530	40	9	390	57	8	41	240	40	
<b>Group3 (Long cover tube specimens)</b>														
7	LCT48-2D	4	M20	90	530	40	9	390	48.6	3.5	41.6	320	80	
8	LCT54-2D	4	M20	90	530	40	9	390	54	6	42	320	80	
9	LCT57-2D	4	M20	90	530	40	9	390	57	8	41	320	80	

Abbreviations. ABR: Specifications of structural double-threaded anchor bolts. STKMA: Steel grade for structural steel tubes.

In general, the specimens were categorized into three groups: reference, short cover tubes (SCT), and long cover tube specimens (LCT). The reference specimens were assumed to consist of only the



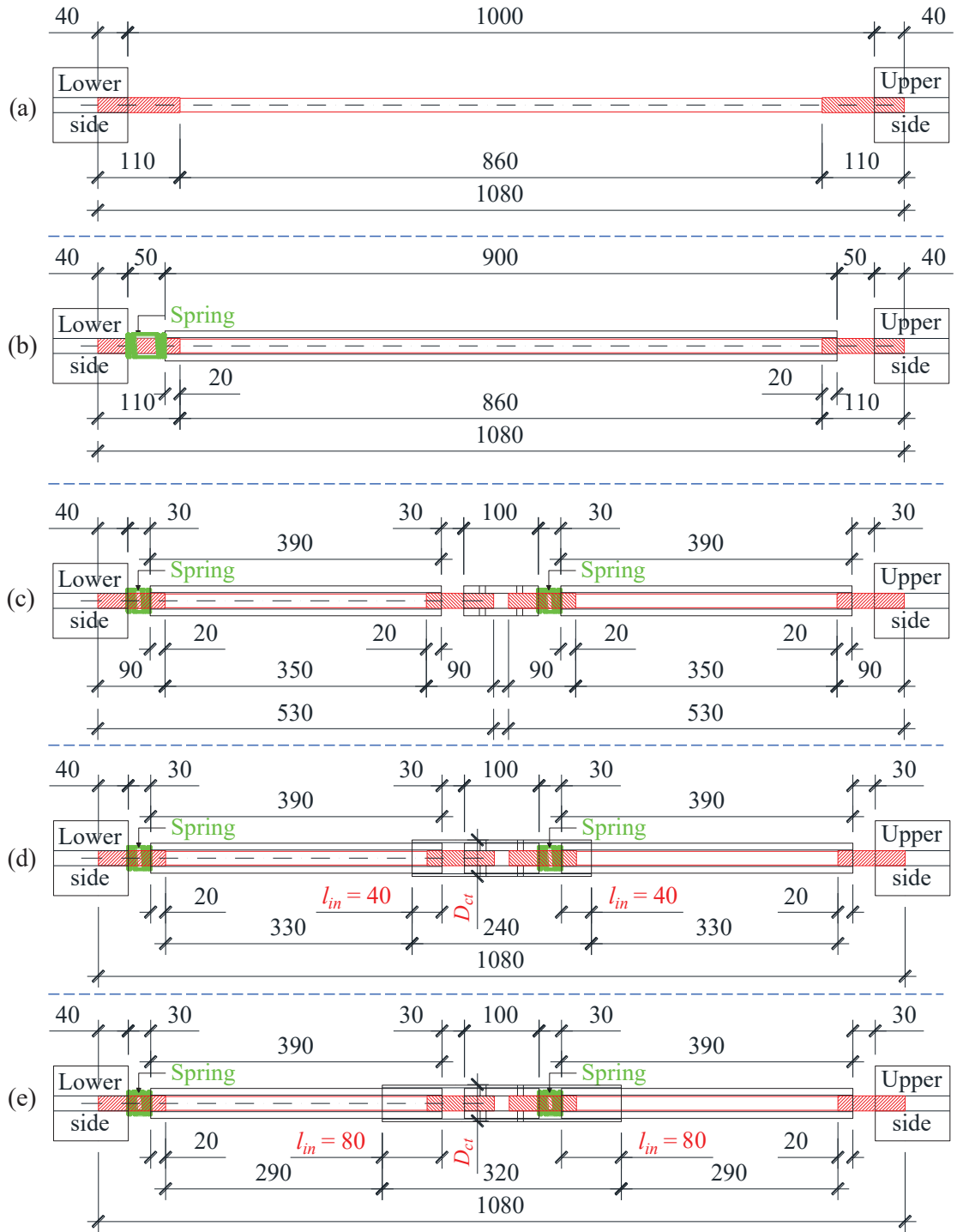


**Fig. 5.6.** Basic dimensions of the specimens for the compression loading tests.  
 (a) N-BR, (b) L-BR, (c) S-BR, (d) representative SCT specimens, and  
 (e) representative LCT specimens.

core bar (N-BR), long buckling restrainer base damper (L-BR), and four contraction allowance zones with no cover tube specimen (S-BR), as shown in Figs. 6(a),6(b), and 6(c), respectively. The reference specimens were identified based on the length of the buckling restrainer (N for none, S for short buckling restrainer, and L for long buckling restrainer). In contrast, Fig. 6(d) represents the proposed damper with the short cover tube specimens, while Fig. 6(e) represents the long cover tube specimens. For example, for SCT48-D, 48 indicates the outer diameter of the cover tubes,  $D_{ct} = 48$ .  $D$  indicates the insertion length,  $l_{in}$ , of the cover tube to the buckling restrainer. This compression loading test considered only two insertion lengths  $l_{in}$ :  $l_{in} = D_{br}$  and  $l_{in} = 2D_{br}$ .  $D_{br}$  is the diameter of the buckling restrainer. In addition, the material properties of the main damper components are listed in **Table 5**. The predicted core bar yield strength  $N_y$  and the Euler buckling load of the buckling restrainer that correspond to the L-BR specimen were obtained based on these data; the predicted values were  $N_y = 83$  kN and  $N_E^B = 230$  kN, respectively.

**Table 5** – Material properties of the compression loading test specimens

Steel grade	name	Yield stress (N/mm <sup>2</sup> )	Yield strain (microstrain)	Ultimate stress (N/mm <sup>2</sup> )	Elongation (%)
ABR400	M20 bar	322	1570	469	28
STKM 13A	Round tube 40 x 9	304	1483	458	59
STKM 13A	Round tube 54 x 6	367	1790	489	59
STKM 13A	Round tube 57 x 8	302	1473	451	58
STKM 13A	Round tube 48.6 x 3.5	393	1917	412	54

### 5.5.2 Core bar and contraction allowances

In the compression test, double-threaded structural anchor bolts M20 were used for the steel bar cores, in which the non-threaded section had a diameter of 18.2 mm (ABR product specifications and JIS B1220 standard). As mentioned in Section 5.4, the core bar threaded sections were inserted through the buckling restrainer at a distance of 20 mm and screwed through the end connector with a dimension of 40 mm for each specimen.

For the common BRBs, a stopper is often attached to the middle part of the steel core to keep the buckling restrainer's position by welding and widening the cross-sectional area. However, it is difficult for the steel core bar to mount the stopper in its middle because any processing such as welding and widening cannot be done. Thus, in this study, an ultra-high deflection coil spring with a size of SWY30-35 was selected as the stopper for the lower contraction allowance zones, where 30 and 35 indicate the outer diameter and the initial length of the spring, respectively. The allowable deflection of the spring was 22.8 mm. As shown in **Fig. 5.6**, a dimension of 30 mm was adopted in

each contraction allowance zone. As presented in **Fig. 5.6(c)**, when a 35 mm length spring is attached to the lower contraction allowances in each part of the steel bar core, the allowable deflection of the spring should ensure that the planned 30 mm gap is maintained owing to the gravity force of the buckling restrainer.

### 5.5.3 Buckling restrainer and cover tube

A round steel tube of  $40 \times 9$  mm having diameter  $D_{br} = 40$  mm and thickness  $t = 9$  mm was selected for the buckling restrainer in the base damper specimen L-BR. The same round steel tube section was then used for the other specimens except N-BR specimen. The clearances were estimated as  $c_s = 2$  mm and  $c_{sh} = 3.67$  mm. The safety factor of the base damper was  $SF = 1.65$ . The yielding moment capacity of the buckling restrainer was  $M_y^B = 1047$  kN  $\times$  mm. These values were calculated by equations used in the Section 3.2.3.

For the cover tube specimens, the section of the restrainers was the same as that of the base damper. By contrast, the size of the cover tubes was varied for comparison. Dimensions of  $48.6 \times 3.5$  mm,  $54 \times 6$  mm, and  $57 \times 8$  mm were utilized for the SCT and LCT specimens, as shown in **Table 5**, based on the  $R_{ct}$  assumptions in Section 5.4. In this compression test, three  $R_{ct}$  corresponding section modulus of the cover tubes were considered:  $R_{ct} = 0.9$ ,  $R_{ct} = 1.7$ , and  $R_{ct} = 2.3$ , as listed in **Table 6**. Two cover tube insertion lengths,  $l_{in}$ , were considered: 40 mm and 80 mm. Finally, the performances under compression loading tests were classified into three satisfactory scales: highly satisfactory, satisfactory (acceptable), and unsatisfactory, as shown in **Table 6** and discussed in Section 5.6.1.

**Table 6** – Section modulus of the tubes used in the compression tests

	L-BR	S-BR	SCT48-D	LCT48-2D	SCT54-D	LCT54-2D	SCT57-D	LCT57-2D
$Z_{br}/\text{mm}^3/$	5705	5705	5705	5705	5705	5705	5705	5705
$Z_{ct}/\text{mm}^3/$	-	-	5217	5217	9796	9796	13307	13307
$R_{ct}$	-	-	0.9	0.9	1.7	1.7	2.3	2.3
<b>Performances</b>	-	-	$\Delta$	$\Delta$	$\Delta$	$\odot$	$\odot$	$\odot$

$\odot$ ,  $\odot$ , and  $\Delta$  indicate highly satisfactory, satisfactory (acceptable), and unsatisfactory, respectively.

### 5.5.4 Testing setup and data measurement

To examine the behavior of the proposed BRKB damper, compression loading tests were performed using a UH-F1000 hydraulic universal test machine equipped with easy-to-see display measurement control, as shown in **Fig. 5.7**. The test specimens were placed vertically in the loading machine, and

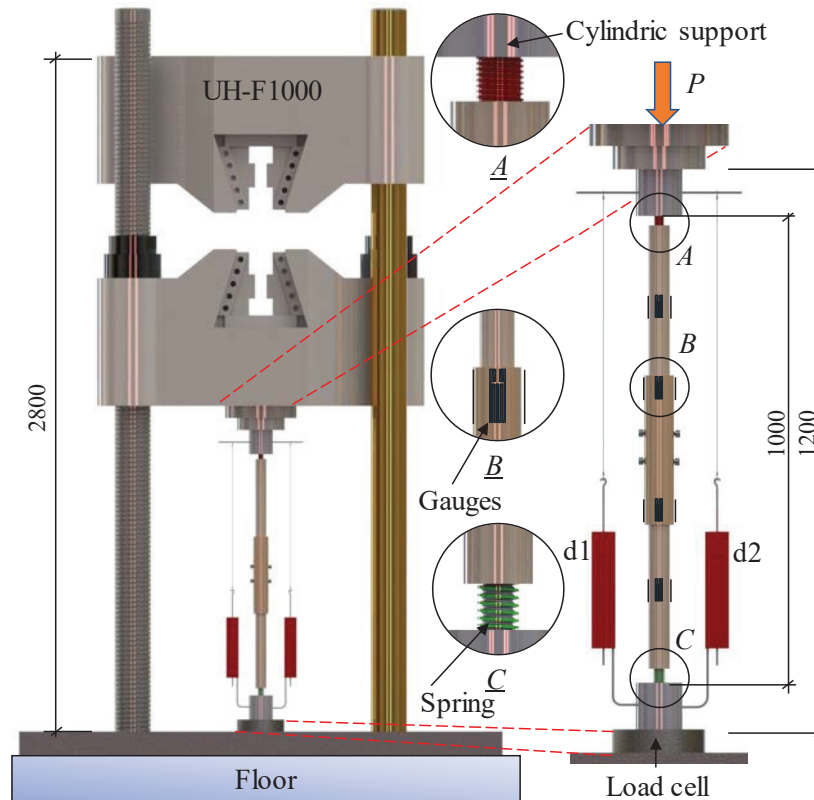


**Fig. 5.7.** Test setup and measuring system for the compression loading tests.

vertical load  $P$  was applied to the upper cylindrical connector. Cylindrical end supportors were utilized at each end of the damper in the compression loading test. In addition, a mobile loading cell was placed beneath the lower cylindrical end-supportor to measure the vertical load,  $P$ , as shown in **Fig. 5.7** (right side).

For the reference specimens, strains of the buckling restrainer tubes at position 1 of specimen L-BR, and positions 1 and 2 of specimen S-BR, are as shown in **Fig. 5.8(a)** and **Fig. 5.8(b)**, respectively. For the specimens with cover tubes, the strains of the cover tube edges were measured at gauge positions 2 and 3, and the strains of the restrainers were measured at gauge positions 1 and 4, as shown in **Fig. 5.8(c)**. **Fig. 5.8(d)** shows the strain gauge positions around the tube surface. In addition, displacement sensors  $d1$  and  $d2$ , as shown in **Fig. 5.7**, were utilized to measure the average vertical displacement of the specimens under loading conditions.

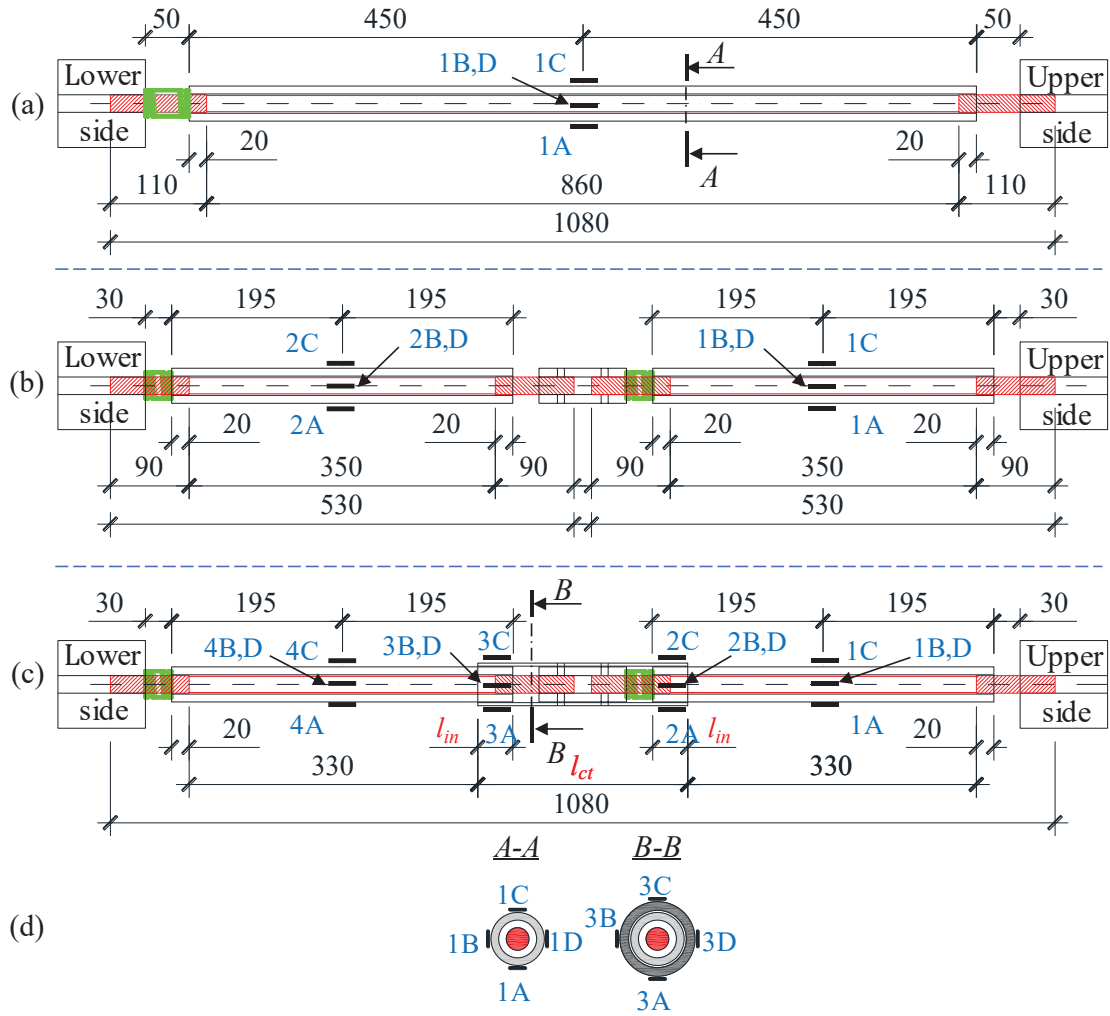


**Fig. 5.8.** Strain gauge locations.

- (a) L-BR, (b) S-BR, (c) representative SCT and LCT specimens, and  
 (d) Cross-sections of A and B.

## 5.6 Compression loading test results

### 5.6.1 Load-displacement relationship

**Fig. 5.9** presents the load–displacement relationships of all the test specimens subjected to compression loads. The notation  $P_y$  indicates the predicted yield load of the steel bar core. The primary horizontal axis indicates an applied compressive displacement,  $D$ , at each specimen. In contrast, the secondary horizontal axis presents the applied compressive displacement normalized by the yield displacement,  $D_y$ . The value of  $D_y$  for specimens N-BR and L-BR is 1.47 mm and reflected in **Fig. 5.9**, while for the specimens with four contraction allowance zones, the value of  $D_y$  is 1.32 mm and reflected in **Fig. 5.9(b)** and **Fig. 5.9(c)**.

In the case of the specimens in group 1, compared to the N-BR specimen (only bar), the highest increase in the maximum load of up to 111.5 kN was attained in the base damper specimen (L-BR) with a displacement of 38.6 mm, as shown in **Fig. 5.9(a)**. The N-BR and S-BR specimens showed a similar trend in the elastic stage. It can be seen that, if the proposed four contraction allowance zones BRKB have no cover tube, the failure mode is the same as that of the bar specimen at a load of 38 kN.

For the specimens in group 2, (**Fig. 5.9(b)**), the axial load capacities tended to increase slightly in SCT48-D with  $R_{ct} = 0.9$  and SCT54-D with  $R_{ct} = 1.7$ , the first two cover tube specimens, with maximum loads of 40 kN and 52 kN, respectively. However, these two specimens no longer resist any additional load owing to the failure of the cover tubes, as the photographs in Section 5.6.3. It is noted here that the SCT48-D and SCT54-D specimens, including N-BR and S-BR, buckled before yielding of the steel bar core. In addition, as the section modulus of the cover tube increased to  $R_{ct} = 2.3$  with a shorter insertion length  $l_{in}$ , the axial load capacity tended to increase after core bar yielding, as the results for specimen SCT57-D reveal. The maximum load that was attained was 111 kN.

For the specimens in group 3, (**Fig. 5.9(c)**), the load resistance capacity tended to increase as the insertion length of the cover tubes increased. In particular, specimen LCT57-2D possessed an axial load capacity that was more significant than those of the other two LCT specimens. The behavior of overstrength, as shown in **Fig. 5.9(c)**, will be assessed by cyclic loading tests and discussed regarding the brace compression-to-tension ratio in Section 5.8.1.

Overall, the following discussion can be summarized. When the  $R_{ct}$  was less than 1.0, the damper could not achieve the design purpose regardless of the cover tube insertion length. When the  $R_{ct}$  was 1.7, it was observed that the insertion length,  $l_{in}$ , was more influenceable for the load-bearing capacity of the proposed damper. For example, the specimen SCT54-D was unsatisfactory, while the specimen LCT54-2D was satisfactory. Moreover, when the  $R_{ct}$  was 2.3, the specimen SCT57-D was also

satisfactory. In contrast, the specimen LCT57-2D was highly satisfactory, in which a continuous strength increment was observed, as shown in **Fig. 5.9(c)**.

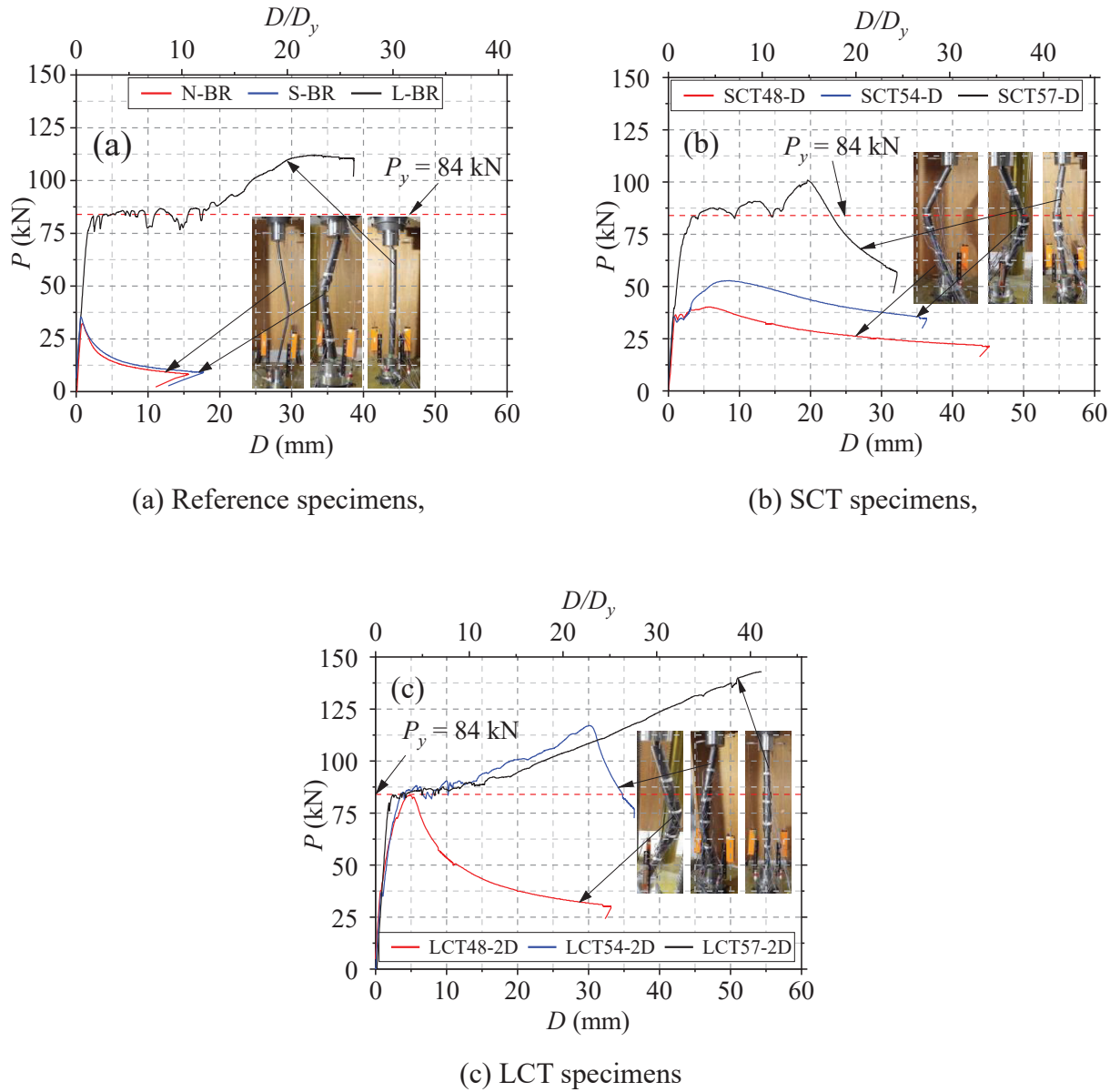


**Fig. 5.9.** Load–displacement relationship.

## 5.6.2 Variation in the strains for the cover tube and buckling restrainer

**Fig. 5.10** to **Fig. 5.16** show the relationship between the axial load and strain of the buckling restrainer and cover tubes for each specimen. The vertical dashed lines illustrate the yield strain corresponding to the buckling restrainer and cover tubes of the proposed damper. By employing large contraction allowances for specimen L-BR, the strain values of the buckling restrainer increased significantly, as shown in **Fig. 5.10(a)**. In the case of specimen S-BR, the strain values at the buckling restrainers and the maximum axial load were lower than those of the other all specimens, as shown in **Fig. 5.10(b)** and **Fig. 5.10(c)**.

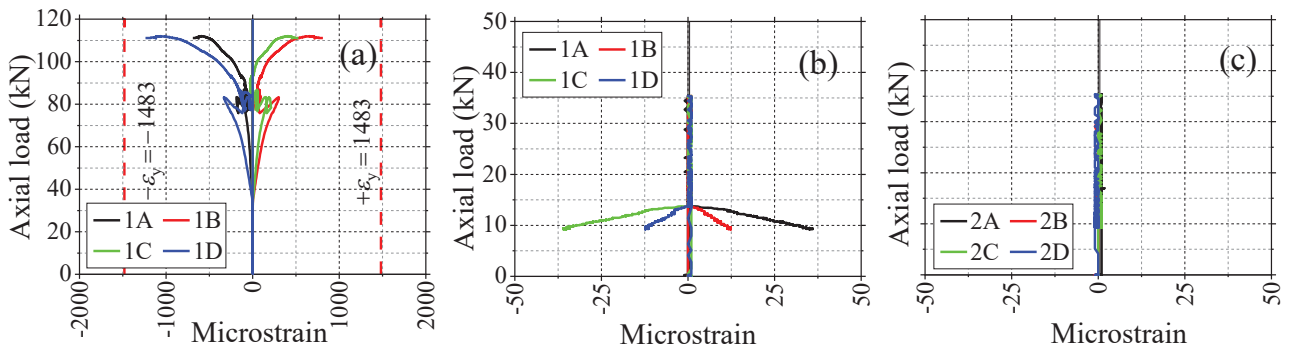


**Fig. 5.10.** Brace axial load and strain relations. (a) for L-BR and (b) and (c) for S-BR.

Overall, the test results reveal that the strain values at the buckling restrainers were lower than the yield strain for the specimens in all the groups under given loads, as shown in **Fig. 5.11(a)** and **Fig. 5.12(a)**, **Fig. 5.13(a)** and **Fig. 5.14(a)**, and **Fig. 5.15(a)** and **Fig. 5.16(a)**. However, the strain values in the cover tubes for the specimens in group 2 exceeded the yield strain regardless of the tube thickness corresponding to the given loads, as shown in **Fig. 5.11(b)**, **Fig. 5.13(b)**, and **Fig. 5.15(b)**. In contrast, the strain values at the cover tubes for the specimens in group 3, **Fig. 5.14(b)** and **Fig. 5.16(b)** were remained below the yield strain, except for specimen LCT48-2D, as shown in **Fig. 5.12(b)**. It is important to note that when the ratio of the section modulus, as defined with Eq. (5.1), is less than 1, for example,  $R_{ct}=0.9$ , the strain values of the cover tube were exceeded yield strain regardless of the cover tube length, as shown in **Fig. 5.11(b)** and **Fig. 5.12(b)**. In contrast, when the ratio  $R_{ct}$  increases to 1.7 for the specimen LCT54-2D, the strain values of the cover tube are attained to remain below the yield strain, as shown in **Fig. 5.13(b)**.

Furthermore, specimen LCT57-2D with a ratio of the section modulus of  $R_{ct} = 2.3$  achieved good performance, as shown in **Fig. 5.16(a)** and **Fig. 5.16(b)**, until the final loading stage. Finally, it was revealed that these two parameters,  $I_{in}$  and  $R_{ct}$ , possibly play essential roles in the design of our proposed BRKB.



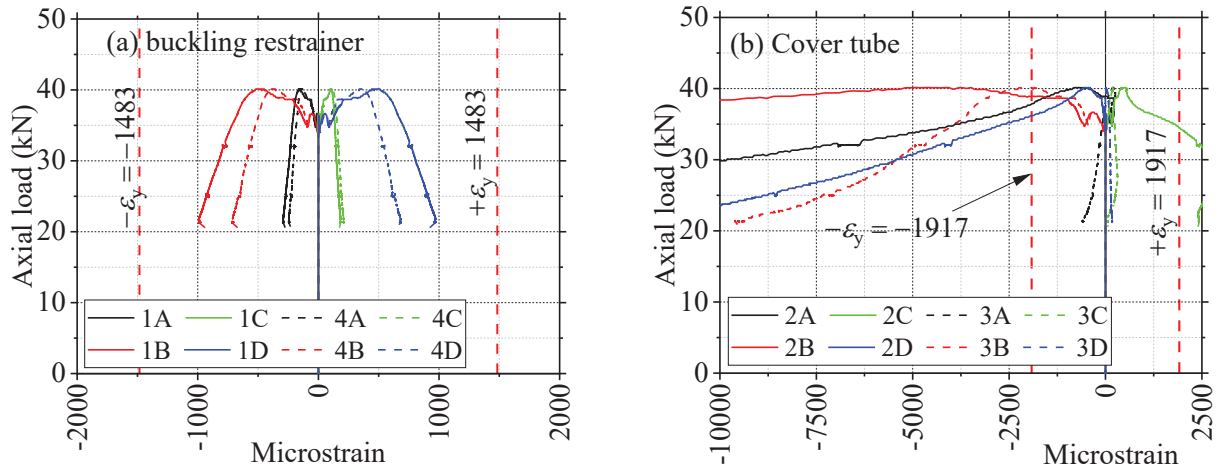


Fig. 5.11. Brace axial load and strain relations for SCT48-D.

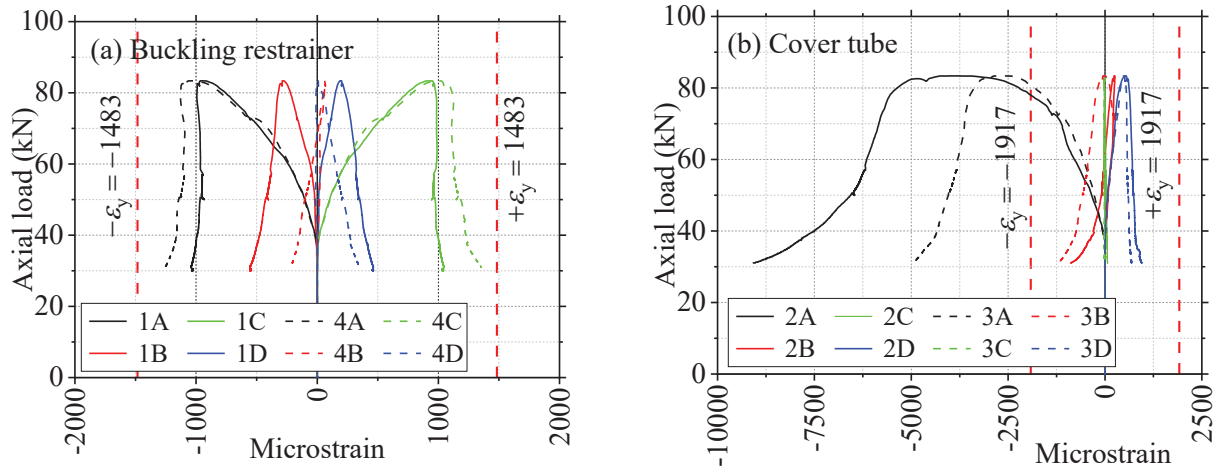


Fig. 5.12. Brace axial load and strain relations for LCT48-2D.

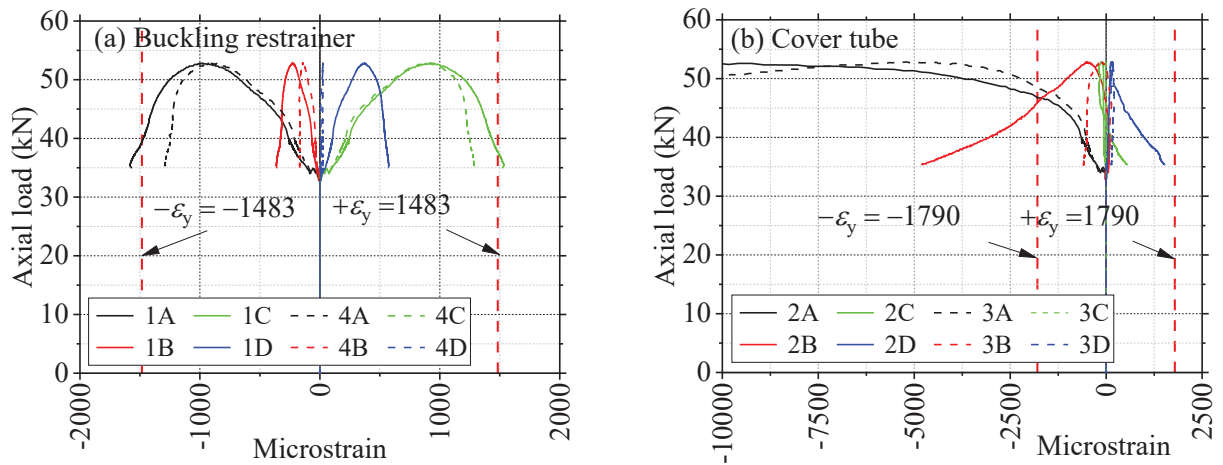


Fig. 5.13. Brace axial load and strain relations for SCT54-D.

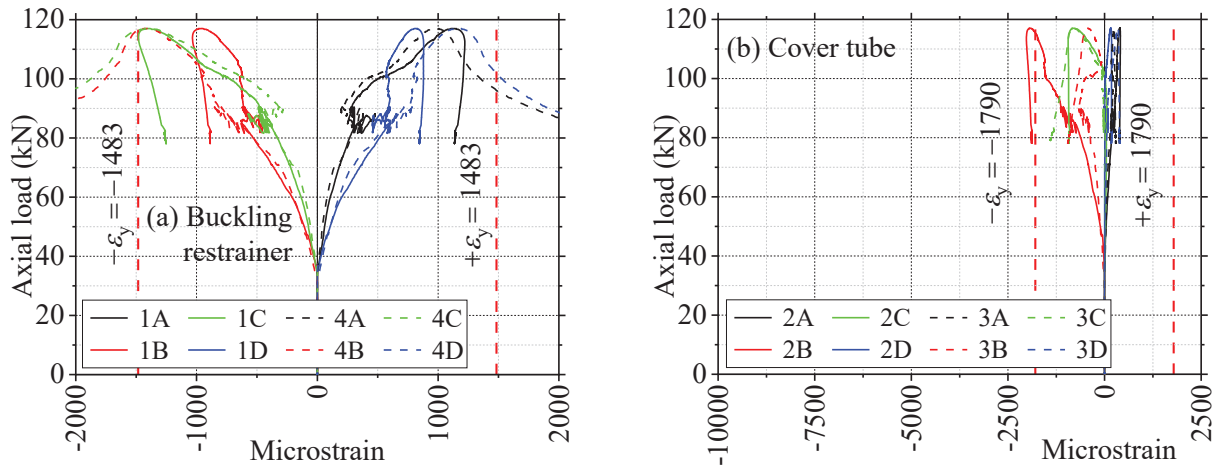


Fig. 5.14. Brace axial load and strain relations for LCT54-2D.

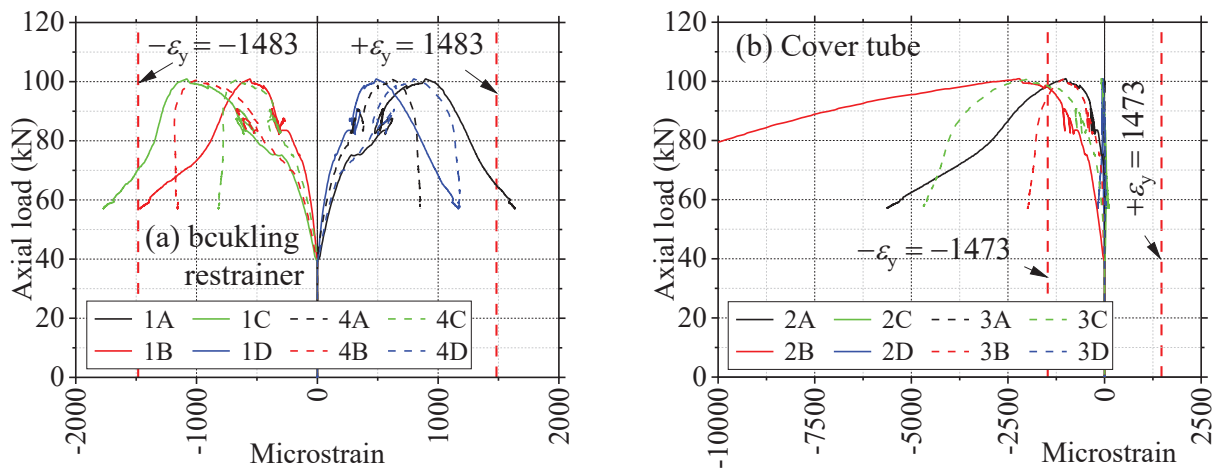


Fig. 5.15. Brace axial load and strain relations for SCT57-D.

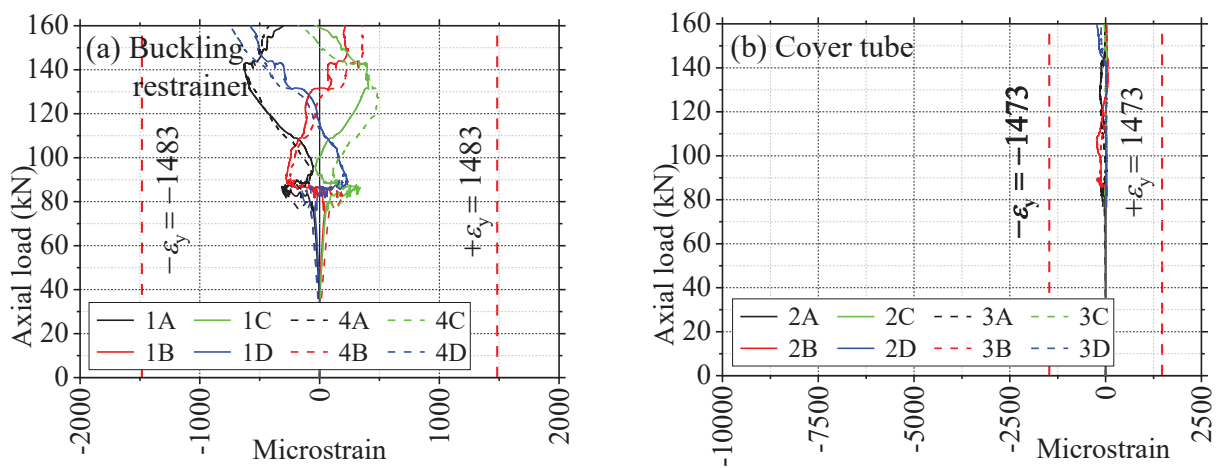
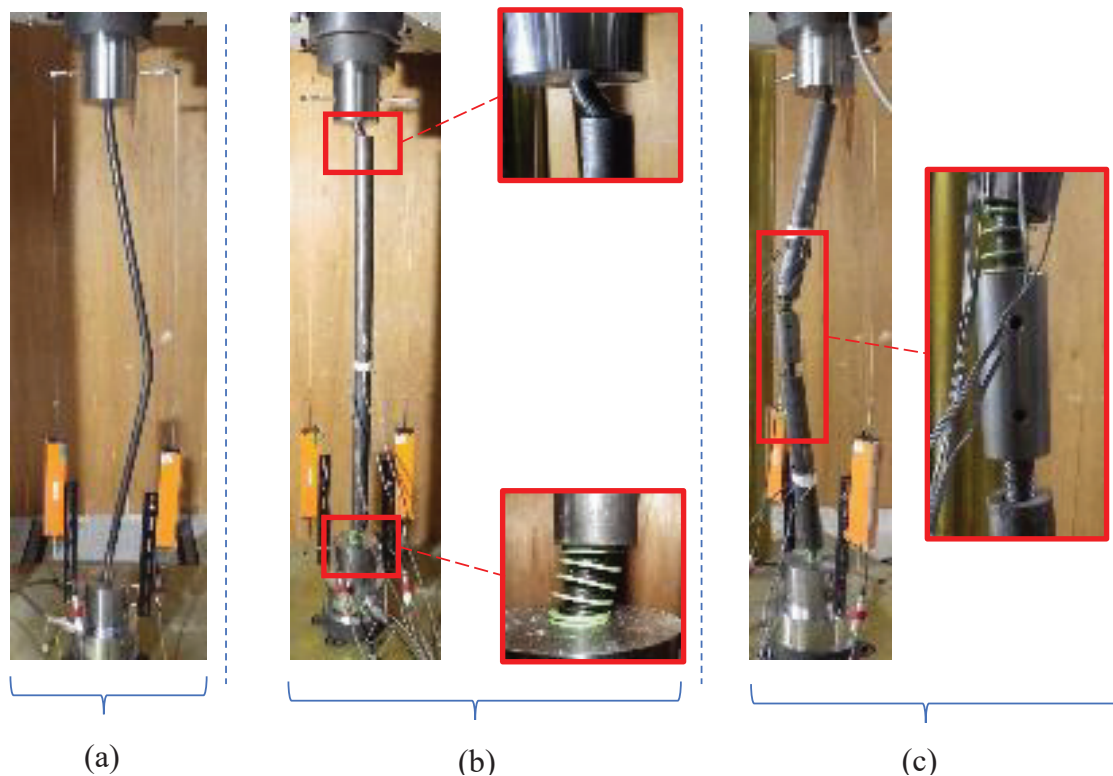


Fig. 5.16. Brace axial load and strain relations for LCT57-2D.

### 5.6.3 Residual deformation after compression loading

**Fig. 5.17** to **Fig. 5.19** illustrate the residual deformation for all the specimens in the final loading stages. **Fig. 5.17(a) – Fig. 5.17(c)**, **Fig. 5.18(a) – Fig. 5.18(c)**, and **Fig. 5.19(a) – Fig. 5.19(c)** represent the deformations of the specimens in groups 1, 2, and 3, respectively.



**Fig. 5.17.** Residual deformation in the final stage of loading for the reference specimens.

(a) N-BR, (b) L-BR, and (c) S-BR

For specimen L-BR, slight bending was observed in the middle of the buckling restrainer owing to the axial force acting on the steel bar core being transferred to the BR prior to the core bar yielding, as shown in **Fig. 5.17(b)**. When the compressive load was increasingly applied to the steel bar core, it induced a plastic hinge at the exposed portion of the steel bar core in the upper contraction allowance after the core bar yielded. The maximum axial load was  $N_{max} = 111$  kN. Moreover, it can be seen from specimen S-BR that, when the proposed damper had no cover tube, plastic hinges quickly occurred in the steel bar core, as shown in **Fig. 5.17(c)**. The maximum load, which leads to core bar buckling in the earlier stage of the applied loading, was only  $N_{max} = 30$  kN. The flexural buckling of the steel bar core on its exposed portion caused an excessive lateral deflection in specimen S-BR.

Furthermore, to improve the stability of the proposed damper, a cover tube insertion length of  $l_{in} = 40$  mm was employed for the specimens in Group 2. In the first two specimens, specimens SCT48-D

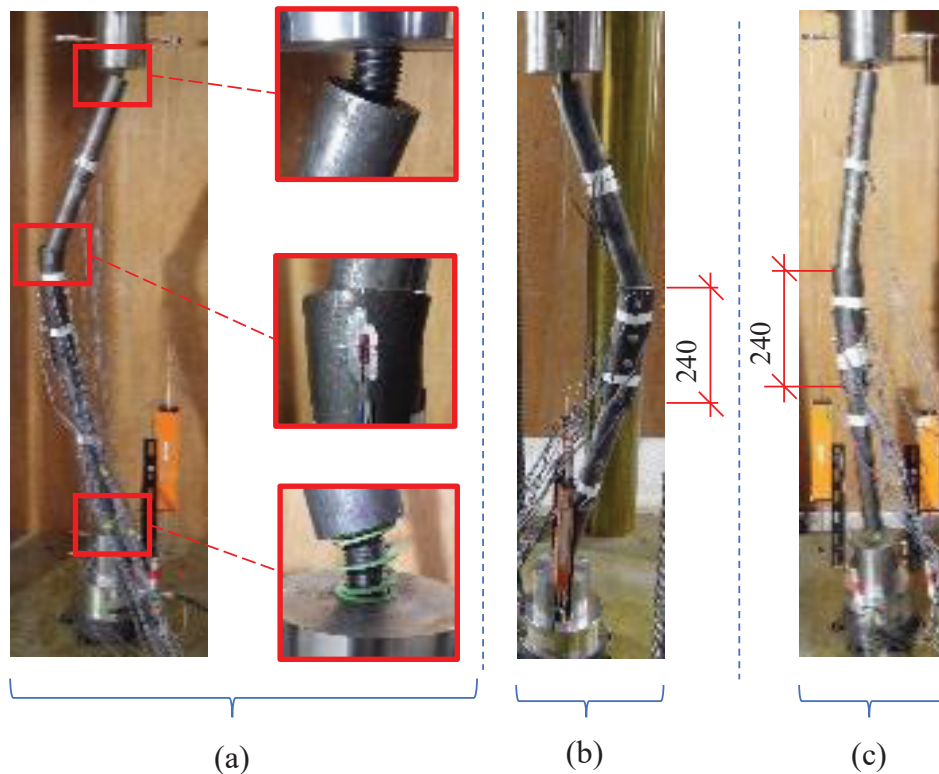


**Fig. 5.18.** Residual deformation in the final stage of loading for the SCT specimens.

(a) SCT48-D, (b) SCT54-D, and (c) SCT57-D

and SCT54-D, with  $R_{ct} = 0.9$  and  $1.7$ , respectively, an excessive distortion was formed at the edge of the cover tube because of its insufficient insertion length as shown in **Fig. 5.18(a)** and **Fig. 5.18(b)**. These local failure behaviors were caused by a maximum axial load equal to  $N_{max} = 40$  kN. In specimen SCT57-D with an  $R_{ct} = 2.3$ , the edge failure of the cover tube was visibly small. In contrast, the buckling restrainer was slightly deformed near the upper edge of the cover tube under the given loads, as shown in **Fig. 5.18(c)**. The maximum axial load was measured at  $N_{max} = 100$  kN.

Although the insertion length of the cover tube increased to  $l_{in} = 80$  mm for specimen LCT48-2D, global buckling occurred owing to the specimen's small  $R_{ct}$  of  $0.9$ . Plasticity initiation was slightly delayed with  $N_{max} = 80$  kN compared with specimen SCT48-D. It is noted here that the small thickness of the cover tube could not sustain the normal force acting on it from the buckling restrainer, as shown in **Fig. 5.19(a)**. Moreover, plasticity patterns, similar to those of specimen LCT48-2D, were observed in specimen LCT54-2D (**Fig. 5.19(b)**). The maximum axial load was  $N_{max} = 117$  kN.

Finally, as a result of the compression loading tests, a specimen with sufficient strength and a very stable BRKB was obtained, which was specimen LCT57-2D. No significant failure was observed in this specimen except for the shortening of the steel core without failure of the buckling restrainer and

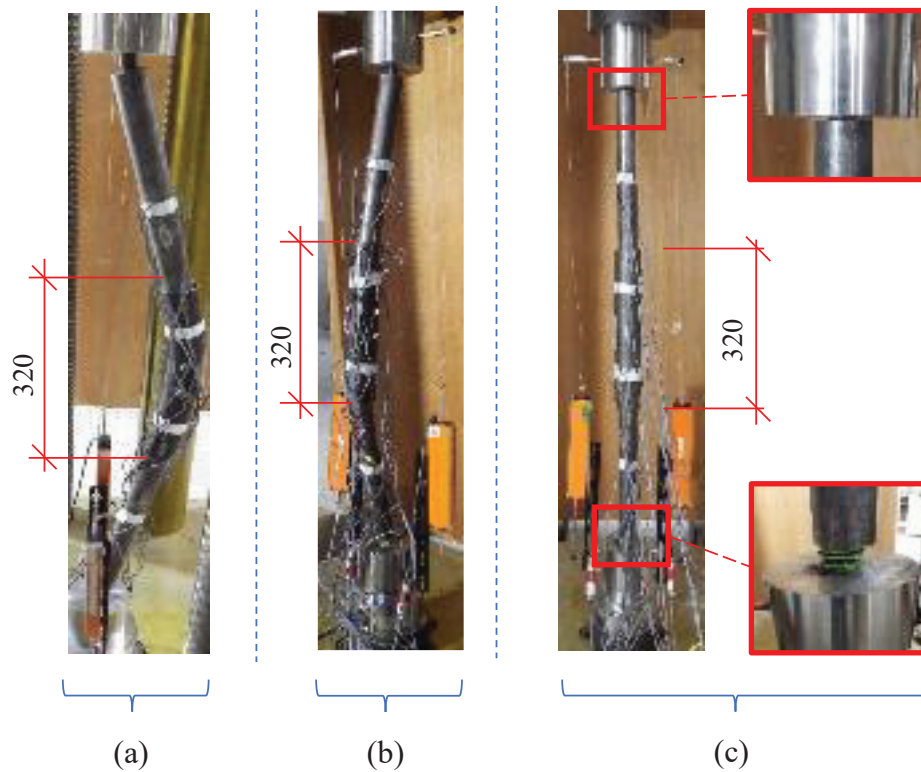


**Fig. 5.19.** Residual deformation in the final stage of loading for the LCT specimens.  
 (a) LCT48-2D, (b) LCT54-2D, and (c) LCT57-2D.

cover tube, as shown in **Fig. 5.19(c)**. In addition, the compression loading tests revealed that the number of contraction allowances strongly influenced the load-bearing capacities of the proposed dampers under given axial loads. Nevertheless, extended cyclic loading tests were conducted on different parameters of the cover tube BRKBs to examine the cyclic response of the proposed dampers.

## 5.7 Cyclic loading tests

### 5.7.1 Test specimen

The compression loading tests revealed that the dampers LCT54-2D and SCT57-D with cover tubes with  $R_{ct}$  of 1.7 and 2.3, respectively, exhibited satisfactory design performance. In contrast, LCT57-2D with  $R_{ct}$  of 2.3 exhibited highly satisfactory. Considering the compatibility of the cross-sections between the buckling restrainer and cover tube, the effect of the cover-tube insertion lengths was examined for a fixed  $R_{ct}$  value, which was 1.4 in the cyclic loading test specimens, as listed later in **Table 9**. Three dampers, SCT60-D, LCT60-2D, and LCT60-3D, were prepared and tested to investigate their cyclic responses. **Fig. 5.20** presents the basic dimensions of the three dampers

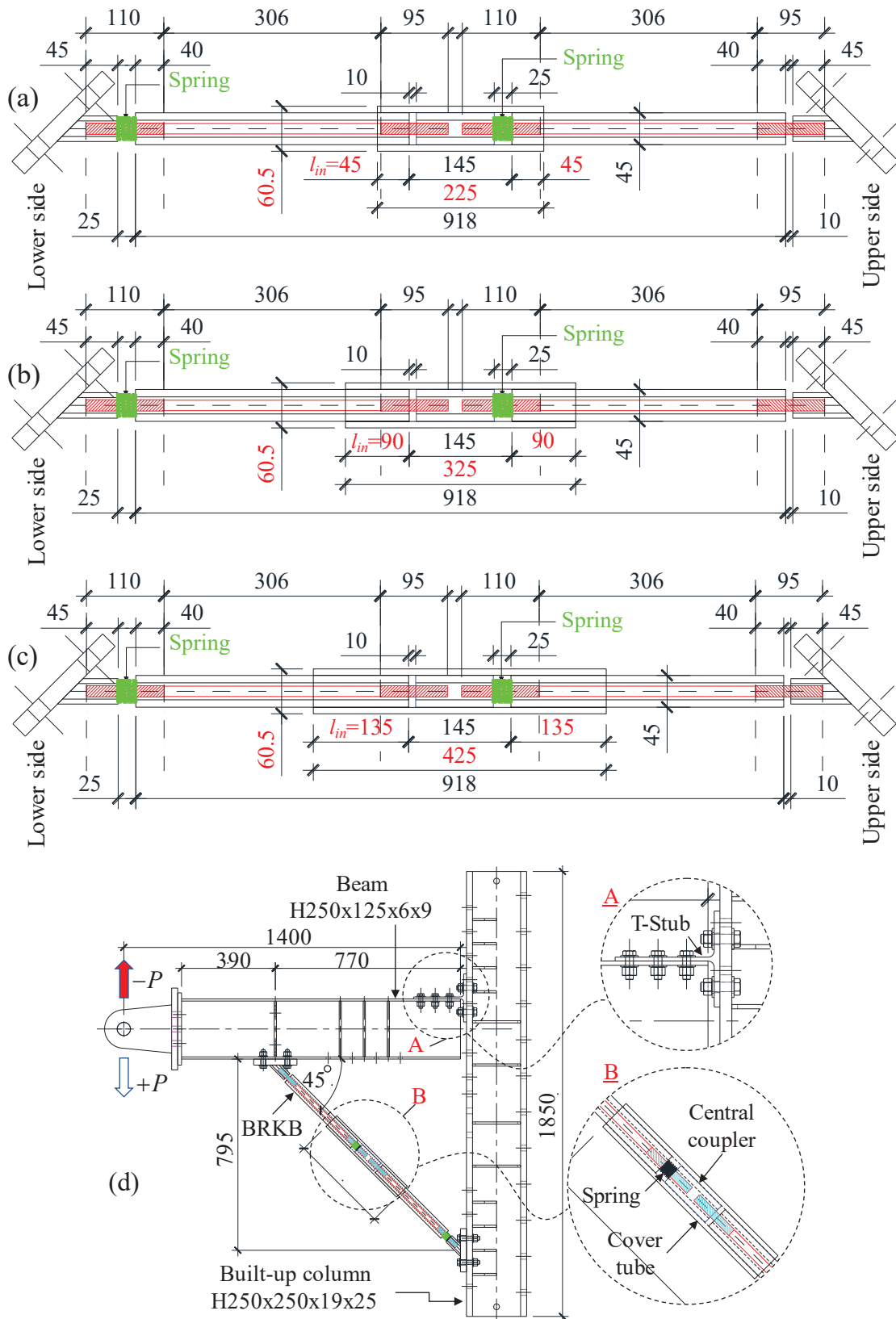


Fig. 5.20. Basic dimensions of the dampers for the cyclic loading test specimens.

(a) SCT60-D, (b) LCT60-2D, (c) LCT60-3D, and (d) sub-assembly.

and the sub-assembly of the cyclic loading tests. As previously mentioned, cover tube insertion lengths  $l_{in}$  of 45, 90, and 135 mm were selected as the experimental study test parameters, as shown in **Fig. 5.20(a)** to **Fig. 5.20(c)**. As noted here, these values imply that  $l_{in} = D_{br}, 2D_{br},$  and  $3D_{br}$  for each damper.

The geometric characteristics and material properties of the dampers are listed in **Table 7** and **Table 8**, respectively. Their identifications were the same as those used in the compression loading tests. A round steel tube of  $45 \times 10$  mm was used for the buckling restrainers, while that of  $60.5 \times 7$  mm was used for the cover tubes. **Table 9** presents the section modulus of tubes.

**Table 7** – Geometrical parameters of the proposed dampers used in the cyclic loading tests

	Name	Cont. allow.	Core bar			Buckling Restrainer tube			Cover tube				
			Quantity	Screw diameter, $d_s$ (mm)	Screw length, $l_r$ (mm)	Core length, $l$ (mm)	Outer diameter, $D_{br}$ (mm)	Thickness, $t$ (mm)	Length, $l_{br}$ (mm)	Outer diameter, $D_{ct}$ (mm)	Thickness, $t_{ct}$ (mm)	Inner diameter, $d_{ct}$ (mm)	Length, $l_{ct}$ (mm)
			ABR			STKM13A			STKM13A				
<b>1</b>	SCT60-D	4	M22	95,110	511	45	10	386	60.5	7	46.5	235	45
<b>2</b>	LCT60-2D	4	M22	95,110	511	45	10	386	60.5	7	46.5	325	90
<b>3</b>	LCT60-3D	4	M22	95,110	511	45	10	386	60.5	7	46.5	415	135

Abbreviations. ABR: Specifications of structural double-threaded anchor bolts. STKMA: Steel grade for structural steel tubes.

**Table 8** – Material properties of the cyclic loading test specimens

Steel grade	name	Yield stress (N/mm <sup>2</sup> )	Yield strain (microstrain)	Ultimate stress (N/mm <sup>2</sup> )	Elongation (%)
ABR400	M22 bar	302	1473	453	29
STKM 13A	Round tube 45 x 10	283	1380	442	61
STKM 13A	Round tube 60.5 x 7	283	1380	435	68

**Table 9** – Section modulus of the tubes used in the cyclic loading tests

	SCT60-D	LCT60-2D	LCT60-3D
$Z_{br}/\text{mm}^3/$	8090	8090	8090
$Z_{ct}/\text{mm}^3/$	5705	5705	5705
$R_{ct}$	1.4	1.4	1.4
<b>Performances</b>	$\Delta$	$\odot$	$\ominus$

$\ominus$ ,  $\odot$ , and  $\Delta$  indicate highly satisfactory, satisfactory (acceptable), and unsatisfactory, respectively.

The steel-core-bar configuration based on the fabrication standards JIS B 1220 is the same as that described in Section 5.5.2. However, the diameters of the core bar were 22 mm and 20.2 mm at the thread and shank parts, respectively. The insertion length of the core bar threaded parts into the restrainer was 40 mm. The core bar was screwed through the end connector with 45 mm. Under these conditions, the shank part should not be exposed if the rotation angle of the beam reaches 0.02 radian. Four contraction allowance zones with a total distance of 70 mm were employed for all the dampers. The lower contraction allowance zones with the coil spring are marked green for each damper. In addition, the safety factor, SF, of the buckling restrainer was calculated, implying the theory introduced in the previous Section 3.2.3. According to the calculation, the safety factor was SF = 2. **Fig. 5.20(d)** illustrates the sub-assembly used for the cyclic loading test. In order to observe the cyclic behavior of the proposed damper, a strong column and a sufficient strength beam were selected in the sub-assembly. A 1.4 m beam of the hot-rolled H-section with dimensions of H-250 × 125 × 6 × 9 and a built-up section column with dimensions of H-250 × 250 × 19 × 25 were utilized. The length of each member was taken based on the damper length in this study. In addition, the performances of specimens under cyclic loading tests were also classified into three satisfactory scales: highly satisfactory, satisfactory (acceptable), and unsatisfactory, as shown in **Table 9** and discussed in Section 5.8.3.

### 5.7.2 Testing setup

**Fig. 5.21** illustrates the design of the general apparatus used for the cyclic loading tests. The out-of-plane displacements are entirely constrained, as shown in **Fig. 5.21(a)**. Four rollers attached to the beam ensure that the beam moves freely over the surface of the vertical constrainer without any direct beam-to-constrainer interaction. The sub-assembly that includes a beam, column, and the proposed BRKB is attached to the reaction frame fully fixed and loaded by a vertical jack at the beam tip. As illustrated in **Fig. 5.21(b)** and **Fig. 5.21(c)**, a beam-to-column weld-free connection (pin connection) was adopted to reveal the energy dissipation capacity of the proposed damper. In this regard, the shape of the T-stub element was used for the connection, as shown in **Fig. 5.21(c)**. Thus, the beam and column behaviors can be regarded as entirely elastic. An assembled BRKB was connected by the right



and left screw connector to the beam and column of the specimen at a 45° inclination, as shown in **Fig. 5.21(b)**. In addition, **Fig. 5.22** shows photographs of the actual test setup.

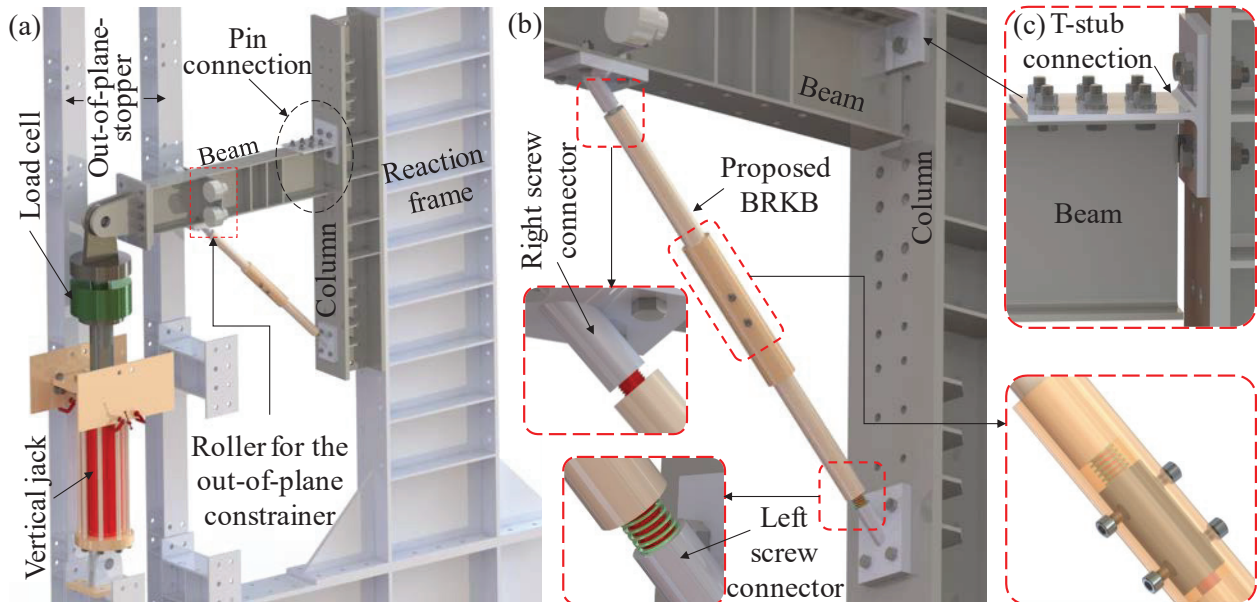


**Fig. 5.21.** General apparatus for the cyclic loading test. (a) Test setup configuration, (b) view of the BRKB placement, and (c) detailed view of the weld-free connection.

### 5.7.3 Data measurement of testing

**Fig. 5.23** presents the cyclic loading tests program. A hydraulic jack with a stroke of 500 mm and a maximum force of 1000 kN was applied at the beam tip. The downward direction of vertical load  $P$  was assigned a positive sign, as shown in **Fig. 5.23(a)**. The following data were measured: (1) vertical displacement of the beam tip,  $\delta$ , regarding vertical load,  $P$ , (2) rotation of the beam relative to the beam-to-column pin connection, and (3) strains of the buckling restrainer and cover tube for each specimen. Sixteen strain gauges were mounted at each specimen to record its strain behavior, as shown in **Fig. 5.23(d)**.

Displacement sensors d1 and d2 to d5 were utilized to measure the vertical displacement of the beam tip and the rotation of the beam, respectively. Finally, displacement sensors d6 and d7 were placed along the axis of the BRKBs to measure the elongation of the steel bar cores.

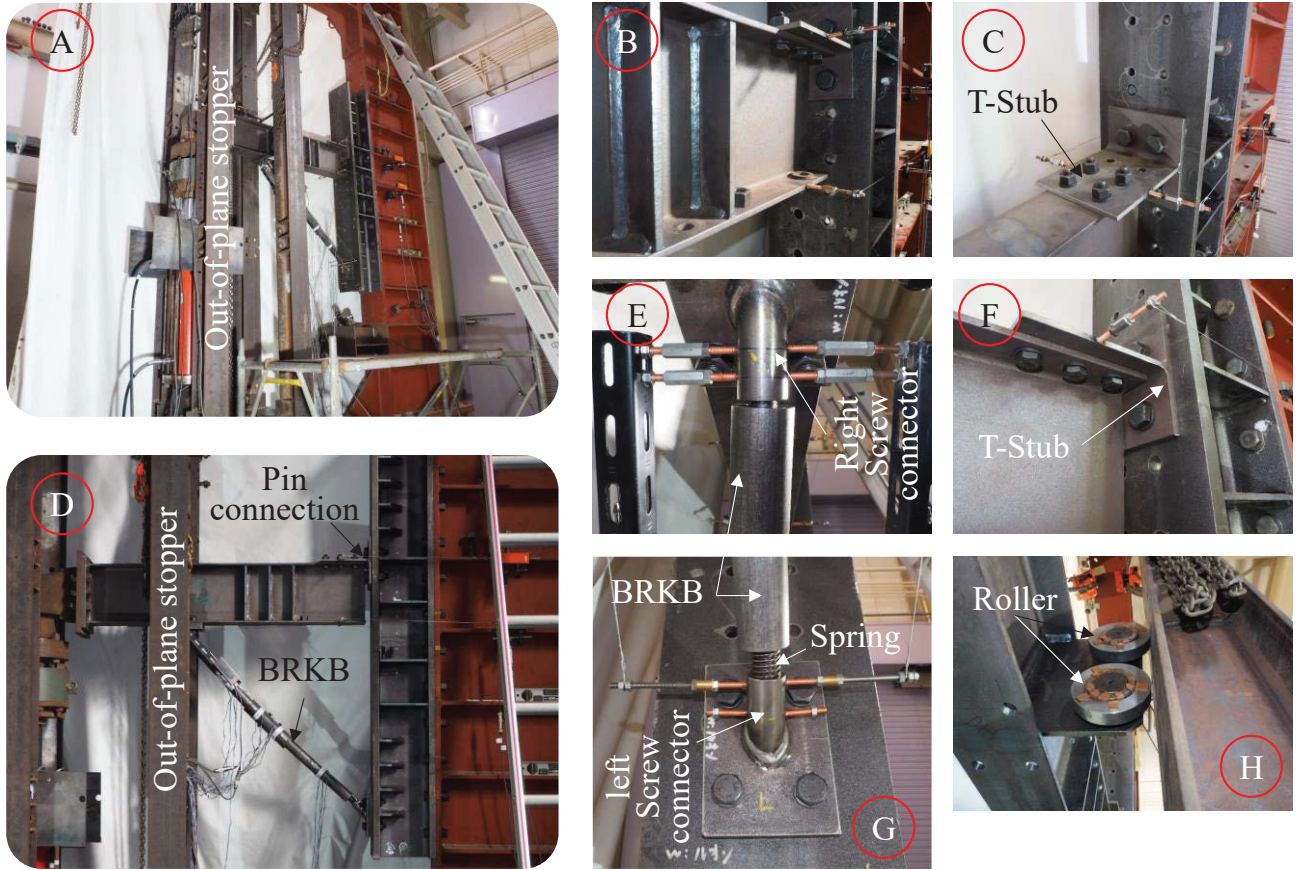
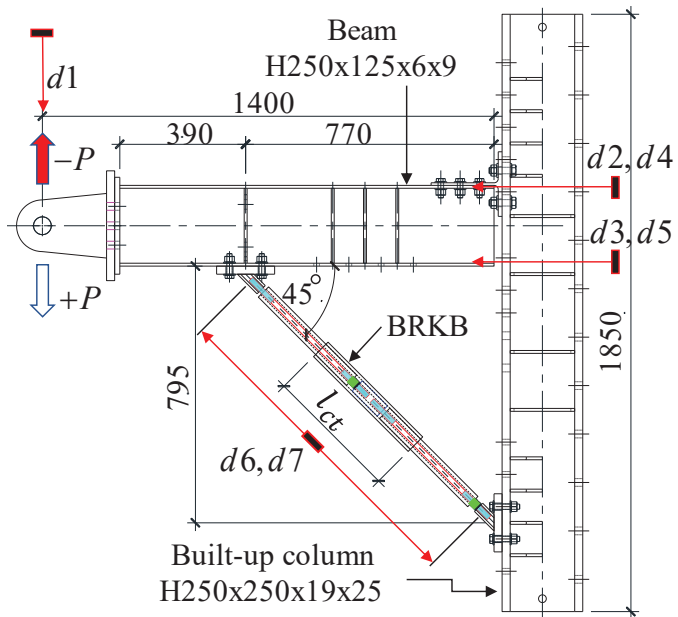
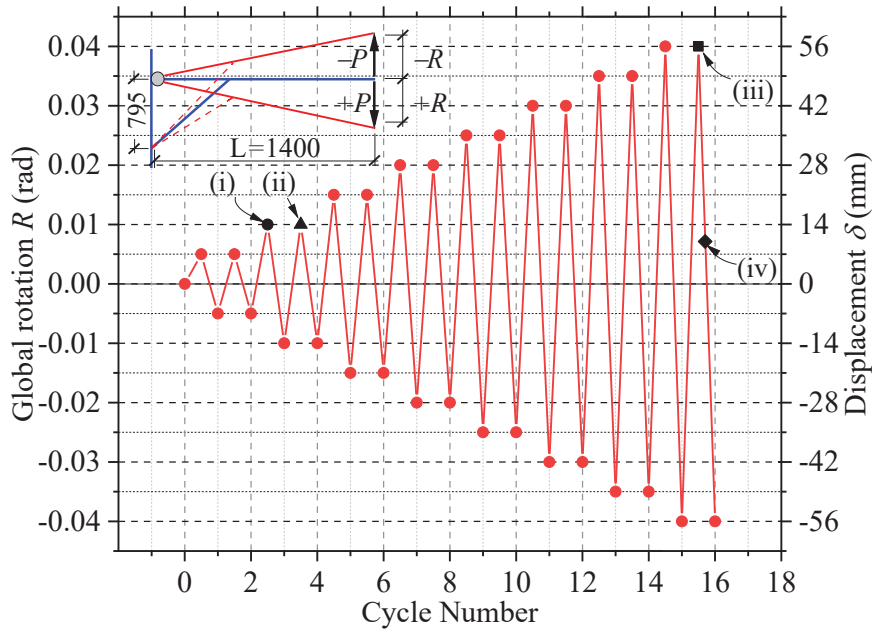


Fig. 5.22. Photographs of the cyclic loading test setup

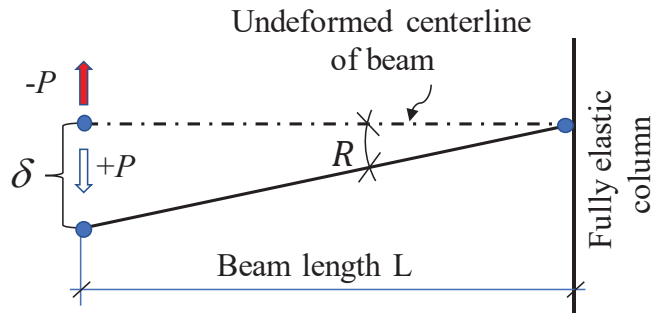


(a) displacement measurements plan

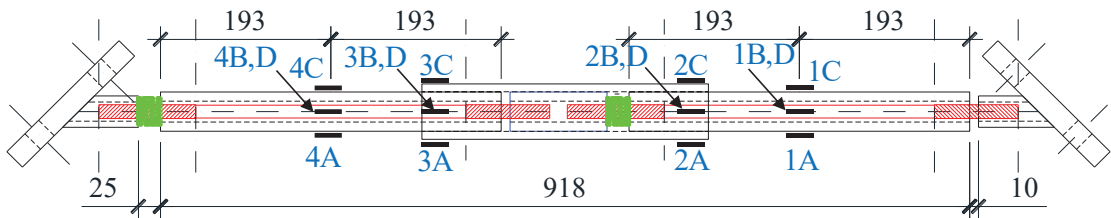
Fig. 5.23. Cyclic loading tests program.



(b) loading protocol,



(c) global rotation of the reference beam,



(d) gauge positions on the dampers.

**Fig. 5.23** Cyclic loading tests program (continued).

#### 5.7.4 Global rotation angles and loading conditions

Displacement-controlled cyclic loading was used in the test. **Fig. 5.23(c)** shows the global rotation of the reference beam. As shown in **Fig. 5.23(c)**, the global rotation angle of the test specimen was determined based on a pure cantilever beam ( $R = \delta/L$ ).

The loading protocol is shown in **Fig. 5.23(b)**. The right vertical axis represents the beam tip displacement imposed on the controlled global rotation angle, and the left vertical axis illustrates the global rotation angle. In the cyclic loading test, the initial displacement was calculated as  $\delta = 7$  mm corresponding to  $R(\text{rad}) = 0.5\%$ . The loading was increased up to  $R(\text{rad}) = 4\%$  in increments of  $R(\text{rad}) = 0.5\%$ . Each increment consisted of two cyclic loading steps. The beam and column were considered fully elastic to observe the cyclic response of the proposed damper, as shown in the test setup design. After each loading cycle, the loading was stopped, and a visual inspection of the specimen, including dampers, was performed.

### 5.8 Cyclic loading test results

#### 5.8.1 Load and global rotation angle relationship

This section discusses the effect of the test parameters on the cyclic responses of the three dampers, and the results are illustrated in **Fig. 5.24**. The horizontal dashed lines marked as  $P_y$  in each graph indicate the predicted yielding load of the steel bar core.

The specimen with damper SCT60-D achieved a global rotation of  $R(\text{rad}) = \pm 3\%$ , which is 75% of the  $R(\text{rad}) = \pm 4\%$  expected for the test specimens. Following the  $R(\text{rad}) = \pm 0.5\%$  increment, which consisted of two loading steps, the BRKB remained in the elastic range. At this stage, no yielding was apparent for each member of the dampers, such as the buckling restrainers and cover tubes. Significant strength deterioration was initiated in the specimen with the SCT60-D damper at a global rotation of  $R(\text{rad}) = +1\%$  (point (i)) after the cover tube edge failed in the second cycle of  $R(\text{rad}) = +1\%$  (point (ii)). The failure continuously occurred upon the further increase in the global rotation, as shown in **Fig. 5.24(a)**. The maximum load at points (i) and (ii) was 50 kN on the brace compression side and slightly over 50 kN on the brace tension side.

The specimen with the LCT60-2D damper achieved a global rotation  $R(\text{rad}) = \pm 4\%$ . However, in the second cycle  $R(\text{rad}) = +4\%$ , a sudden strength degradation occurred because of the buckling of the bottom restrainer tube, as shown in **Fig. 5.24(b)** (point (iii)). At this stage, the maximum brace compressive load reached 124 kN. In contrast, the maximum tensile load reached 80 kN.

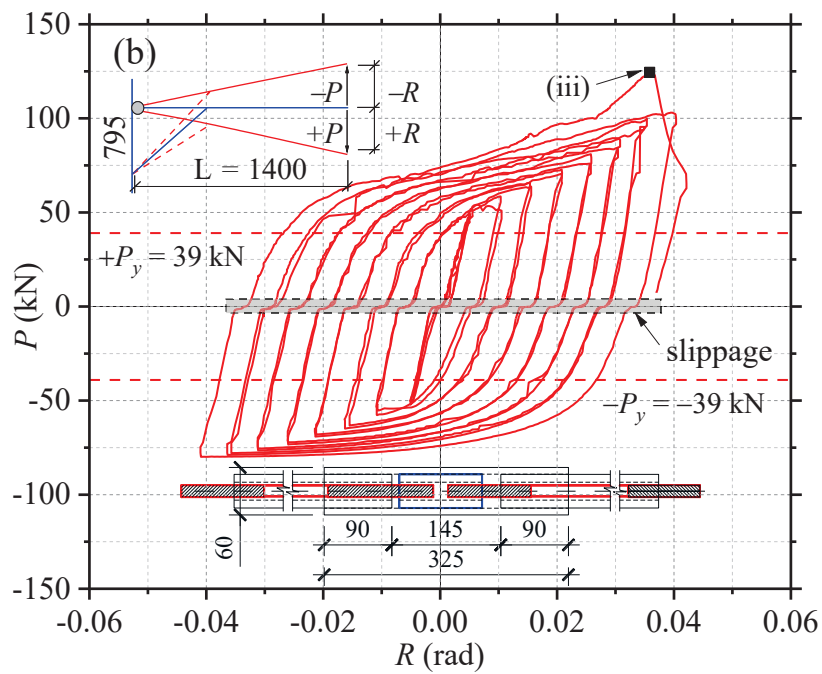
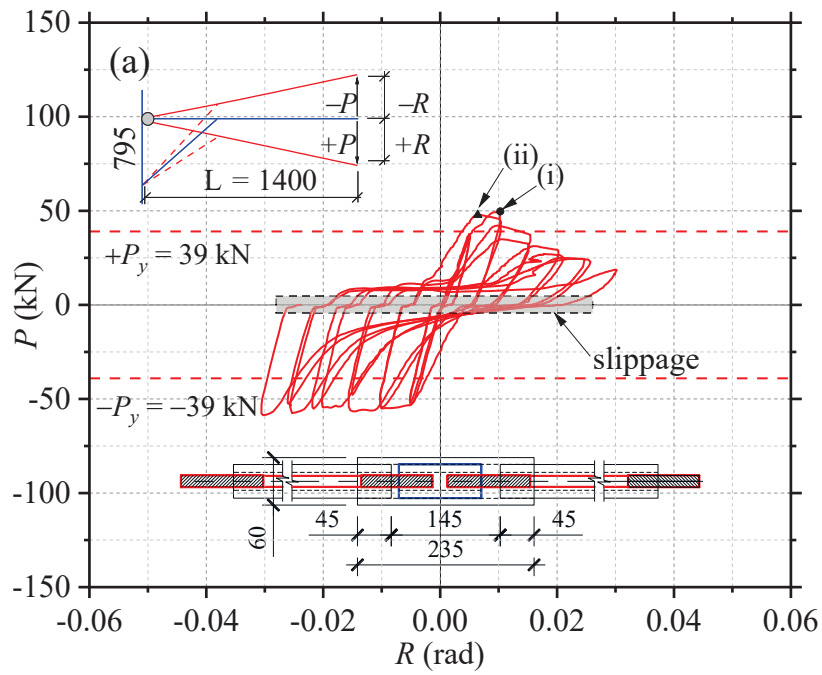
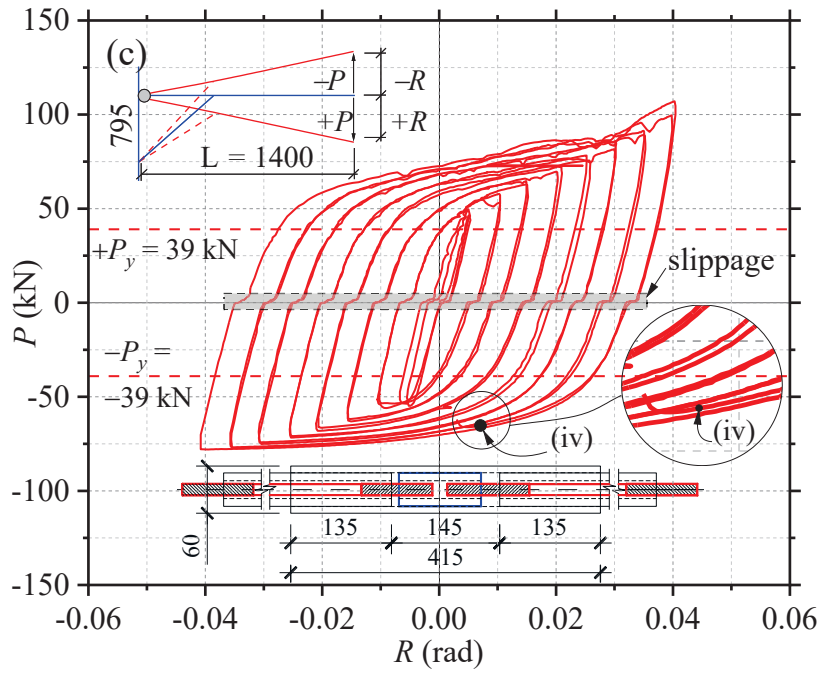
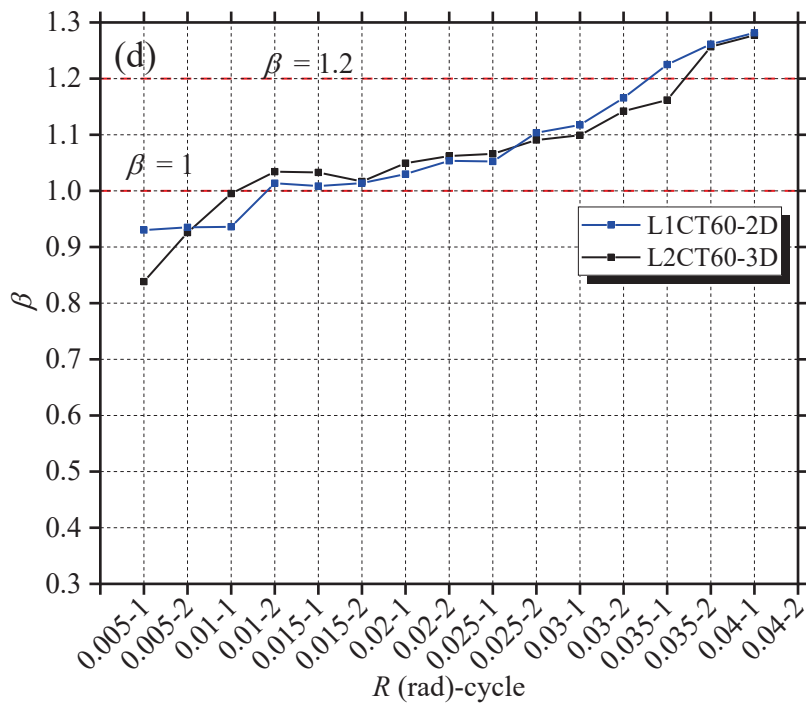


Fig. 5.24. Vertical load and story drift angle relations for three specimens during the cyclic loading tests.



(c) LCT60-3D



(d) compression-to-tension ratio

**Fig. 5.24.** Vertical load and story drift angle relations for three specimens during the cyclic loading tests (continued).

Finally, the specimen with the LCT60-3D damper exhibited sufficient ductile behavior until the steel bar core reached the rupture point corresponding to the second cycle  $R(\text{rad}) = +4\%$ , as shown in **Fig. 5.24(c)** (point (iv)). At this stage, the maximum load  $P$  reached 106 kN. In contrast, the maximum load,  $P$ , corresponding to the tensile side of the brace, reached 78 kN. In addition, the observed maximum load that led to bracing in the compression state of the specimen with the LCT60-2D damper was slightly larger than that of the specimen with the LCT60-3D damper.

For the proposed BRKBs, it was observed that the insertion length of the cover tube plays an essential role in its cyclic loading responses. For example, when  $l_{in} = D_{br} = 45$  mm (SCT60-D), the damper could not dissipate energy well, whereas the other two dampers could. In addition, slight slippage was observed during the cyclic loading tests for each result. It is likely that jack-to-beam or brace-to-beam connection bolts were affected for the above reason because of their rigidity.

**Fig. 5.24(d)** presents the variation in the brace compression-to-tension ratio [40], [43], defined as the ratio of the maximal compressive force to the maximal tensile force for each cycle. In Japan, the BCJ specification [38] permits  $\beta \leq 1.2$ , while the US standard AISC 341 [40] permits  $\beta \leq 1.3 - 1.5$ . The results of this study are based on the BCJ specifications. It can be observed that the specimen with the SCT60-D damper could not meet these criteria. Therefore, its results were neglected in this study. Specimen with the LCT60-2D damper met these criteria between global rotations  $R(\text{rad}) = 0.01 - 2$  and  $R(\text{rad}) = 0.03 - 2$ , while specimen with the LCT60-3D damper met these criteria between  $R(\text{rad}) = 0.01 - 1$  and  $R(\text{rad}) = 0.035 - 1$ . Finally, it is concluded that the specimen with the LCT60-3D damper exhibited the most efficient energy dissipation capacity among the proposed dampers.

The performances of the cyclic loading tests are shown in **Table 9**. The dampers with the varying lengths of the cover tube and constant  $R_{ct}$  were used to examine their structural performances in cyclic loading tests. Considering design performances, the specimens with the SCT60-D, LCT60-2D dampers, and LCT60-3D damper were unsatisfactory, satisfactory, and high satisfactory performances, respectively.

### 5.8.2 Strains for the cover tube and buckling restrainer

**Fig. 5.25** to **Fig. 5.27** show the relationship between the axial load of the braces and the measured strains for BRKBs for each specimen. Considering beam-tip load,  $P$ , the axial load of the brace was obtained from moment equilibrium in the tested model. The vertical dashed lines indicate the yield strain, and the horizontal dashed lines represent the Euler buckling load of the buckling restrainer tube for base BRKB (L-BR). **Fig. 5.25(a)** and **Fig. 5.25(b)** illustrate the measured strains for the

buckling restrainer tubes, while **Fig. 5.25(c)** and **Fig. 5.25(d)** present the results of the strains of the cover tubes for each specimen.

For the specimen with the SCT60-D damper, the strain values induced in the buckling restrainer were noticeably smaller than the values induced in the cover tube, as shown in **Fig. 5.25(a)** and **Fig. 5.25(b)**. The strains on the buckling restrainer were symmetric among gauge positions 1 and 4. In contrast, an excessive asymmetric spreading of the strains was observed in gauge position 3, as shown in **Fig. 5.25(d)**. This behavior illustrates that the cyclic response of the damper with a  $l_{in} = D_{br}$  insertion length of the cover tube was not satisfactory.

For the specimen with the LCT60-2D damper, the buckling restrainer experienced dominant strains for the induced axial force, as shown in **Fig. 5.26(a)** and **Fig. 5.26(b)**. The cover tube strains remained in the elastic range except those at gauge positions 2 B and 3 B, as shown in **Fig. 5.26(c)** and **Fig. 5.26(d)**. As the load increased, the strain values at gauge positions 1 B, 4 B, and 4 D for the buckling restrainer, and the cover tube strains at gauge positions 2 B and 3 B exceeded the yield strain simultaneously, as shown in **Fig. 5.26(a)** to **Fig. 5.26(d)**.

For the specimen with the LCT60-3D damper, all the strain values for the buckling restrainer and cover tubes did not exceed the yield strain and met the Euler buckling criteria. The strain values for the cover tube and buckling restrainers were visibly lower than those of the other two specimens, as illustrated in **Fig. 5.27**. This behavior indicates that no plastic deformation or buckling failure occurred during the cyclic loading test for the damper in the specimen with the LCT60-3D damper.

### 5.8.3 Residual deformation after cyclic loading

**Fig. 5.28** shows the tested specimens and the residual deformation of the proposed BRKBs after the cyclic loading tests. **Fig. 5.28(a)** shows that the cover tube end of SCT60-D loses its stability owing to the insufficient insertion length for the given loads. Likewise, global buckling occurs in LCT60-2D when the cover tube insertion length increases by two times the insertion length in the damper in the specimen with the SCT60-D damper, as shown in **Fig. 5.28(b)**. Finally, the specimen with the LCT60-3D damper achieved superior performance when the system was carefully designed and detailed, as shown in **Fig. 5.28(c)**. These behaviors indicate that the damper stability capacity is strongly governed by the insertion length of the cover tube as long as the damper is designed to meet all the strength and stiffness requirements. Moreover, a detailed visual inspection of the disassembled BRKBs was conducted, and three failure patterns were observed for the buckling restrainers, cover tubes, and steel bar cores.

For the specimen with the SCT60-D damper, an undesirable plastic hinge at the upper edge of the cover tube began to occur at a low amplitude of cyclic loading and continuously developed up to the



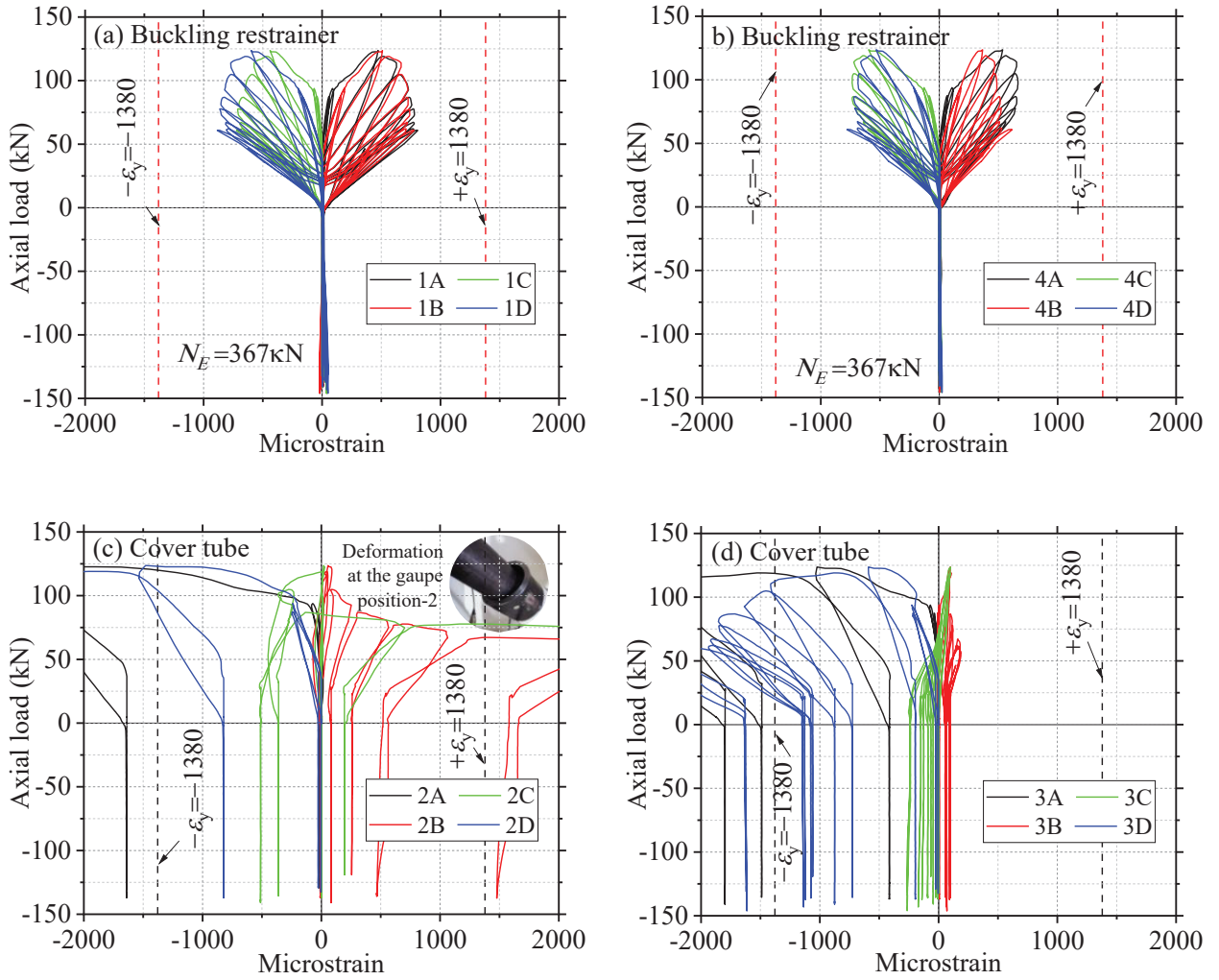


Fig. 5.25. Brace axial load and strain relations for specimen SCT60-D.

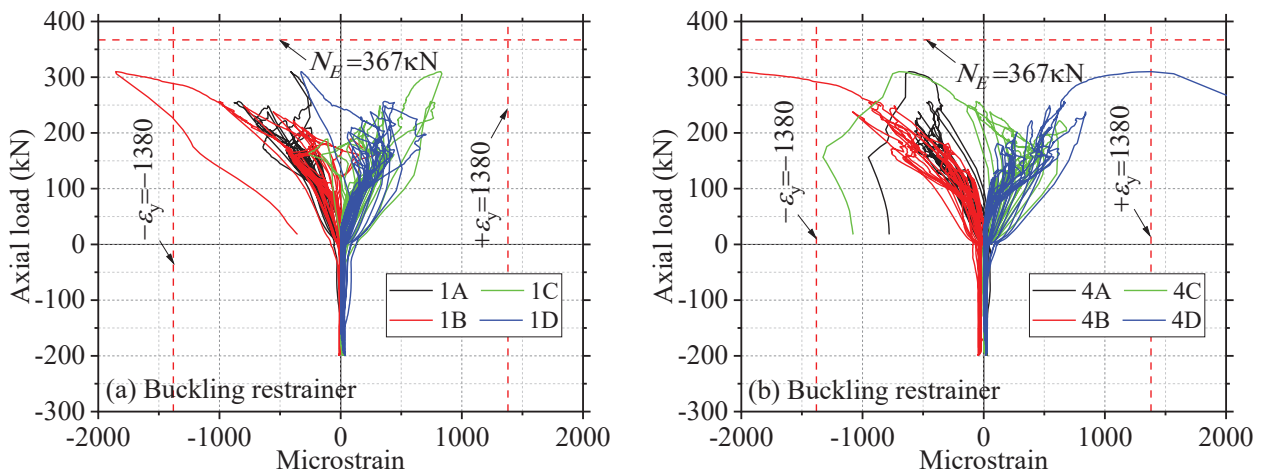


Fig. 5.26. Brace axial load and strain relations for specimen LCT60-2D.

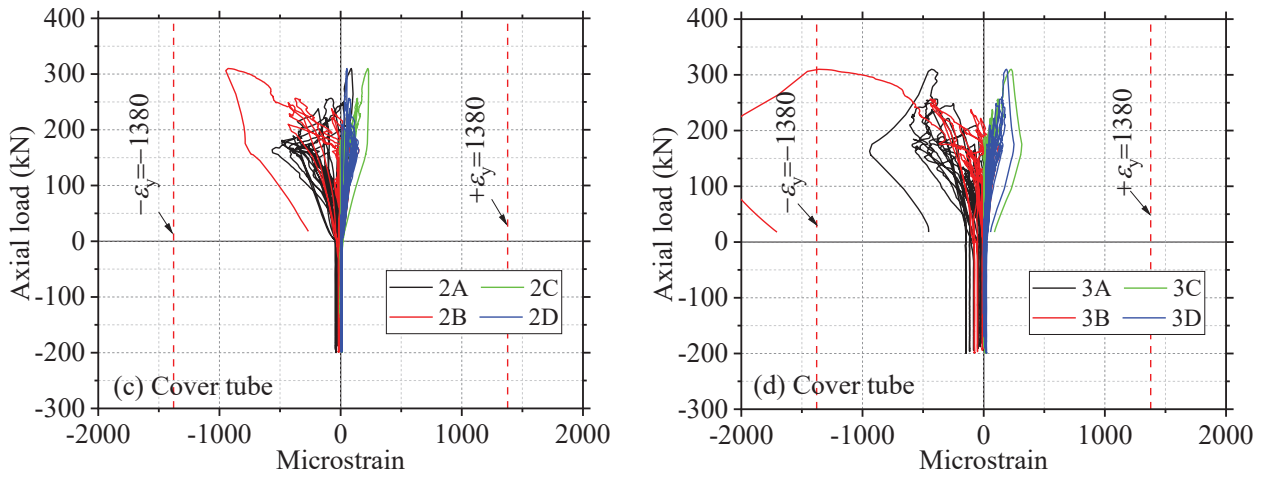


Fig. 5.26. Brace axial load and strain relations for specimen LCT60-2D (continued).

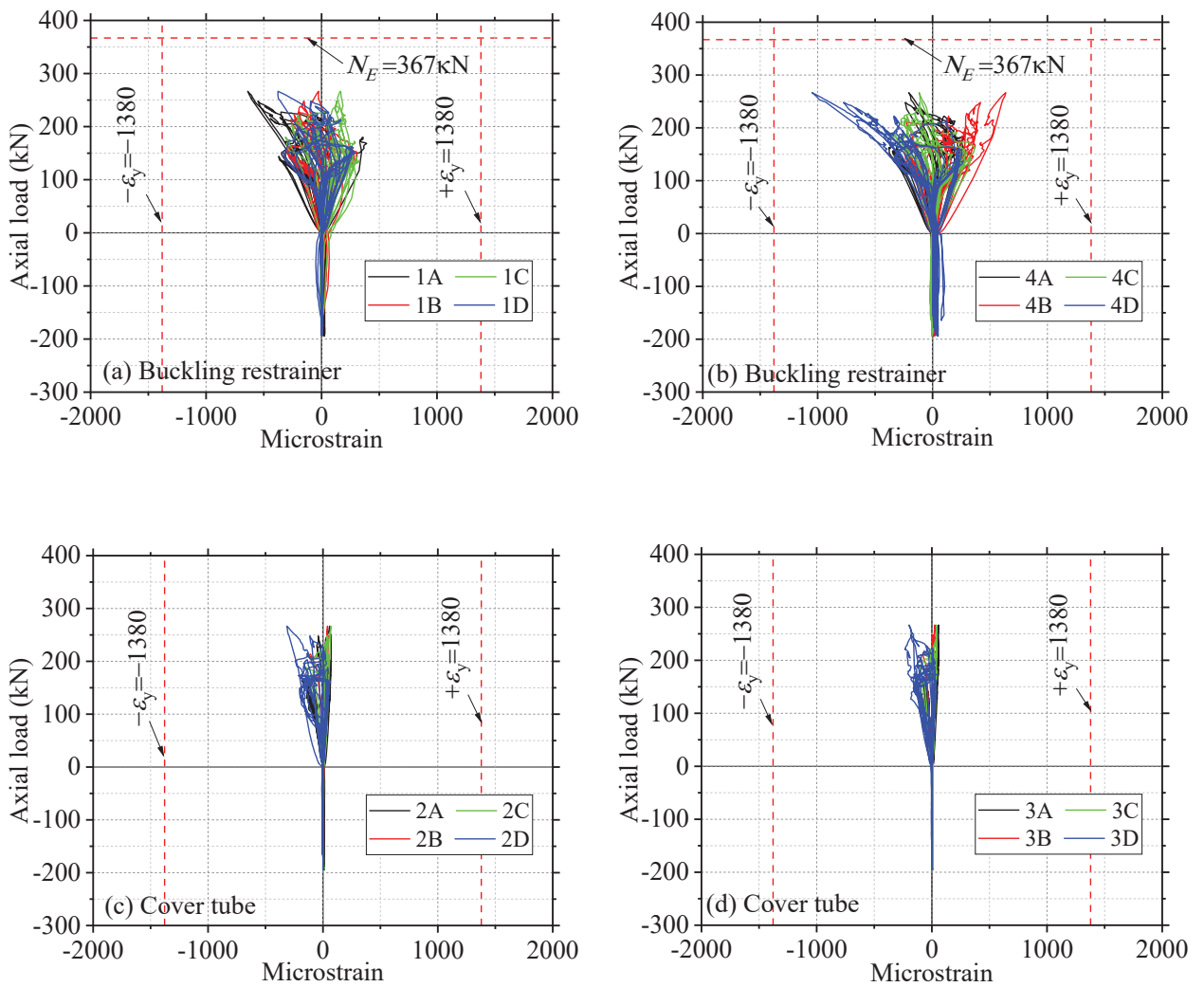
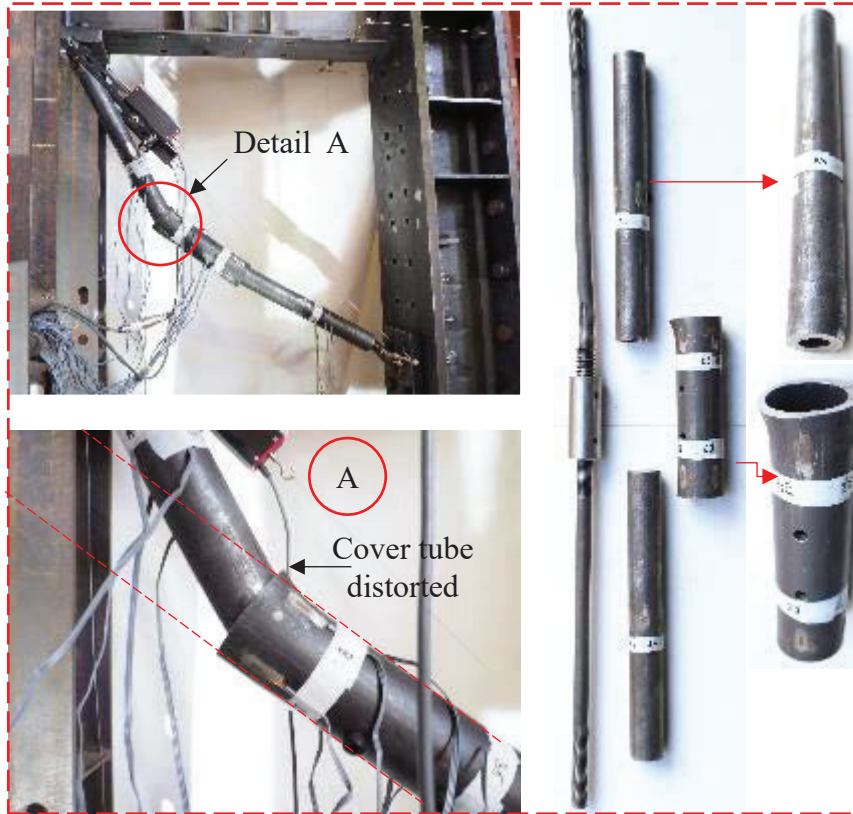
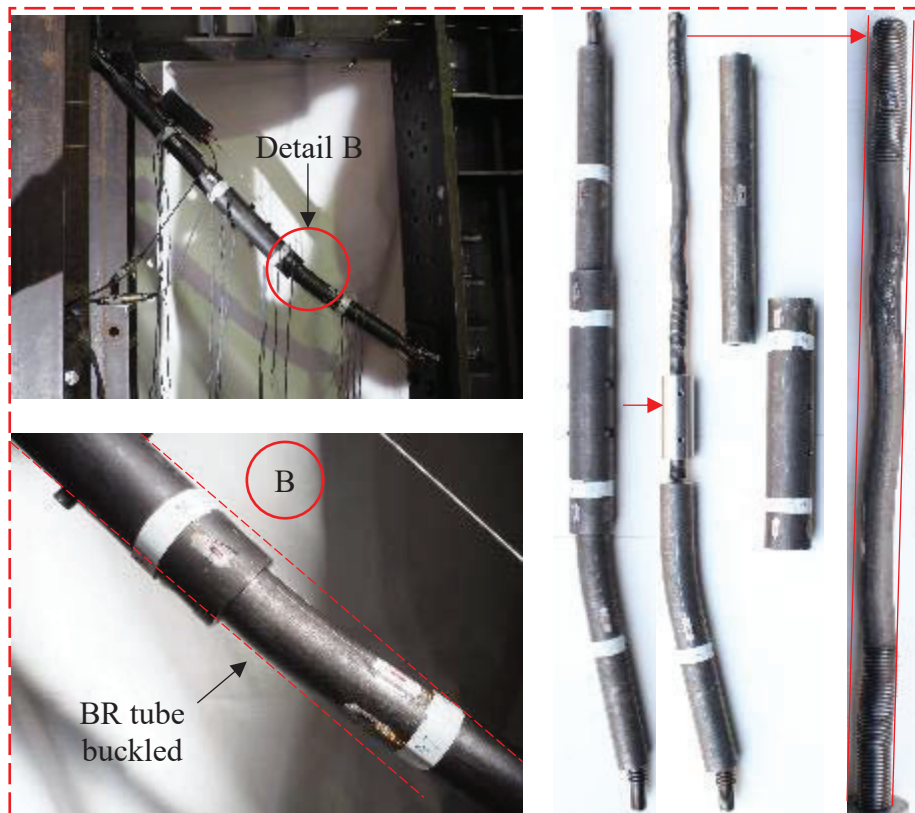


Fig. 5.27. Brace axial load and strain relations for specimen LCT60-3D.



(a) SCT60-D



(b) LCT60-2D

**Fig. 5.28.** Residual deformation in the final stage of cyclic loading for the BRKBs.



(c) LCT60-3D

**Fig. 5.28.** Residual deformation in the final stage of cyclic loading for the BRKBs (continued).

final loading stage. This failure mechanism leads to excessive plastic deformation at the edge of the cover tube and slight bending of the buckling restrainer and steel bar core, as shown in the right photo of **Fig. 5.28(a)**.

The specimen with the LCT60-2D damper was intended to be adequately involved in the plastic work for the given loads. However, it was revealed that the  $2D_{br}$  insertion length of the cover tube was insufficient to resist the relatively higher amplitude of the cyclic loading responses. Spiral buckling behavior was observed at the upper steel bar core, while the lower buckling restrainer, including the steel bar core, was slightly bent, as shown in the right photo of **Fig. 5.28(b)**.

After completion of all the cyclic loading stages, no severe failures were observed in the buckling restrainer and cover tubes for the specimen with the LCT60-3D damper. Higher mode buckling and spiral buckling simultaneously occurred in the lower and upper steel bar cores until the global rotation angle  $R(\text{rad}) = 4\%$  was reached. This behavior indicates that the  $3D_{br}$  insertion length of the cover tube in the BRKB is sufficient for plastic work. However, when the elongation of the steel bar core introduced in BRKBs exceeds the plastic limits at  $R(\text{rad}) = 0.04 - 2$ , (see point (iv) in **Fig. 5.24(c)**),

fractures occur at the screw part placed in the lower contraction allowance zone, as shown on the right photo of **Fig. 5.28(c)**.

The assessment of the  $R_{ct}$  for the cyclic loading tests against the compression loading tests is shown in **Table 9**. The specimen with the LCT60-3D damper showed high satisfaction for design purposes without a global buckling. In contrast, the specimen with the LCT60-2D damper was considered acceptable because the brace compression-to-tension ratio was achieved for design purposes, as shown in **Fig. 5.24(d)**.

## 6. CONCLUSIONS AND FUTURE RESEARCH NEED

### 6.1 Experimental and numerical study for assessment of spreading plasticity in RMC

#### 6.1.1 Conclusions

In sections 3 and 4, the cyclic behavior of RMCs with slender BRKB dampers was examined. First, T-shaped partial frame prototype models were tested with the proposed BRKBs to evaluate the load resistance ability of the braces and the plasticity behavior of the beams. An extensive numerical study was then performed to investigate the plasticity behavior of the beams and braces under one-way loading based on the test results. A steel core bar was used for the configuration of the proposed BRKBs, to downsize the connection between the KB and the beam flanges compared to conventional KBs. By adopting a slender BRKB in an RMC, a specific yielding sequence was formed near the beam and brace that was not observed in typical KB systems. The following conclusions can be drawn from this study.

- Relative to the beam length, shorter BRKBs provided better results in terms of dispersing plasticity along the beam during the numerical and experimental studies.
- Based on the extended numerical analysis, it was determined that a small-diameter steel core bar (M16) for BRKBs was less effective for the design purposes.
- Despite the thickness of the tube restrainer  $t = 1$  models, all M22 steel core bar BRKB models with  $SF < 1$  exhibited excellent ability to spread plasticity along the beams. However, a small safety factor cannot satisfy the stability requirements of the BRKBs.
- In contrast, in the M22 steel core bar BRKB models with  $SF > 1$ , yielding was initiated in the beam and brace simultaneously without failure of the brace, and plastic hinges were widened significantly along the beam, producing satisfactory behavior.
- Accordingly, it was concluded that the theoretical safety factor (value of at least one) of the proposed BRKBs could be achieved for the design purposes. The half clearance between the screw section of the steel core bar and restraining tube  $c_s/2$  should be controlled in the range of 1 to 2 mm for the models used in the case study.

#### 6.1.2 Future research need

These sections have evaluated the behavior of only certain welded beam-to-column connections using the proposed BRKB. However, more research is needed to evaluate the benefits of the proposed BRKB for whole RMC frames.

## 6.2 Experimental study for the novel slender BRKBs

### 6.2.1 Conclusions

The first half of this dissertation investigated the behavior of plasticity amplification on a rigid beam-to-column connection using a steel-core-bar round tube buckling-restrained knee brace damper BRKB under cyclic loading tests. This study showed that the proposed damper significantly reduced the stress concentration at the rigid beam-to-column connection. The second half of this study proposed and tested a novel long BRKB with a steel bar core damper using a round central coupler, tube restrainer, and a cover tube with weld-free beam-to-column connections. Overall, the experimental study was conducted in two stages.

In the first stage, compression loading tests were conducted on nine specimens, including the base damper, using a UH-F1000 pressure machine to evaluate the energy dissipation capacities upon the application of compression loads. In this stage, the insertion length,  $l_{in}$ , and the ratio of the section modulus of the cover tube against the buckling restrainer were examined.

In the second stage, based on the investigations in the first stage, extensive cyclic loading tests were carried out on three additional specimens with the BRKBs to investigate the effect of their insertion lengths on the cover tubes. In these tests,  $l_{in}$  was selected as the test parameter, and it was equal to  $D_{br}$ ,  $2D_{br}$ , and  $3D_{br}$  for each damper, where  $D_{br}$  denotes the outer diameter of the buckling restrainer.

As a result of both experimental studies, the following conclusions can be drawn.

- The advantages of the proposed damper are easy to assemble compared to conventional buckling-restrained braces and a high architectural flexibility for the retrofitting of large-span weld-free or welded steel moment-resisting systems.
- By increasing the number of contraction allowances, undesirable failure mechanisms that are global instability and local buckling of the restrainer ends can be suppressed effectively because the more uniform plastic deformation of the core bar can be achieved longitudinally. In other words, the adoption of several contraction allowance zones with proper design of the cover tubes for the proposed dampers significantly improves the performance of the proposed dampers.
- The study revealed that the damper stability capacity is governed by the insertion length of the cover tube,  $l_{in}$ , and ratio of the section modulus of the cover tube against the buckling restrainer,  $R_{ct}$ . For the compression responses of the proposed dampers, when the  $R_{ct}$  was less than 1.0, the damper could not achieve the design purpose regardless of the cover tube insertion length. When the  $R_{ct}$  was 1.7, it was observed that the specimen SCT54-D was

unsatisfactory. In contrast, the specimen LCT54-2D was satisfactory for the design performance. Finally, when the  $R_{ct}$  was 2.3, the specimens SCT57-D and LCT57-2D exhibited satisfactory and highly satisfactory, respectively.

- For the cyclic responses of the proposed dampers, the damper with the insertion length of  $l_{in} = 3D_{br}$  exhibited high satisfaction with the load-bearing capacity. An  $R_{ct}$  of 1.4 can be recommended when designing the proposed dampers if a sufficient insertion length is adopted for the proposed damper.

### *6.2.2 Future research need*

Overall, these experimental studies were performed on a specific number of test specimens to study the compression and cyclic behavior of the proposed dampers. Therefore, future research should investigate the behavior of a large number of damper models using finite element analysis.



**REFERENCES**

- [1] N. F. Youssef, D. Bonowitz, and J. L. Gross, "NISTIR 5625 A Survey of Steel Moment-Resisting Frame Buildings Affected by the 1994 Northridge Earthquake," *Build. Fire Res. Lab. Natl. Inst. Stand. Technol.*, vol. NISTIR 562, p. 173, 1995.
- [2] K. Horikawa and Y. Sakino, "Review of damage in welded joints caused by the Kobe earthquake," *Trans. JWRI*, vol. 24, no. 2, pp. 1–10, 1995.
- [3] M. D. Engelhardt and T. A. Sabol, "Reinforcing of steel moment connections with cover plates: benefits and limitations," *Eng. Struct.*, vol. 20, no. 4–6, pp. 510–520, 1998.
- [4] Q.-S. "Kent" Yu, C.-M. Uang, and J. Gross, "Seismic rehabilitation design of steel moment connection with welded haunch," *J. Struct. Eng.*, vol. 126, no. 1, pp. 69–78, 2000.
- [5] T. Balendra, E. L. Lim, and C. Y. Liaw, "Large-scale seismic testing of knee-brace-frame," *J. Struct. Eng.*, vol. 123, no. 1, pp. 11–19, 1997.
- [6] H.-L. Hsu and Z.-C. Li, "Seismic performance of steel frames with controlled buckling mechanisms in knee braces," *J. Constr. Steel Res.*, vol. 107, pp. 50–60, 2015.
- [7] E. Mele, "Moment resisting welded connections: an extensive review of design practice and experimental research in USA, Japan and Europe," *J. Earthq. Eng.*, vol. 6, no. 01, pp. 111–145, 2002.
- [8] R. O. Hamburger and J. O. Malley, *Seismic design of steel special moment frames*. US Department of Commerce, National Institute of Standards and Technology, 2016.
- [9] K. Inoue et al., "Full-Scale Test on Plastic Rotation Capacity of Steel Wide-Flange Beams Connected with Square Tube Steel Columns (Parti: Test Plan and Pilot Test)," *Kou kousou rombunshuu*, vol. 4, no. 16, pp. 27–42, 1997.
- [10] T. Nagao, T. Tanaka, and H. Nanaba, "Performance of beamcolumn connections in steel structures," 2004.
- [11] A. Asghari and S. Saharkhizan, "Seismic design and performance evaluation of steel frames with knee-element connections," *J. Constr. Steel Res.*, vol. 154, pp. 161–176, 2019.
- [12] T. Balendra, M.-T. Sam, C.-Y. Liaw, and S.-L. Lee, "Preliminary studies into the behaviour of knee braced frames subject to seismic loading," *Eng. Struct.*, vol. 13, no. 1, pp. 67–74, 1991.

## References

- [13] T. Balendra, M.-T. Sam, and C.-Y. Liaw, "Diagonal brace with ductile knee anchor for aseismic steel frame," *Earthq. Eng. & Struct. Dyn.*, vol. 19, no. 6, pp. 847–858, 1990.
- [14] T. Balendra, E.-L. Lim, and S.-L. Lee, "Ductile knee braced frames with shear yielding knee for seismic resistant structures," *Eng. Struct.*, vol. 16, no. 4, pp. 263–269, 1994.
- [15] M. Mahmoudi, S. Montazeri, and M. J. S. Abad, "Seismic performance of steel X-knee-braced frames equipped with shape memory alloy bars," *J. Constr. Steel Res.*, vol. 147, pp. 171–186, 2018.
- [16] A. Asghari and A. H. Gandomi, "Ductility reduction factor and collapse mechanism evaluation of a new steel knee braced frame," *Struct. Infrastruct. Eng.*, vol. 12, no. 2, pp. 239–255, 2016.
- [17] J. D. Aristizabal-Ochoa, "Disposable knee bracing: improvement in seismic design of steel frames," *J. Struct. Eng.*, vol. 112, no. 7, pp. 1544–1552, 1986.
- [18] M. Mofid and P. Khosravi, "Non-linear analysis of disposable knee bracing," *Comput. & Struct.*, vol. 75, no. 1, pp. 65–72, 2000.
- [19] Z. Huang, L. Qing-song, and C. Long-zhu, "Elastoplastic analysis of knee bracing frame," *J. Zhejiang Univ. A*, vol. 6, no. 8, pp. 784–789, 2005.
- [20] S. Leelataviwat, B. Suksan, J. Srechai, and P. Warnitchai, "Seismic Design and Behavior of Ductile Knee-Braced Moment Frames," *J. Struct. Eng.*, vol. 137, no. 5, pp. 579–588, 2011, doi: 10.1061/(asce)st.1943-541x.0000301.
- [21] P. Chusilp and K. Suita, "Full-scale tests for seismic performance verification of steel building structures with hysteretic dampers," *京都大学防災研究所年報. C*, vol. 47, no. C, pp. 201–214, 2004.
- [22] A. Watanabe, Y. Hitomi, E. Saeki, A. Wada, and M. Fujimoto, "Properties of brace encased in buckling-restraining concrete and steel tube," in *Proceedings of ninth world conference on earthquake engineering*, 1988, vol. 4, pp. 719–724.
- [23] M. Iwata, T. Kato, and A. Wada, "Buckling-restrained braces as hysteretic dampers," *Behav. steel Struct. Seism. areas*, pp. 33–38, 2000.
- [24] D. Kawai, Y. Koetaka, K. Suita, K. Inoue, N. Uno, and Y. Fukuchi, "Mechanical behavior and design method of weld-free steel structure with knee brace damper using square tube column".

## References

- [25] J. Kim and Y. Seo, "Seismic design of steel structures with buckling-restrained knee braces," *J. Constr. steel Res.*, vol. 59, no. 12, pp. 1477–1497, 2003.
- [26] E. Junda, S. Leelataviwat, and P. Doung, "Cyclic testing and performance evaluation of buckling-restrained knee-braced frames," *J. Constr. Steel Res.*, vol. 148, pp. 154–164, 2018.
- [27] A. N. Tak, S. R. Mirghaderi, and M. Dargahi, "Plastic design of knee-element connection frames (KCFs) using mechanism control," *J. Constr. Steel Res.*, vol. 173, p. 106247, 2020.
- [28] Y. BYAKUNO, Y. KOETAKA, K. INOUE, and S. MOROOKA, "Design and experimental verification on the performance of the buckling-restrained knee brace," *Kou kouzou rombunshuu*, vol. 12, no. 45, pp. 233–241, 2005.
- [29] J. A. S. Mateus, H. Tagawa, and X. Chen, "Buckling-restrained steel bar damper for spine frame system," *Eng. Struct.*, vol. 229, p. 111593, 2021.
- [30] K. Inoue, K. Suita, I. Takeuchi, P. Chusilp, M. Nakashima, and F. Zhou, "Seismic-resistant weld-free steel frame buildings with mechanical joints and hysteretic dampers," *J. Struct. Eng.*, vol. 132, no. 6, pp. 864–872, 2006.
- [31] H. Tagawa and S. Kaneko, "Cyclic performance of buckling-restrained knee brace damper with U-shaped holes," in *Proceedings of the Seventh Asia Conference on Earthquake Engineering*, Bangkok, Thailand, 2018, pp. 22–25.
- [32] S. Pampanin, "Emerging solutions for high seismic performance of precast/prestressed concrete buildings," *J. Adv. Concr. Technol.*, vol. 3, no. 2, pp. 207–223, 2005.
- [33] F. Sarti, A. Palermo, and S. Pampanin, "Fuse-type external replaceable dissipaters: Experimental program and numerical modeling," *J. Struct. Eng.*, vol. 142, no. 12, p. 4016134, 2016.
- [34] C.-L. Wang, Y. Liu, and L. Zhou, "Experimental and numerical studies on hysteretic behavior of all-steel bamboo-shaped energy dissipaters," *Eng. Struct.*, vol. 165, pp. 38–49, 2018.
- [35] Y. Liu, C.-L. Wang, and J. Wu, "Development of a new partially restrained energy dissipater: Experimental and numerical analyses," *J. Constr. Steel Res.*, vol. 147, pp. 367–379, 2018.
- [36] S. Yang, D. Guan, L.-J. Jia, Z. Guo, and H. Ge, "Local bulging analysis of a restraint tube in a new buckling-restrained brace," *J. Constr. Steel Res.*, vol. 161, pp. 98–113, 2019.
- [37] H. Tagawa, Y. Nagoya, and X. Chen, "Bolted beam-to-column connection with buckling-restrained round steel bar dampers," *J. Constr. Steel Res.*, vol. 169, p. 106036, 2020.

## References

- [38] S. Fujii and H. Tagawa, “Experimental study on buckling-restrained braces using round steel bar cores and double steel tubes,” *J Struct Constr Eng, Arch. Inst Jpn*, vol. 650, pp. 879–885, 2010.
- [39] H. Tamai and T. Takamatsu, “Cyclic loading tests on a non-compression brace considering performance-based seismic design,” *J. Constr. Steel Res.*, vol. 61, no. 9, pp. 1301–1317, 2005.
- [40] J. A. S. Mateus, H. Tagawa, and X. Chen, “Buckling-restrained brace using round steel bar cores restrained by inner round steel tubes and outer square steel tube,” *Eng. Struct.*, vol. 197, p. 109379, 2019.
- [41] M. Fujimoto, A. Wada, E. Saeki, A. Watanabe, and Y. Hitomi, “A Study on the Unbonded Brace Encased in Buckling-Restraining Concrete and Steel Tube,” *J. Struct. Eng. AIJ*, vol. 34B, pp. 24–58, 1988.
- [42] Q. Xie, “State of the art of buckling-restrained braces in Asia,” *J. Constr. steel Res.*, vol. 61, no. 6, pp. 727–748, 2005.
- [43] T. Takeuchi and A. Wada, *Buckling-restrained braces and applications*. Japan Society of Seismic Isolation Tokyo, 2017.
- [44] S. A. C. J. V. G. D. Committee, S. A. C. J. Venture, S. E. A. of California, A. T. Council, and C. U. for Research in Earthquake Engineering, *Recommended Seismic Evaluation and Upgrade Criteria for Existing Welded Steel Moment-frame Buildings*, vol. 351. Federal Emergency Management Agency, 2000.
- [45] H. Sugihardjo and others, “Cumulative Ductility and Hysteretic Behavior of Small Buckling-Restrained Braces,” *Adv. Civ. Eng.*, vol. 2017, 2017.
- [46] T. Munkhunur, H. Tagawa, and C. Xingchen, “FINITE ELEMENT ANALYSIS OF STEEL BEAM-TO-COLUMN JOINTS STRENGTHENED BY BUCKLING-RESTRAINED KNEE BRACING USING STEEL BAR CORES,” 2019.
- [47] AISC ANSI/AISC 341-16, “Seismic Provisions for Structural Steel Buildings,” Tech, rep, 2016.
- [48] ANSYS, “User’s Manual.” ANSYS, inc, USA, 2014.
- [49] H. Heidary-Torkamani and S. Maalek, “Conceptual numerical investigation of all-steel Tube-in-Tube buckling restrained braces,” *J. Constr. Steel Res.*, vol. 139, pp. 220–235, 2017.
- [50] W. H. Pan, J. Z. Tong, Y. L. Guo, and C. M. Wang, “Optimal design of steel buckling-restrained braces considering stiffness and strength requirements,” *Eng. Struct.*, vol. 211, p. 110437, 2020.

## References

- [51] R. W. K. Chan and F. Albermani, “Buckling-restrained-lug connection for energy dissipation,” *Adv. Struct. Eng.*, vol. 16, no. 1, pp. 11–20, 2013.
- [52] A. Elkady and D. G. Lignos, “Analytical investigation of the cyclic behavior and plastic hinge formation in deep wide-flange steel beam-columns,” *Bull. Earthq. Eng.*, vol. 13, no. 4, pp. 1097–1118, 2015.

**APPENDIX A**

In this appendix, to assess the spreading of plasticity around typical knee braced beams in a moment connection, three different section areas of equal-sided double angles TKB beam models were analyzed. Their results are discussed in Table A1. Furthermore, the results of stress distributions for each TKB beam model are plotted in Figs. A1 and A2 and are compared with the proposed BRKB damper for the global relative rotation 0.02 and 0.05 radians. The numerical analysis method used in this section is the same as the method used in section 4. The relationships between an axial load and axial deformation of the TKBs are shown in Fig. A3. In which their results are compared with the results of the proposed BRKB damper. Fig. A4 illustrates relationships between load and global relative rotation for each TKB beam, in which the red color indicates the results of the proposed BRKB damper.

As shown in Fig. A3(c) and Fig. A4(c), although it seems that TKB ( $\perp$  40x5) is very efficient for our design purpose, the large strength and stiffness of TKB do not cause the spreading of plasticity at the beam as our proposed damper. The strength increases gradually in the KB tension side for each TKB beam within -0.04 radian, while the strength in the KB compression side degrades compared to the KB tension side. Because flexural buckling of the TKBs causes excessive lateral deflection and it continuously occurs for given further loads (see Fig. A4 (a), (b), and (c)).

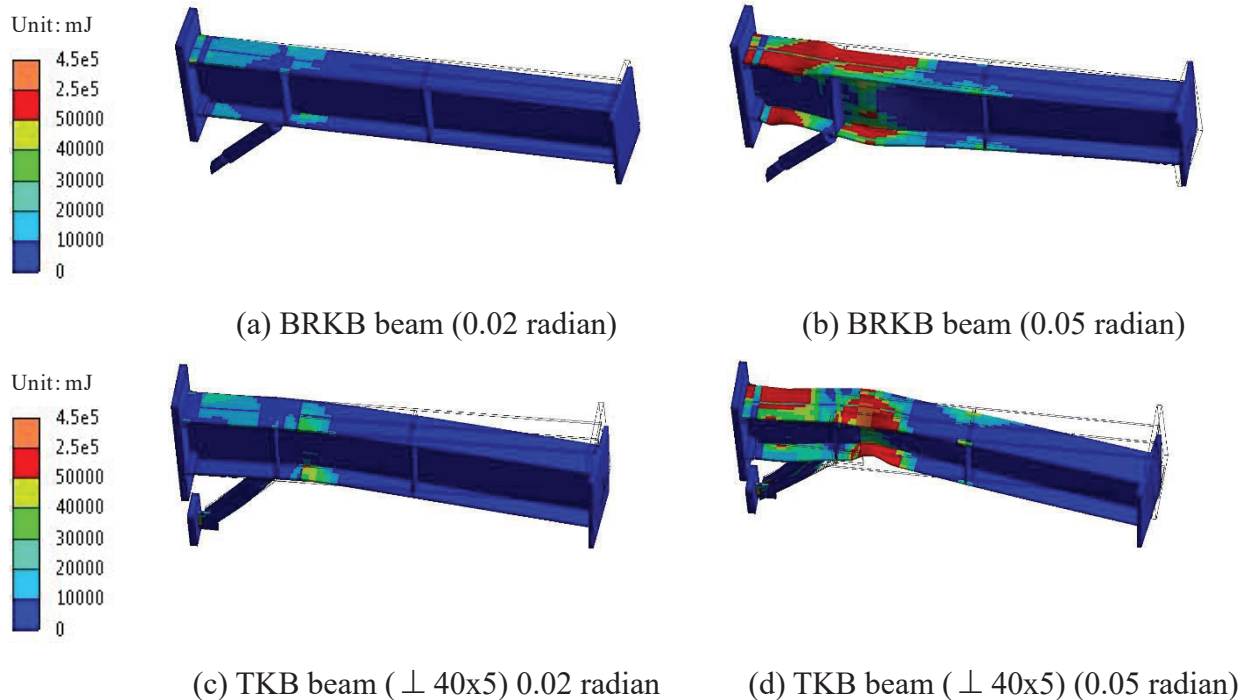


**Fig. A1.** Plastic strain energies for the BRKB and TKB ( $\perp$  40x5) beams regarding 0.02 and 0.05 radians of loading.

Appendix A

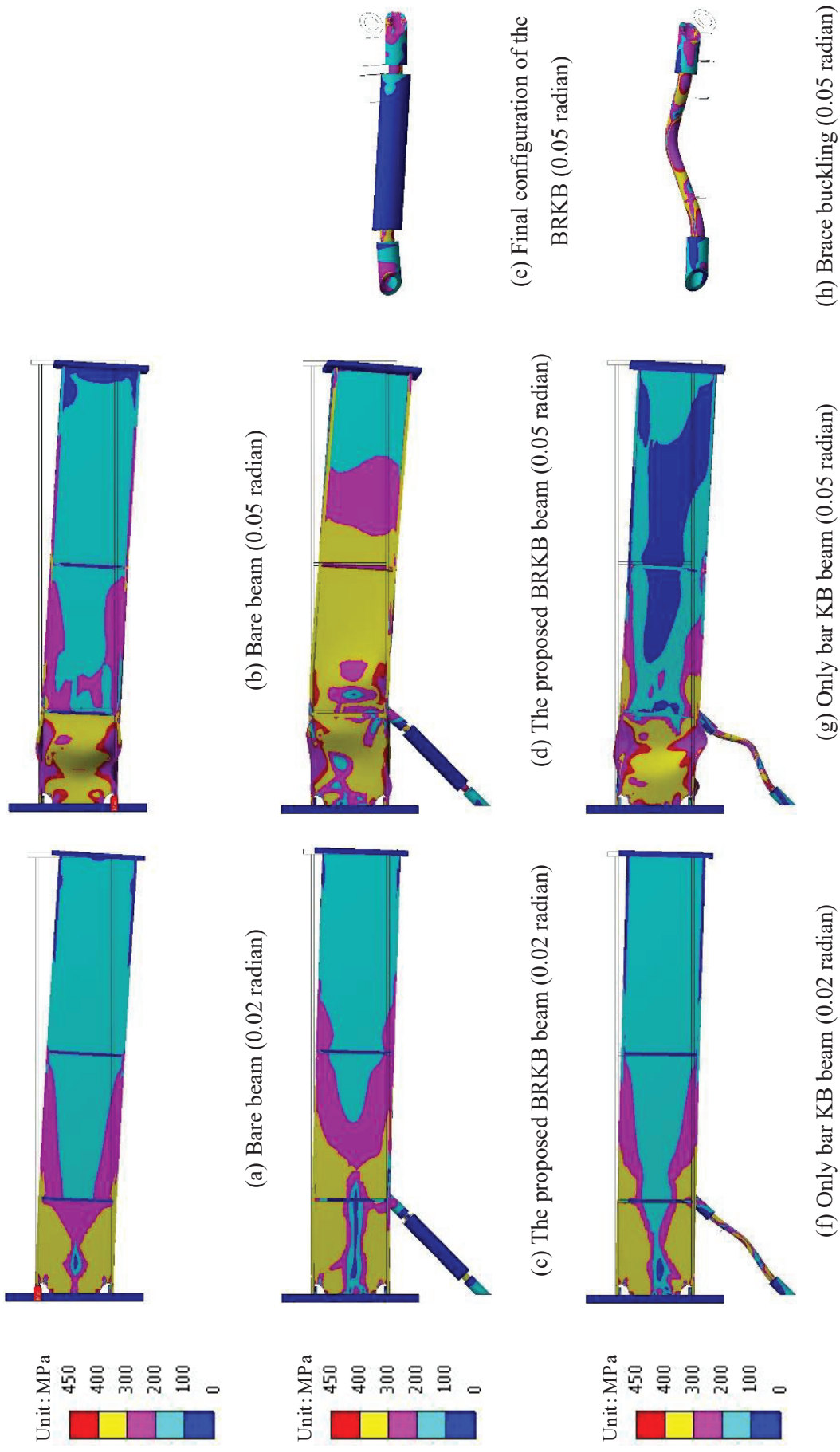


**Fig. A2.** Equivalent Von-Mises stress distributions regarding 0.02 and 0.05 radians of loading.

Appendix A

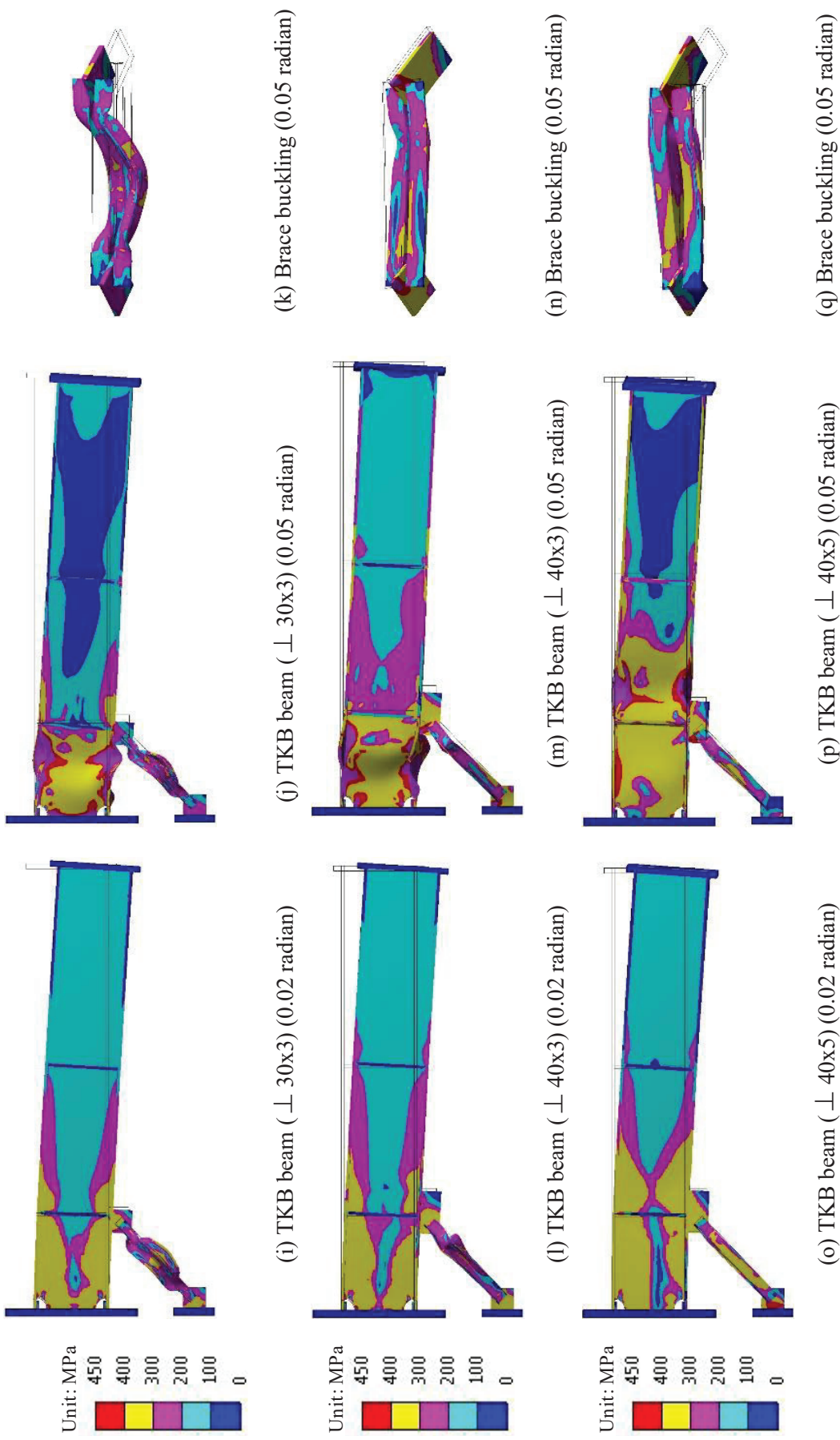
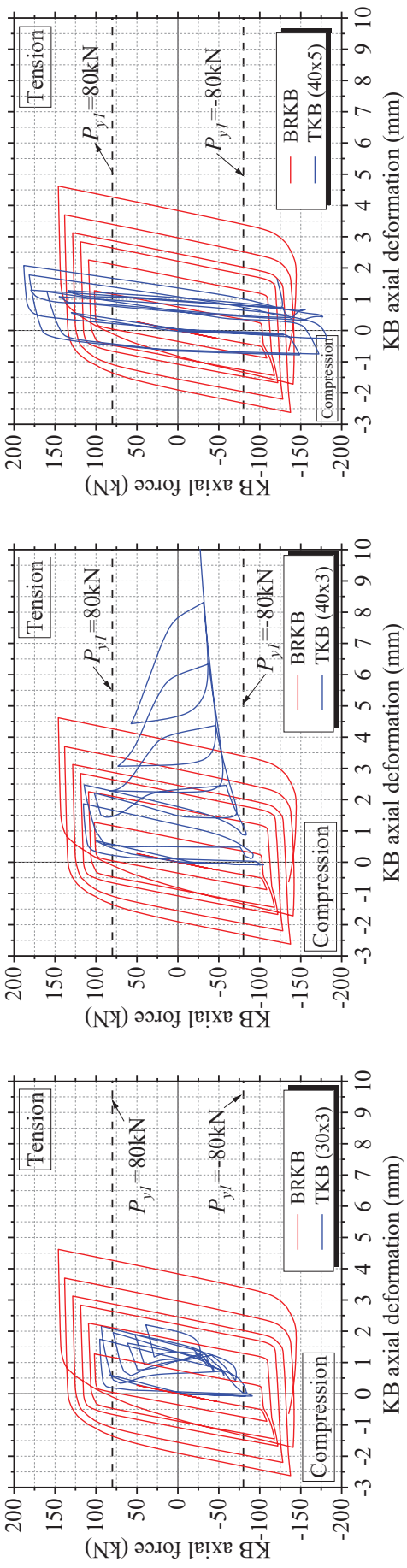


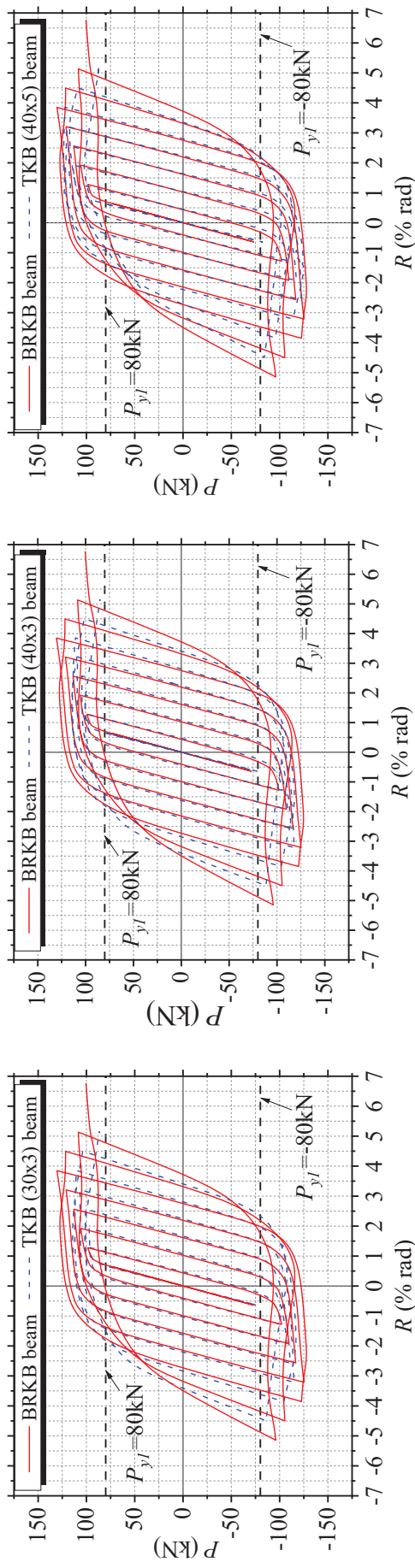
**Fig. A2** Equivalent Von-Mises stress distributions regarding 0.02 and 0.05 radians of loading (Continued).





(a) TKB ( $\perp$  30x3) (b) TKB ( $\perp$  40x3) (c) TKB ( $\perp$  40x5)

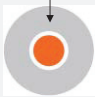




**Fig. A3.** Relationship between an axial load and axial deformation of the TKBs.



(a) TKB ( $\perp$  30x3) (b) TKB ( $\perp$  40x3) (c) TKB ( $\perp$  40x5)

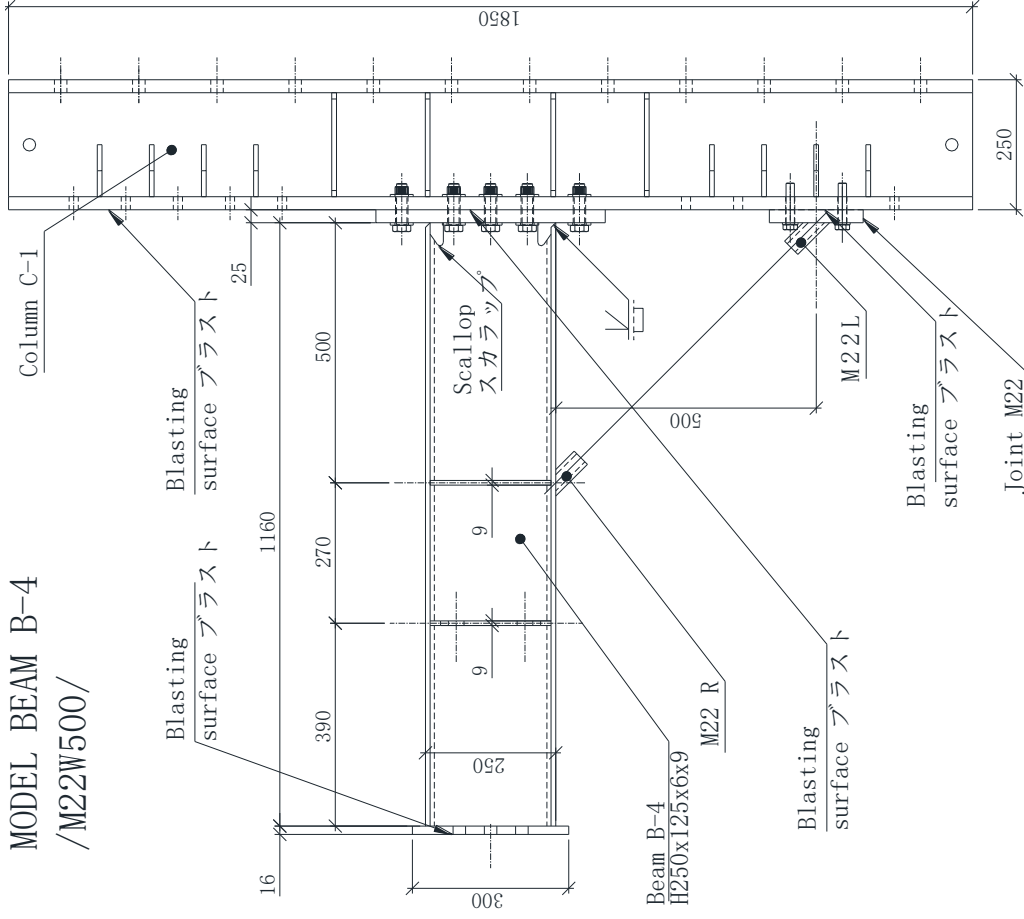
**Fig. A4.** Relationship between load and global relative rotation for the TKB beam models.

**Table A1** – Assessment of the spreading of plasticity for the TKB beams

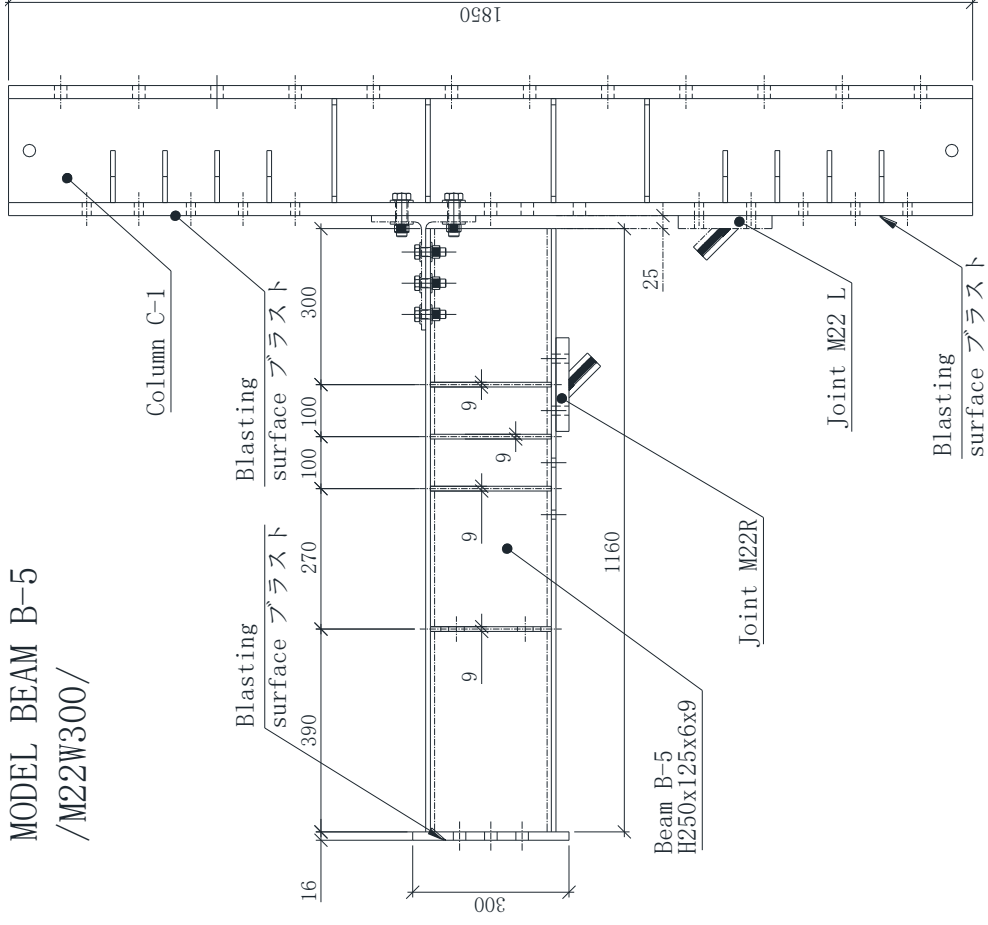
Model name	Knee braces		Description of the plasticity spreading behavior
	Configurations	Section-area (mm <sup>2</sup> )	
<b>Bare beam</b>	-	-	Stress is concentrated in the beam end (see Fig. A1 (a) and (b)).
<b>The proposed BRKB beam</b>	Buckling restrainer 	320 (Core bar)	Stress and plastic strain energy in the beam-end are spreading due to the proposed damper, as shown in Fig. A1 (c), (d), and (e), and Fig. A2 (a), (b), respectively.
<b>Only bar KB beam</b>		320	Stress is concentrated in the beam end (see Fig. A1 (f), (g), and (h)).
<b>TKB beam (⊥ 30x3)</b>		345	The cross-section area of the TKB is close to the steel core bar, where stress is concentrated in the beam end due to the lack of stability of the TKB (see Fig. A1 (i), (j), and (k) and Fig. A3 (a)).
<b>TKB beam (⊥ 40x3)</b>		467	The cross-section area of the TKB, which was obtained based on the design theory of section 2, is larger than the steel core bar, where the stress is concentrated in the beam end due to the lack of stability of the TKB (see Fig. A1 (l) (m), and (n) and A3 (b)).
<b>TKB beam (⊥ 40x5)</b>		751	The cross-section area of the TKB is larger than the area that is obtained by the design theory of section 2, where the stress spreading behavior is similar to the proposed system (see Fig. A1 (o), (p), and (q)). However, excessive strength and stiffness of the TKB induce the large plastic strain energy outside of the KB portion at the beam (see Fig. A2 (c) and (d), and Fig. A3 (c)).

APPENDIX B

MODEL BEAM B-4  
/M22W500/



MODEL BEAM B-5  
/M22W300/

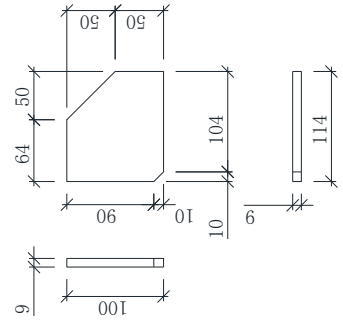
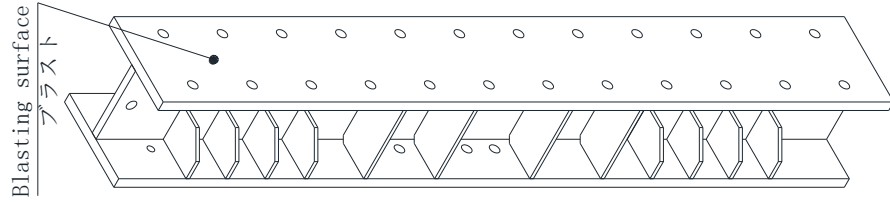


Appendix B

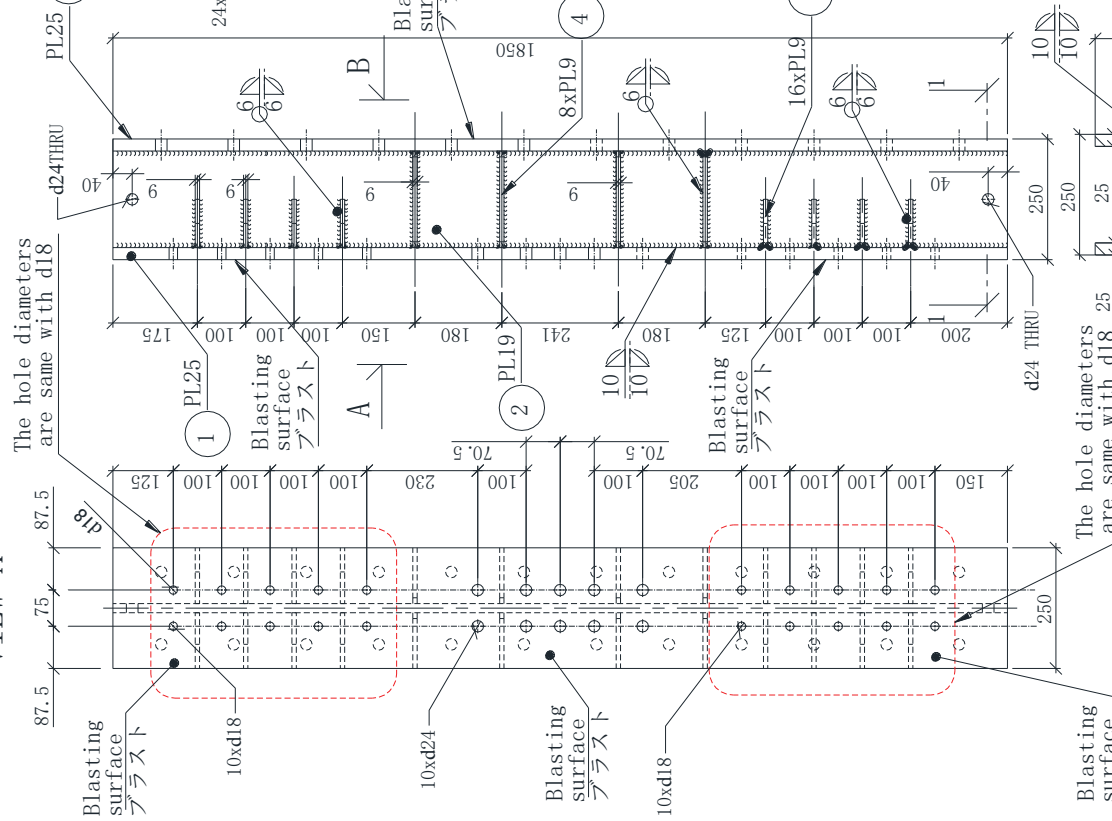
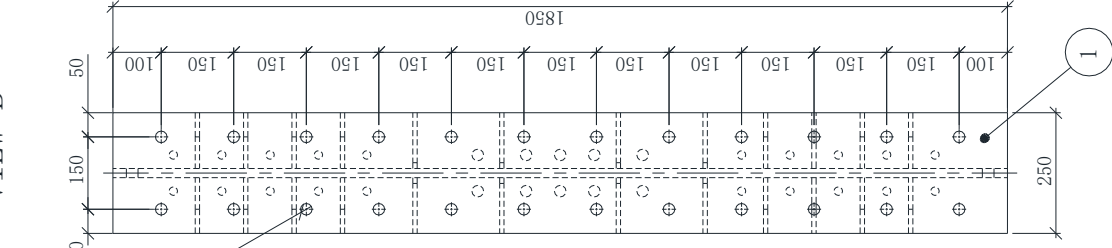
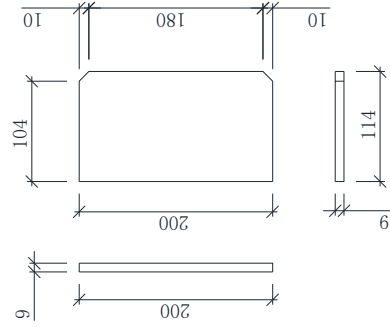
COLUMN C-1

VIEW-B

ITEM NO3. PL9



ITEM NO4. PL9



1. If the geometric dimensions of Item number 4 and 3 are interfere for the fabrication, a fabricator can readjust them.

SECTION 1-1

ITEM NO.	PART NUMBER	DESCRIPTION	Tot. WEL.WEIGHT/Kg/	QTY.
1	PL 25	-1850x250x25	181.5	2
2	PL 19	-1850x200x19	55.19	1
3	PL 9	-200x114x9	25.76	16
4	PL 9	-114x100x9	6.84	8
Total weight /Kg/			269.29	

Appendix B

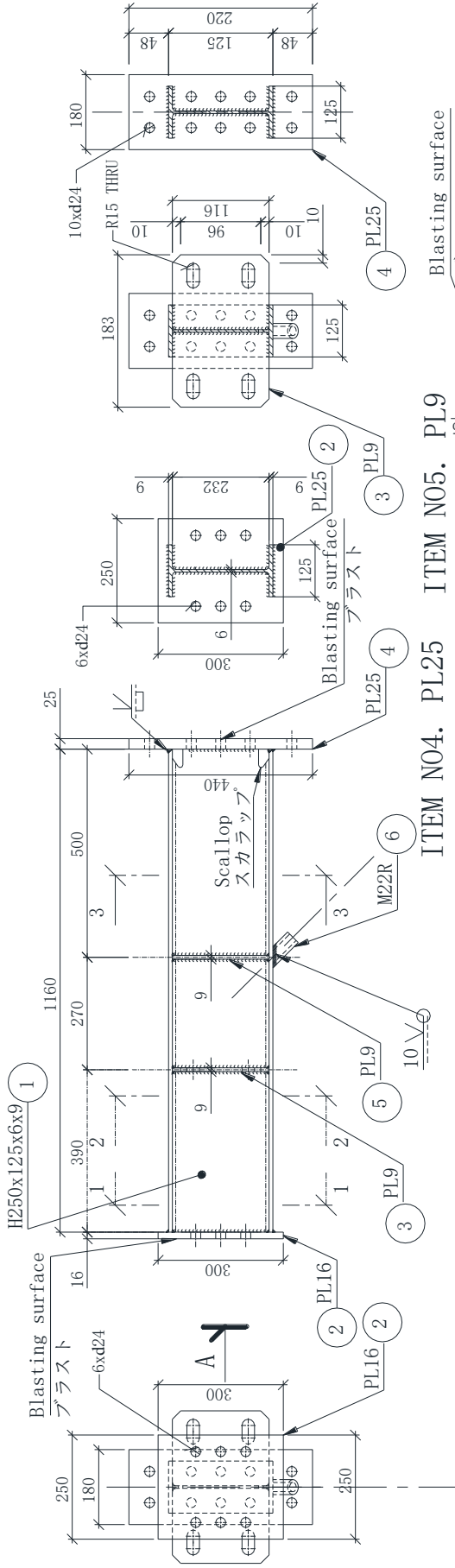
VIEW-A

BEAM B-4 / M22W500

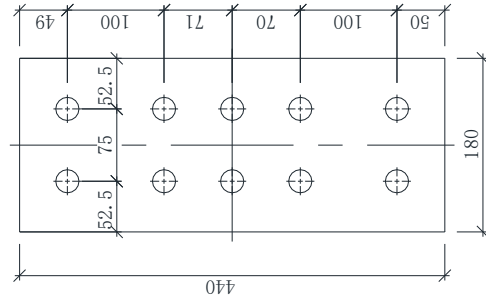
SECTION 1-1

SECTION 2-2

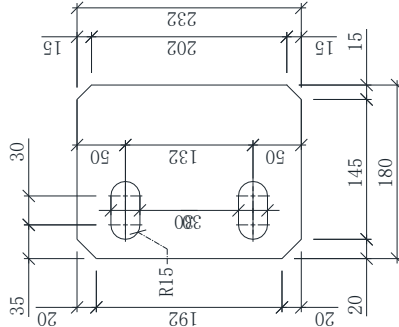
SECTION 3-3



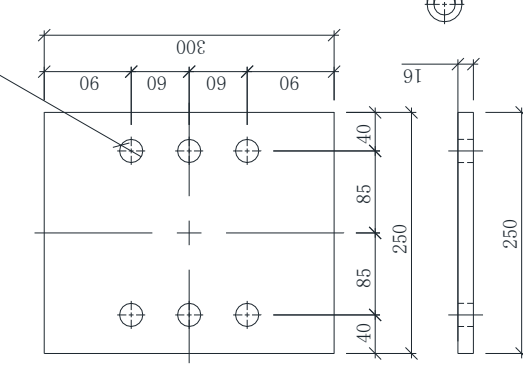
ITEM N04. PL25



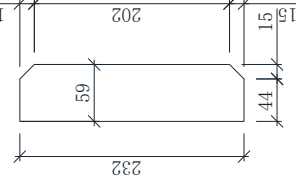
ITEM N03. PL9



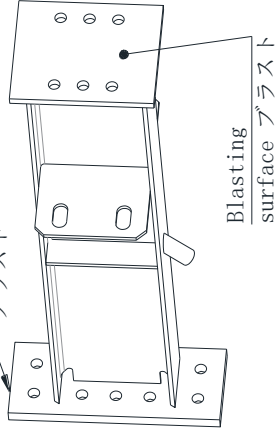
ITEM N02. PL16



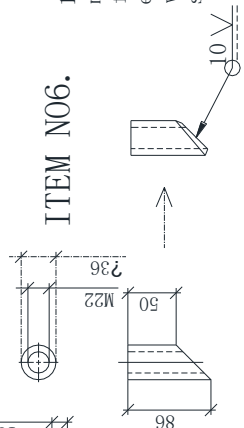
ITEM N05. PL9



ITEM N06.



ITEM N06.

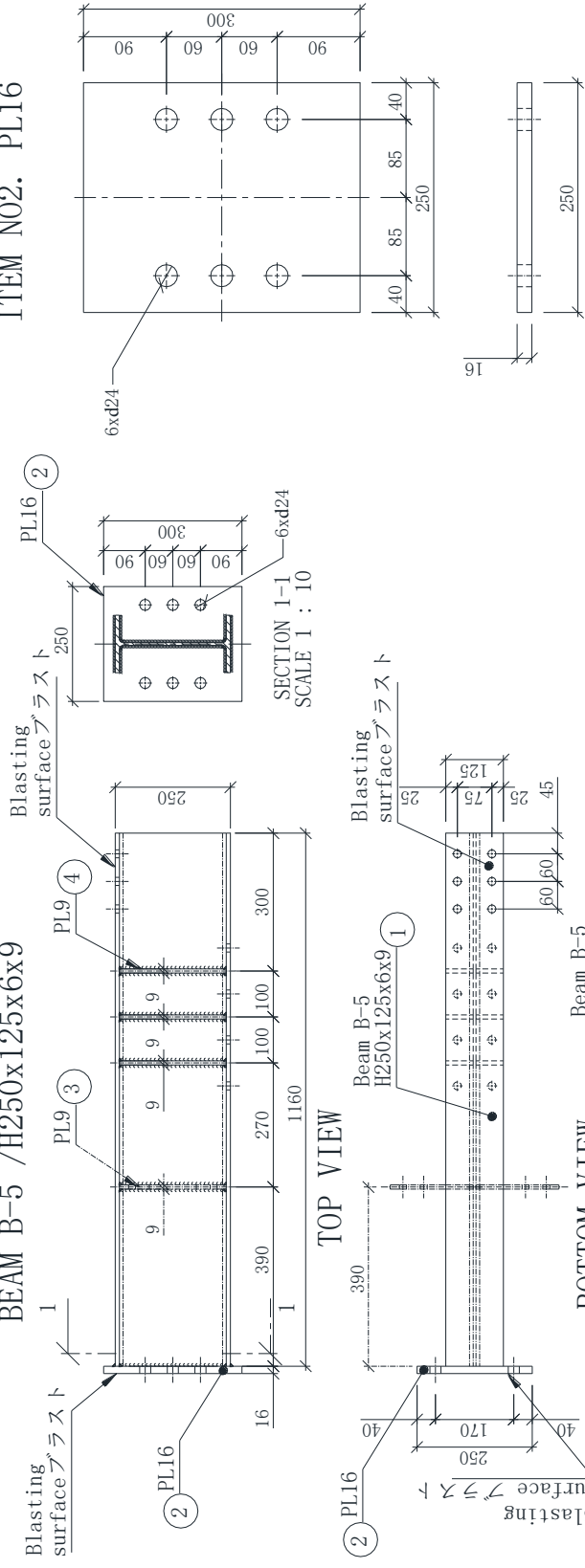


1. "V" groove welding method must be used for the item n06 element regarding with the welding standard.

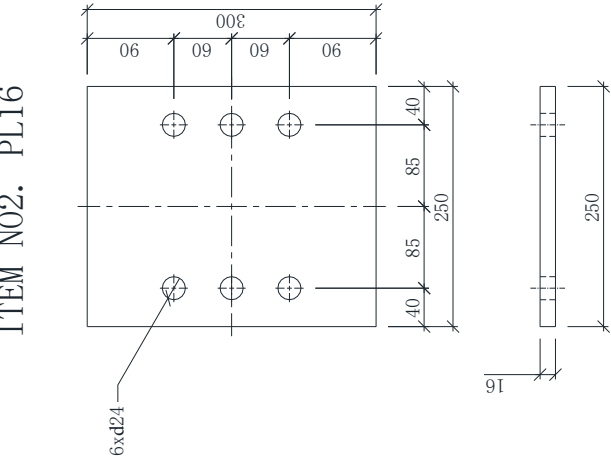
PART NUMBER	DESCRIPTION	Tot. WEI. /Kg/	QTY.	
1	Beam B-4	H250x125x6x9	29	1
2	PL 16	-300x250x16	9.42	1
3	PL 9	-232x180x9	5.9	2
4	PL 25	-440x180x25	15.54	1
5	PL 9	-232x59x9	1.94	2
6	M22R	? 36xM22	0.43	1
7	Total weight /Kg/		62.1	

Appendix B

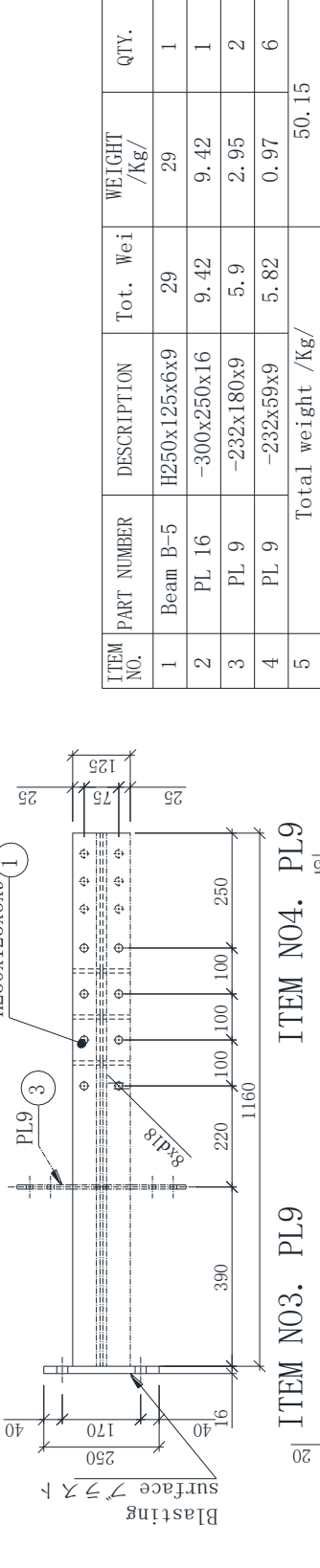
BEAM B-5 / H250x125x6x9



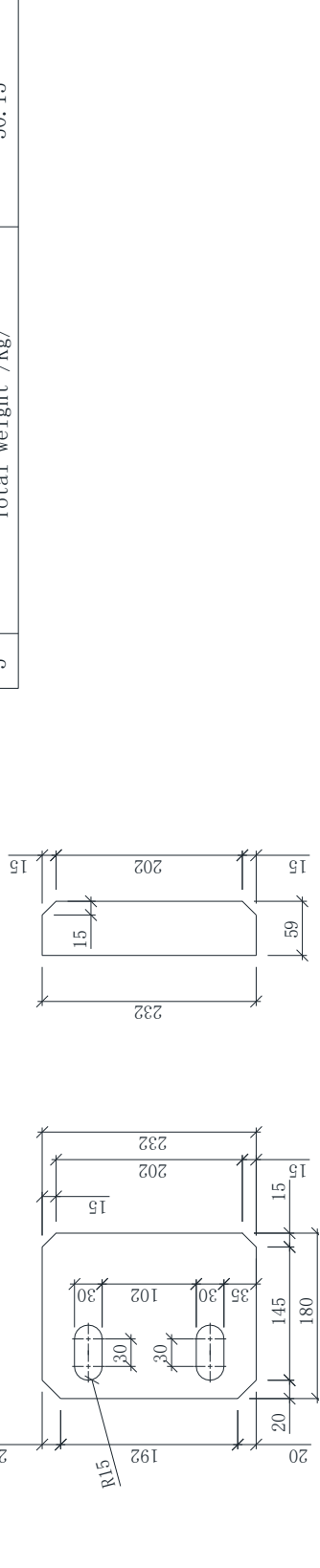
ITEM NO2. PL16



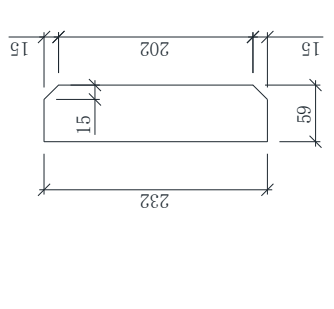
BEAM B-5 / H250x125x6x9



ITEM NO3. PL9



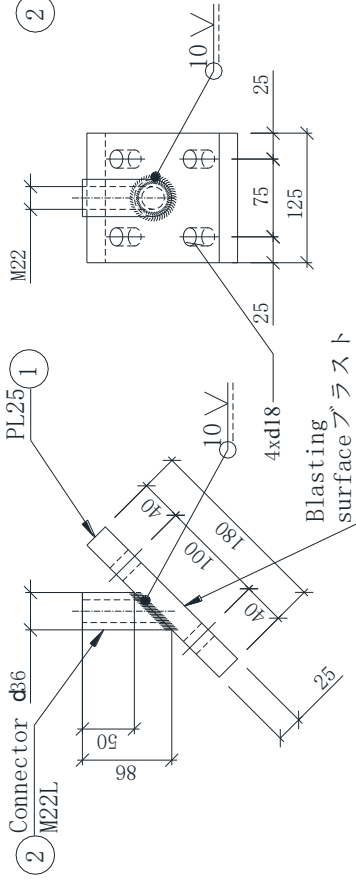
ITEM NO4. PL9



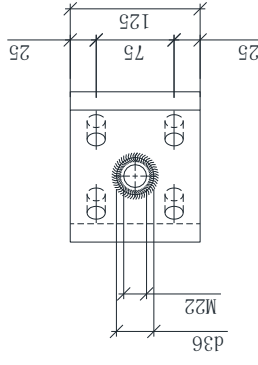
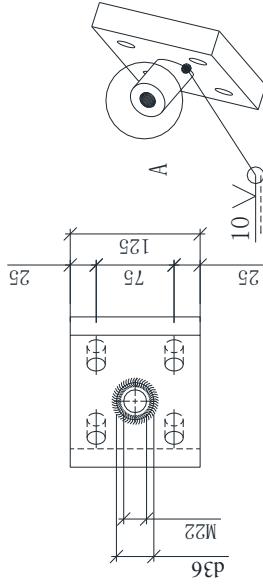
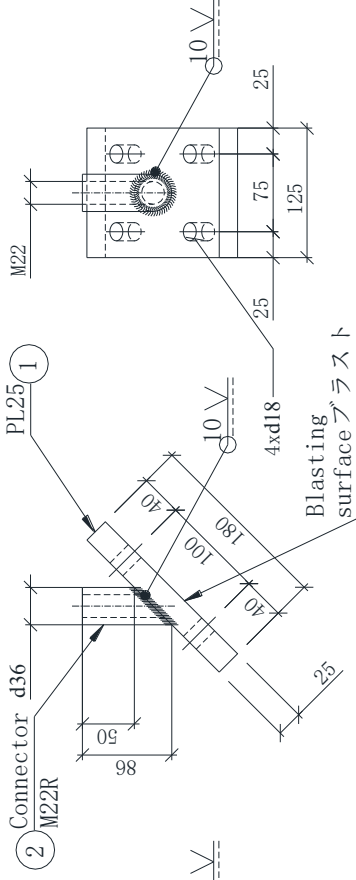
ITEM NO.	PART NUMBER	DESCRIPTION	Tot. Wei	WEIGHT /Kg/	QTY.
1	Beam B-5	H250x125x6x9	29	29	1
2	PL 16	-300x250x16	9.42	9.42	1
3	PL 9	-232x180x9	5.9	2.95	2
4	PL 9	-232x59x9	5.82	0.97	6
Total weight /Kg/				50.15	

Appendix B

JOINT M22L / n=1/



JOINT M22R / n=1/



1. "V" groove welding method must be used between bolts and plates regarding with the welding standard.
2. Contact surface must be blast on the target surface as shown in this figure.
3. n=2 total quantity number.

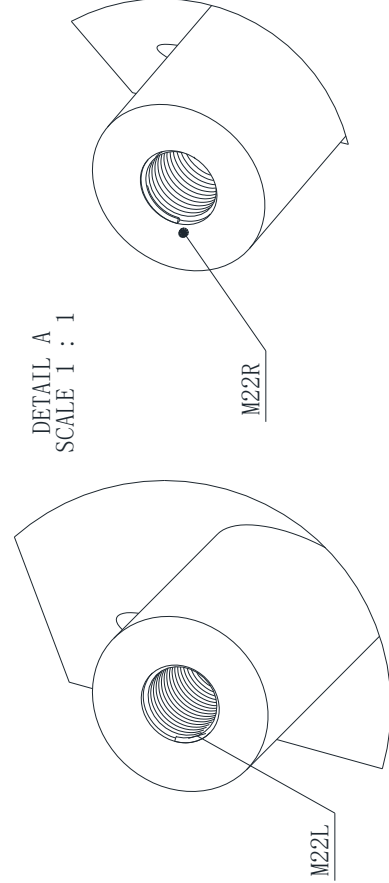
JOINT M22L

ITEM NO.	PART NUMBER	DESCRIPTION	Tot. Wei	WEIGH T /Kg/	QTY.
1	PL 25	-180x125x25	4.42	4.42	
2	M22L	L=86			

JOINT M22R

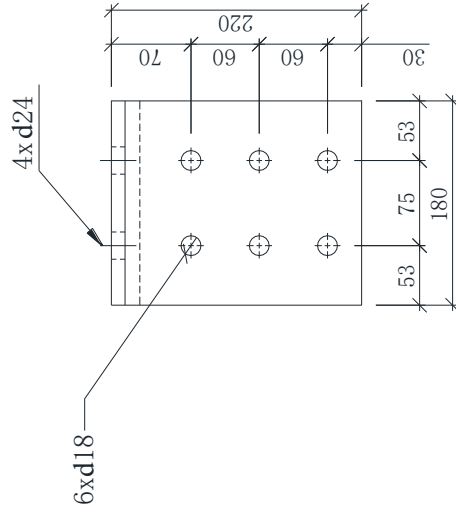
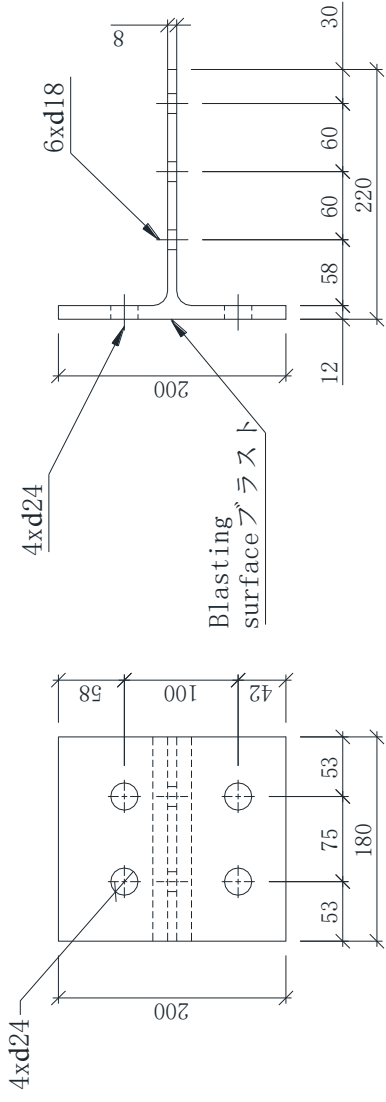
ITEM NO.	PART NUMBER	DESCRIPTION	Tot. Wei	WEIGH T /Kg/	QTY.
1	PL 25	-180x125x25	4.42	4.42	
2	M22R	L=86			

DETAIL A  
SCALE 1 : 1



Appendix B

T-STUB / H300x200x8x12 / n=8/



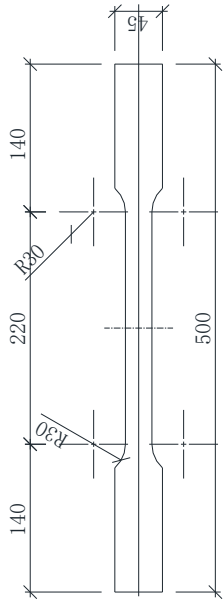
1. Contact surface must be blast on the target place as shown in this figure.
2. n=8 total quantity of numbers.



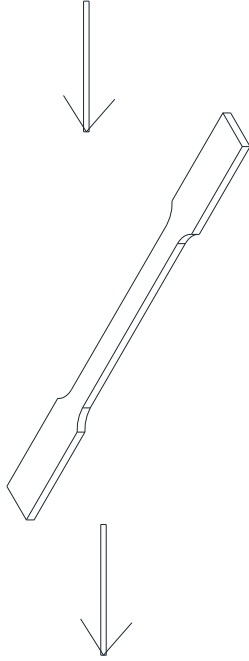
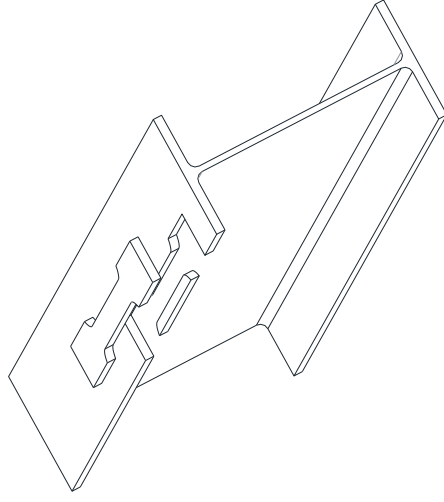
Appendix B

BEAM TEST PIECE /H250x125x6x9 /n=2/

STEP-2



STEP-1



1. The sample of the test specimen must be taken up from the beam flange as shown above figure.
2. n=2 total quantity of numbers.

## RELATED PUBLICATIONS:

1. “Steel rigid beam-to-column connections strengthened by buckling-restrained knee braces using round steel core bar dampers,” Munkhunur T, Tagawa H, Chen X, *Engineering Structures*, Vol. 250, p. 113431, 2022.
2. “Experimental study on slender buckling-restrained knee braces with round steel core bar cores,” Munkhunur T, Tagawa H, Chen X, *Frontiers of Structural and Civil Engineering*, accepted for publication.
3. “Finite element analysis on steel beam-to-column joint strengthened by buckling-restrained knee brace using round steel core bar,” Munkhunur T, Tagawa H, Chen X, 12<sup>th</sup> Pacific Structural Steel Conference Tokyo, Japan, November 9<sup>th</sup> to 11<sup>th</sup>, 2019.
4. “Experimental study on steel beam-to-column joint strengthened by buckling-restrained knee brace using steel core bar,” Munkhunur T, Tagawa H, Chen X, 17<sup>th</sup> World Conference on Earthquake Engineering, 17 WCEE Sendai, Japan, September 13<sup>th</sup> to 18<sup>th</sup>, 2020.